Center for Advanced Communications

Villanova University

TECHNICAL REPORT

(10/1/02 – 9/30/03)

CLASSIFICATION AND DISCRIMINATION OF SOURCES WITH TIME-VARYING FREQUENCY AND SPATIAL SPECTRA

Submitted to

Office of Naval Research

Grant No. N00014-98-1-0176

Principal Investigator

Moeness G. Amin

Contributors

Prof. Moeness Amin
Prof. Yimin Zhang
Dr. Gordon Frazer
Mr. Baha Obeidat
Mr. Behzad Mohammadi

October 2003

20030930 115

Table of Contents

Executive Summary

Classification and Discrimination of Sources with Time-Varying Frequency and Spatial Spectra

ONR, Grant no. N00014-98-1-0176

Moeness Amin (PI)

This report presents the results of the research performed under ONR grant number N00014-98-1-0176 over the period of October 1st, 02 to September 30th, 03. The research team working on this project consists of: Prof. Moeness Amin (PI), Prof. Yimin Zhang (Research Professor), Dr. Gordon Frazer (Visiting Research Professor from DSTO, Australia), Mr. Weifeng Mu, Mr. Baha Obeidat, and Mr. Behzad Mohammadi (Graduate Students). We have also collaborated with Prof. X-G. Xia from University of Delaware, Prof. H. Ge from NJIT, and Prof. A. Zoubir from Darmstadt University of Technology, Germany.

The research objectives in FY03 evolved around the detection of complex Doppler target signatures using time-frequency signal representations. In additions to achieving these objectives, the research has progressed on two other fronts; namely, *Polarimetric Sensor Array Processing and Subband Array Implementations for Space-Time Processing*. Four book chapters, five journal article, and ten conference papers have been generated from our research efforts in FY03. Below is the summary of the research accomplishments in each of the above three areas. Copies of the principle publications are included in the report.

1. Over the Horizon Radar

We have developed a high-resolution time-varying signature estimation of weak target signals for Over-the-Horizon Radars (OTHRs). A significant problem in OTHR is robust high-resolution Doppler processing of maneuvering targets. The complex Doppler signatures present in these cases smear in Doppler and have reduced detectability and localization. We have introduced a powerful clutter suppression technique combined with high-resolution time-varying signature estimation method, specifically, in low signal-to-clutter ratio environment. This technique is based on an integration of autoregressive filtering, adaptive chirp/chirplet transform, and adaptive bilinear transform. The new technique is most applicable to scenarios where resolution of multipath returns may clearly reveal accelerating/decelerating characteristics of maneuvering targets which prove significant for target classifications. In these situations, the Fourier transform and many existing time-frequency methods often fail.

2. Polarimetric Sensor Array Processing

We have developed polarimetric time-frequency distributions for sensor arrays. A new technique that encompasses the target time-varying Doppler signature as well as the target polarization signature for applications to high-resolution imaging and direction finding has been

introduced. Both signatures are estimated and processed by multi-antenna receivers. The signal polarization information empowers the recently introduced spatial time-frequency distributions, leading to improved source discrimination and angle-of-arrival estimation. The proposed technique is a general approach that utilizes diversity and distinctions amongst targets based on their polarizations, directions, and time-frequency signal representations. Coupling of those three source characteristics has proven superior to dealing with each one separately.

3. Subband Array Implementations for Space-Time Processing

Space-time adaptive processing (STAP) systems have been shown to be effective in suppressing undesired signals in Radar and mobile communication applications. The high complexity and slow convergence, however, are often the hurdles in practical implementations of STAP systems. Subband array implementations provide near-optimal steady state performance with reduced implementation complexity and improved convergence performance. We continued to analyze the performance of several subband array processing schemes. In particular, we have evaluated the effect of decimation on the mean square errors and examined the advantages of performing subband processing on the received input data as well as the desired (reference) signal.

List of Publications

Journal Papers

W. Mu, M. G. Amin, and Y. Zhang, "Bilinear signal synthesis in array processing," <u>IEEE Transactions on Signal Processing</u>, vol. 53, no. 1, January 2003.

* Y. Zhang, M. G. Amin, and G. J. Frazer, "High-resolution time-frequency distributions for maneuvering target detection in over-the-horizon radars," accepted for publication in the <u>IEE Proceedings on Radar, Sonar and Navigation</u>.

* G. Wang, X.-G. Xia, B. T. Root, V. C. Chen, Y. Zhang, and M. G. Amin, "Maneuvering target detection in over-the-horizon radar by using adaptive clutter rejection and adaptive chirplet transform," accepted for publication in the <u>IEE Proceedings on Radar, Sonar and Navigation</u>.

* M. G. Amin and Y. Zhang, "Bilinear signal synthesis using polarization diversity," accepted for publication in the <u>IEEE Signal Processing Letters</u>.

A. Belouchrani, M. G. Amin, K. Marium, and A. Zoubir, "Blind Separation of Non-Stationary Sources using joint anti-diagonalization," accepted for publication in the <u>IEEE Signal Processing Letters</u>.

Book Chapters

* M. G. Amin, Y. Zhang, G. J. Frazer, and A. R. Lindsey, "Spatial time-frequency distributions: Theory and applications," in L. Debnath (ed.), <u>Wavelets and Signal Processing</u>, Boston, MA: Birkhauser, 2003.

* M. G. Amin and Y. Zhang, "Interference suppression in spread spectrum communication systems," in J. G. Proakis (ed.), <u>The Wiley Encyclopedia of Telecommunications</u>, New York, NY: John Wiley, 2002.

* M. G. Amin and Y. Zhang, "Spatial time-frequency distributions and their applications," in B. Boashash, <u>Time-Frequency Signal Analysis and Processing: A Comprehensive Reference</u>, Elsevier, Oxford, UK, 2003.

* Y. Zhang, M. G. Amin, and B. Obeidat, "Polarimetric array processing for nonstationary signals," in S.Chandran (ed.), <u>Adaptive Antenna Arrays: Trends and Applications</u>, Springer-Verlag (in press).

Conference Papers

Y. Zhang, M. G. Amin, and H. Ge, "Nonstationary interference suppression in DS/SS communications using space-time oblique projection techniques," <u>IEEE International Symposium on Signal Processing and Information Technology</u>, Marrakech, Morocco, December 2002.

Y. Zhang, M. G. Amin, and A. R. Lindsey, "Improved blind separations of nonstationary sources based on spatial time-frequency distributions," <u>International Symposium on Independent Component Analysis and Blind Signal Processing</u>, Nara, Japan, April 2003.

Y. Zhang, M. G. Amin, and G. J. Frazer, "High resolution time-frequency distributions for manuvering target detection in over-the-horizon radars," <u>IEEE International Conference on Acoustics, Speech, and Signal Processing</u>, Hong Kong, China, April 2003.

L. A. Cirillo and M. G. Amin, "Auto-term detection using time-frequency array processing," <u>IEEE International Conference on Acoustics, Speech, and Signal Processing</u>, Hong Kong, China, April 2003.

G. Wang, X.-G. Xia, B. Root, V. Chen, Y. Zhang, and M. G. Amin, "Manuvering target detection in over-the-horizon radar by using adaptive chirplet transform and subspace clutter rejection," <u>IEEE International Conference on Acoustics, Speech, and Signal Processing</u>, Hong Kong, China, April 2003.

Y. Zhang, M. G. Amin, and B. A. Obeidat, "Direction finding using spatial polarimetric time-frequency distributions," <u>International Symposium on Signal Processing and Its Applications</u>, Paris, France, July 2003.

Y. Zhang, M. G. Amin, B. M. Dogahe, and G. J. Frazer, "Time-frequency analysis for maneuvering target detection in over-the-horizon radars," <u>International Symposium on Signal Processing and Its Applications</u>, Paris, France, July 2003.

Y. Zhang, K. Yang, and M. G. Amin, "Space-time adaptive processing and subband array implementations," <u>SPIE Annual Meeting</u>, San Diego, CA, Aug. 2003.

Y. Zhang, M. G. Amin, and B. Obeidat, "Spatial polarimetric time-frequency distributions and applications to direction-of-arrival estimation," <u>SPIE Annual Meeting</u>, San Diego, CA, Aug. 2003.

Y. Zhang, B. A. Obeidat, and M. G. Amin, "Polarimetric time-frequency MUSIC in coherent signal environment," <u>IEEE Workshop on Statistical Signal Processing</u>, St. Louis, MO, Sept.-Oct, 2003.

Papers marked (*) are included in the report.

High Resolution Time-Frequency Distributions for Maneuvering Target Detection in Over-the-Horizon Radars

Yimin Zhang and Moeness G. Amin

Center for Advanced Communications, Villanova University, Villanova, PA 19085, USA

Gordon J. Frazer

ISR Division, DSTO, Edinburgh, Australia

Abstract

A novel high-resolution time-frequency representation method is proposed for source detection and classification in over-the-horizon radar (OTHR) systems. A data-dependent kernel is applied in the ambiguity domain to capture the target signal components, which are then resolved using the root-MUSIC based coherent spectrum estimation. This two-step procedure is particularly effective for analyzing a multi-component signal with time-varying complex time-Doppler signatures. By using the different time-Doppler signatures, important target maneuvering information, which is difficult to extract using other linear and bilinear time-frequency representation methods, can be easily revealed using the proposed method.

I. Introduction

By exploiting the reflective and refractive nature of high-frequency (HF) radiowave propagation through the ionosphere, over-the-horizon radars (OTHRs) perform wide-area surveillance at long range well beyond the limit of the horizon of conventional line-of-sight (LOS) radars. OTHR systems have become an important tool for wide-area surveillance [1], [2], [3], [4], [5].

A significant problem in OTHR is robust high-resolution Doppler processing of accelerating or decelerating targets. This arises during aircraft and ship target maneuver and during observations of rockets during boost phase and mid-course flight. The complex Doppler signatures present in these cases reveal important information about the target.

Most OTHR systems use classical Doppler processing where one Doppler spectrum is computed using one full coherent integration time (CIT, typically 1 – 100 seconds in OTHR). Some systems use overlapped Doppler processing to provide a spectrogram analysis of time-varying Doppler. Accelerating/decelerating targets smear in Doppler and have reduced detectability and localization. The smearing reduces resolution and can obscure important multi-component Doppler features.

There are numerous time-frequency distributions (TFDs) other than the spectrogram [6], [7], [8]. Many TFDs provide superior localization in time and Doppler frequency. Previous applications of time-frequency signal representations to OTHR, however, have generally been disappointing. The fundamental challenge with OTHR is that the TFD must retain its desirable resolution and concentration properties in the presence of clutter that is typically 40dB or more stronger than the target (although possibly localized in a different region of time-Doppler).

The objective of this paper is to investigate and extend recent developments in data-dependent TFDs to the problem of robust high-resolution analysis of time-varying OTHR target returns. Of particular interest is the problem of multi-component target signal detection and identification where important information concerning the maneuvering target can be revealed. Such information is significant for the classification of maneuvering targets.

This paper is organized as follows. In Section II, the signal model is introduced and

2

the Doppler characteristics of the target signal are investigated. Section III provides the clutter suppression method used in this paper. In Section IV, a high-resolution time-Doppler processing method is proposed and applied to the underlying OTHR applications. Section V shows some more computational results.

II. Signal Model

A. Signal Model

Fig. 1(a) illustrates an stylised OTHR system. For simplicity of mathematical analysis, we adopt the flat ground model, as shown in Fig. 1(b).

The received signal, after pulse or sweep matched filtering and beamforming at the receiver, is expressed as

$$y(t) = x(t) + u(t) + n(t), \tag{1}$$

where $u(t)$ is the clutter, and $x(t)$ is the return signal from the target, expressed as

$$x(t) = Ae^{-j\omega_c(d_t+d_r)/c}, \tag{2}$$

where A is a complex scalar representing the propagation loss and phase, d_t and d_r are the respective one-way slant range between the transmitter and the target and between the target and the receiver, c denotes the speed of light, and $\omega_c = 2\pi f_c$ is the carrier radian frequency. In (1), $n(t)$ is internal and external noise, whose power is small in a typical situation with strong target signal-to-noise ratio. Therefore, the noise term is ignored in this paper.

In a typical OTHR scenario, as shown in Fig. 1(a), in addition to the path directly reflected from the ionosphere, there is reflection at the ground near the target. Denote l_1 and l_2 as the propagation distance of the two paths, respectively, and d_t and d_r as the respective one-way slant range between the transmitter and the target and between the target and the receiver, respectively. Then, d_t takes value of either l_1 and l_2 and so does d_r.[1] The corresponding path losses will be denoted as A_1 and A_2. Therefore, the received

[1]Some OTHR systems are bistatic in which case the transmitter and receiver are in different locations. In this case, the range from the target to the transmitter and that from the target to the receiver are different. We have ignored this difference, however, as it does not significantly affect our results.

signal consists of four combination paths which result in the following three multipath components:

$$x(t) = A_1 e^{-j\omega_c 2l_1/c} + A_2 e^{-j\omega_c 2l_2/c} + A_3 e^{-j\omega_c(l_1+l_2)/c}. \tag{3}$$

We will refer to the path $(l_1 : l_1)$ as path I, path $(l_2 : l_2)$ as path II, and the combination of path $(l_1 : l_2)$ and $(l_2 : l_1)$ as path III.

Based on the flat ground model approximation illustrated in Fig. 1(b), the slant ranges l_1 and l_2, respectively, can be expressed in terms of the range distance R, the ionosphere height H, and the aircraft height h, as

$$l_1 = \left(R^2 + (2H - h)^2\right)^{1/2}, \quad l_2 = \left(R^2 + (2H + h)^2\right)^{1/2}. \tag{4}$$

To clearly reveal the relationship between the slant ranges and the parameters, we take into account the fact that $R \gg H \gg h$ hold for a typical scenario. Then, the above expressions can be approximated as

$$l_1 \approx R + \frac{2H^2 - 2Hh}{R}, \quad l_2 \approx R + \frac{2H^2 + 2Hh}{R}. \tag{5}$$

B. Doppler Characteristics

The flight of an aircraft, in general, consists of horizontal and elevation movements. In this section, we consider the Doppler frequency characteristics of the aircraft's movement in the two different dimensions.

As an aircraft flies, R, and possibly also h, become functions of t. The height of ionosphere, H, is also slowly time-varying. However, we assume that H is a constant over the processing time interval. From (5), we obtain

$$\frac{dl_1(t)}{dt} \approx K(t)v_R(t) - \frac{2H}{R(t)}v_c(t), \quad \frac{dl_2(t)}{dt} \approx K(t)v_R(t) + \frac{2H}{R(t)}v_c(t), \tag{6}$$

where $K(t) = (1 - 2H^2/R^2(t))$, $v_R(t) = dR(t)/dt$ is the target velocity in the range direction toward the radar, and $v_c(t) = dh(t)/dt$ is the ascending velocity of the target. The Doppler frequencies of the three different paths are then obtained as

$$f_I(t) = \frac{2f_c}{c}\frac{dl_1(t)}{dt} \approx \frac{2f_c}{c}K(t)v_R(t) - \frac{4f_cH}{R(t)c}v_c(t),$$

$$f_{II}(t) = \frac{2f_c}{c}\frac{dl_2(t)}{dt} \approx \frac{2f_c}{c}K(t)v_R(t) + \frac{4f_cH}{R(t)c}v_c(t), \tag{7}$$

$$f_{III}(t) = \frac{f_c}{c}\frac{dl_1(t) + dl_2(t)}{dt} \approx \frac{2f_c}{c}K(t)v_R(t).$$

4

From the above discussion, it is evident that, while the dominant Doppler component $2f_cK(t)v_R(t)/c$ is shared by all the three paths and reveals the target velocity in the range direction, the small Doppler difference between the paths is a function of $h(t)$ and, therefore, reveals another important information on how the target moves in the elevation direction.

In this paper, we consider an often encountered scenario of a maneuvering aircraft as an example. In this case, the target makes a 180° turn in $T = 30.72$ seconds to change height and direction. This time interval corresponds to 6 revisits (blocks), and each block contains 256 samples (slow time samples from the radar). The parameters used in the analysis and simulations are listed in Table 1. All the multipath signals are considered to fall within the same range cell.

The range is expressed as

$$R(t) = R(0) - \frac{v_R(t)T}{\pi} \sin\left(\frac{t\pi}{T}\right) \tag{8}$$

and the height is expressed as

$$h(t) = h(0) + \frac{v_c(t)T}{\pi} \left[1 - \cos\left(\frac{t\pi}{T}\right)\right]. \tag{9}$$

The cross-range movement is not considered because it does not significantly contribute to Doppler frequency. Substituting (8) and (9) to (5) yields the following Doppler frequency

$$f(t) = f_R(t) + f_h(t), \tag{10}$$

where $f_R(t)$ is the Doppler frequency caused by the change of $R(t)$ and is expressed as

$$f_R(t) = \frac{2f_c}{c} v_R(t) = \frac{2vf_c}{c} \cos\left(\frac{t - t_1}{T}\pi\right), \tag{11}$$

and $f_h(t)$ in (10) is the Doppler frequency caused by the change of height $h(t)$ and is expressed, for path I, as

$$f_{h,I}(t) = \frac{4v_c(t)f_cH}{R(t)c} \sin\left(\frac{t - t_1}{T}\pi\right). \tag{12}$$

It is easy to confirm that $f_{h,II}(t) = -f_{h,I}(t)$ and $f_{h,III}(t) = 0$ for all t.

The time-Doppler signatures are plotted in Fig. 2. The dominant Doppler component is proportional to the target velocity in the slant range direction, and the small Doppler

difference between the three paths is proportional to the ascending velocity of the target. This difference provides important information on how the target moves in the elevation direction. The maximum one-side Doppler difference corresponding to the maximum ascending speed 1500 m/min = 25 m/s is about 1.17 Hz.

The frequency resolution in the underlying system is $\Delta f = f_s/N = 50/256 = 0.195$ Hz. The detection of such a small Doppler difference is possible through the application of discrete Fourier transform (DFT) to the received signal, provided that $v(t)$ and, subsequently, $2f_c v(t)/c$, are fixed over the CIT of 256 samples. However, when v_R is not a constant, which occurs if the target is accelerating or decelerating, ascending or descending, or, changing its direction, $2f_c v(t)/c$ becomes time-varying and the conventional DFT-based approach does not provide high Doppler resolution even with a long CIT [10]. In this case, the detection and estimation of the Doppler shift caused by a change of h become difficult. The presence of strong clutter adds more difficulties to the underlying problem.

Conventional methods based on spectrogram and other TFDs smear the target's Doppler signature and cannot provide satisfactory resolution performance. The smearing reduces resolution and is likely to obscure important multi-component time-Doppler signatures. To realize high-resolution Doppler detection and estimation, we must first proceed with clutter suppression followed by an effective time-Doppler processing method. The combination of the two methods clearly reveals the interested time-Doppler signatures.

III. Clutter Suppression

We consider TFD methods to achieve high-resolution time-Doppler localization. In the underlying problem, TFDs are referred to as time-Doppler distributions (TDDs). The most commonly used TFD is the Wigner-Ville Distribution (WVD). The WVD of signal $y(t)$ is defined as

$$W_{yy}(t,f) = \int y(t+\tau/2)y^*(t-\tau/2)e^{-j\omega\tau}d\tau \tag{13}$$

where the superscript "*" denotes complex conjugate. All integrals without limits imply integration from $-\infty$ to $+\infty$. Substituting (1) in (13), the WVD of $y(t)$ can be written in terms of

$$W_{yy}(t,f) = W_{xx}(t,f) + W_{uu}(t,f) + W_{xu}(t,f) + W_{ux}(t,f), \tag{14}$$

where the first two terms are, respectively, the autoterms of the target signal and the clutter, and the other two are their crossterms.

In a typical OTHR receiver, the clutter is much stronger (typically 30 to 50 dB) than the target signal. Without substantial suppression of the clutter, the TDD autoterm of the target will be significantly obscured by the clutter autoterm as well as the crossterms between the clutter and signal.

Clutter often has high correlation to that at its neighboring range cells and cross-range cells. Based on this property, clutter mitigation methods using received signals from other range and cross-range cells have been proposed in, for example, [9], [10]. However, in this paper, the received signal from other range and cross-range cells are not used.

We point to the fact that the clutter is highly localized in low frequencies and can be well modeled as an autoregressive (AR) process [11], [12]. Therefore, the clutter can be substantially suppressed by using the AR pre-whitening techniques. Denote P as the order of the AR model, the AR polynomial parameters $a(t), t = 0, ..., P$ can be estimated via the modified covariance method [13].

Filtering the received signal $y(t)$ through a finite impulse filter (FIR), constructed using the AR polynomial parameters, results in the pre-whitened signal:

$$z(t) = y(t) * a(t) = x(t) * a(t) + u(t) * a(t) \triangleq z_x(t) + z_u(t), \tag{15}$$

where "$*$" denotes the convolution operator.

In this paper, the target signal calculated in Section II is overlaid to real OTHR clutter data. We assume that $A_1 = A_2$, and $A_3 = A_1 + A_2 = 2A_1$. The order of the AR model should be chosen to maximize the signal-to-clutter ratio (SCR). The order of the AR model is set to a unit value (P=1). The spectrogram of block 3, which corresponds to the 256 samples from 10.24 to 15.36 seconds, before and after the AR pre-whitening is shown in Fig. 3. It is seen that, while the clutter is substantially suppressed by more than 40 dB, the target signal is only partially affected when its Doppler frequency is very close to that of the clutter. Figs. 4 and 5 show the WVDs of the $y(t)$ and $z(t)$ before and after the pre-whitening. The WVDs are computed from the interpolated data sequence to show the full Doppler-frequency range. While it is often difficult to identify the target in the WVD before pre-whitening (Fig. 4), the target signature can now be somewhat identified in Fig.

5. Further and key improvement in resolutions of the target signature components can be achieved by using the techniques highlighted in Section 4.

IV. High-Resolution Time-Doppler Processing

Even after substantial clutter suppression, the result in Fig. 5 does not reveal clear time-Doppler signatures. There are numerous TFDs other than the spectrogram and the WVD which provide superior localization. Previous applications of time-frequency signal representation techniques to the OTHR problem, however, has generally been disappointing because problem is particularly difficult and demanding.

To achieve chirp signal detection, discrimination, and classification, we propose time-Doppler estimation based on adaptive kernel and high-resolution time-Doppler localization. Bilinear TDDs as well as their Fourier transforms (i.e, ambiguity functions and local auto-correlation functions) are considered.

A. Time-Doppler Distributions and Adaptive Kernel

In the following, we assume that each component of the return signal from the target can be approximated as a chirp over the period of one block, i.e.,

$$x(t) = \sum_{i=1}^{3} A_i e^{j(\alpha_i t + \beta_x t^2/2)} \tag{16}$$

is considered for a time period. Such approximation permits us to obtain important signal information, as discussed in Section II, from the received data signal.

To estimate the chirp rate of the signal, it is common to examine the ambiguity function. The ambiguity function of $z(t)$ is defined as

$$A_z(\theta, \tau) = \int_t z(t + \tau/2) z^*(t - \tau/2) e^{j\theta t} dt \tag{17}$$

where θ and τ are, respectively, the frequency-lag and time-lag variables. Similar to the TDD, the ambiguity function can be decomposed into two autoterms and two crossterms. One important property of the ambiguity function is that all signal autoterms pass through the origin, whereas the crossterms are often away from the origin. For a multi-component parallel chirp signal, the ambiguity function shows linear signatures depending on the signal chirp rate. Therefore, unlike the time-Doppler domain, in which a two-dimensional

8

search is required, the chirp rate in the ambiguity domain can be estimated by a one-dimensional search. The reducution in computations make the ambiguity-domain attractive for chirp rate estimation.

The chirp rate can be estimated by searching for the peaks of the following Q function [14]

$$Q(\xi) = \int |A_z(r\cos\xi, r\sin\xi)| dr. \tag{18}$$

In the case considered, peaks possibly appear at $\xi_x = -1/\tan^{-1}(\beta_x)$ and $\xi_u = -1/\tan^{-1}(\beta_u)$, where β_x and β_u are the chirp rates of the signal and the principle component of the residual clutter, respectively.

Based on the chirp rate estimation, an adaptive kernel can be designed. We construct a kernel whose passband only captures the target signal chirp rate. The clutter will be, subsequently, mitigated in the ambiguity domain due to its distinct orientation compared to the target signal. For an estimated chirp rate $\hat{\xi}_x$, the following adaptive kernel is constructed to encompass the autoterm ambiguity function of the target signal, i.e.,

$$\phi_a(\theta, \tau) = e^{-d^2(\theta,\tau)/\sigma^2} \tag{19}$$

where σ is the kernel width, and

$$d^2(\theta, \tau) = \theta^2 + \tau^2 - (\theta\sin\hat{\xi}_x + \tau\cos\hat{\xi}_x)^2. \tag{20}$$

The adaptive kernel suppresses the clutter and noise, as well as all crossterms.

The adaptive chirp TDD is

$$C_x(t, \omega) = \frac{1}{2\pi} \sum_\theta \sum_\tau A_x(\theta, \tau)\phi_a(\theta, \tau)e^{-j\theta t - j\tau\omega}. \tag{21}$$

The above distribution has substantially suppressed clutter and noise, as well as the crossterm TDDs between the multi-component signal. The adaptive TDD is shown in Fig. 7 for the received signal at block 3.

B. High Resolution Time-Doppler Localization

In [14], chirp MUSIC was introduced for the estimation of the Doppler frequencies at each time index t. The estimated auto-correlation function $\hat{R}_x(t, \tau)$ is used to construct a

9

data matrix for MUSIC spectrum estimation. However, the resulting matrix is, in general, not positive definite. Therefore, in [14], the filtered ambiguity function is transformed to the time-frequency domain, and only the positive part of the TFD is considered for the construction of the auto-correlation function. This method, although showing good time-Doppler localization in high signal-to-noise ratio (SNR) situations, is computationally inefficient because spectrum estimation is implemented for each time index. In addition, the estimated time-Doppler signature is not always consistent with the true values, particularly in low SNR scenarios. Therefore, it is not a candidate for application in the underlying OTHR applications.

In this paper, we obtain the auto-correlation directly from the filtered ambiguity function as

$$\hat{R}_x(t,\tau) = \frac{1}{2\pi} \int A_x(\theta,\tau)\phi_a(\theta,\tau)e^{-j\theta t}d\theta. \tag{22}$$

Because signal components with single chirp rate are involved, the auto-corelation function $R_{x,i}(t,\tau)$ of each chirp component has the form

$$R_{x,i}(t,\tau) = A_i^2 e^{j(\alpha_i+\beta_x t)\tau}, \tag{23}$$

which is dependent of t. Such dependence can be removed by using the estimated value, $\hat{\beta}_x = -1/\tan(\hat{\xi}_x)$. From $R_{x,i}(t,\tau)$, the time-independent auto-correlation function is estimated as

$$\tilde{R}_x(\tau) = \int \hat{R}_x(t,\tau)e^{-j\hat{\beta}_x t\tau}dt. \tag{24}$$

The coherent integration yields coherent MUSIC subspace estimation of α_i's for improved performance. The vector $\tilde{R}_x(\tau)$ is considered as raw data sequence, rather than as covariance elements adopted in [14], to ensure the positive definiteness of the covariance matrix for spectrum estimation. In our simulations, the root-MUSIC algorithm is used for computational convenience. Only one root-MUSIC operation is required for each block. The chirp signatures at different times are then constructed using the estimated chirp rate and α_i's.

In Fig. 8, the coherent time-varying root-MUSIC spectrum is shown for block 3. Despite the low SCR, the time-Doppler signatures, along with the Doppler frequency difference

information, are estimated clearly and consistently. Simulation results for all other blocks also confirmed successful Doppler signature estimation.

C. TDD Magnitude Compression and More Simulation Results

The existence of strong time-Doppler value at some discrete points, however, may sometime create undesired time-Doppler signatures. Because the desired TDDs typically show much more consistent signature over all samples with its true chirp rate, we propose the use of the following magnitude compression of $C_x(t, \omega)$,

$$C'_x(t, \omega) = |C_x(t, \omega)|^\gamma \text{sign}[C_x(t, \omega)], \tag{25}$$

where $0 < \gamma < 1$. Our experience suggests that γ should take value between 0.1 and 0.5. $C'_x(t, \omega)$ is used instead to estimate the auto-correlation function $\hat{R}_x(t, \tau)$ in (26).

When the TDD magnitude compression is performed, the local auto-correlation function $R_x(t, \tau)$ should be obtained from

$$\hat{R}_x(t, \tau) = \frac{1}{4\pi} \sum_\omega C'_x(t, \omega) e^{j\tau\omega}. \tag{26}$$

In Fig. 9, the time-Doppler signatures obtained from the proposed method is shown for the entire turning process of the aircraft. In the computations, the results are calculated from six blocks, each of 256 samples. $\gamma = 0.2$ are used for each block. The theoretical values of the Doppler signatures are overlaid in the plot. It is evident that the proposed method provides stable and consistent estimation of the Doppler signatures over different situations.

To show the importance of applying magnitude compression, we plotted in Fig. 10 the time-Doppler signatures obtained without the magnitude compression. It is seen that, while most time-Doppler signatures are correctly estimated, one component in block 4 is not. The reason is simply that, in the process of clutter suppression, signal component with close spectrum to the clutter may loss part of its signal power.

V. Conclusions

In this paper, a novel method has been proposed for high-resolution time-Doppler signature localization applied to over-the-horizon radar systems. By combining AR prewhitening for effective clutter suppression, time-frequency based signal discrimination,

and coherent high-resolution spectrum analysis, the proposed method provides robust estimation of time-varying Doppler signature in low signal-to-clutter ratio (SCR) scenarios.

References

[1] J. M. Headrick and M. I. Skolnik, "Over-the-horizon radar in the HF band," *Proc. IEEE*, vol. 62, pp. 664–673, 1974.

[2] A. A. Kolosov, *Over-The-Horizon Radar*, Boston, MA: Artech House, 1987.

[3] L. F. McNamara, *The Ionosphere, Communications, Surveillance, and Direction Finding*, Melnourne, FL: Krieger Publishing, 1991.

[4] G. D. McNeal, "The high-frequency environment at the ROTHR Amchitka radar site," *Radio Science*, vol. 30, pp. 739–746, May–June 1995.

[5] J. M. Headrick and J. F. Thomason, "Naval applications of high frequency over-the-horizon radar," *Nav. Eng. J.*, vol. 108, pp. 353–359, May 1996.

[6] L. Cohen, *Time-Frequency Analysis*, Englewood Cliffs, NJ: Prentice Hall, 1995.

[7] H. I. Choi and W. J. Williams, "Improved time-frequency representation of multicomponent signals using exponential kernels," *IEEE Trans. Acoust., Speech, Signal Processing*, vol. 37, pp. 1132–1143, July 1990.

[8] D. L. Jones and R. G. Baraniuk, "An adaptive optimal-kernel time-frequency representation," *IEEE Trans. Signal Processing*, vol. 43, no. 10, pp. 2361–2371, Oct. 1995.

[9] S. Kraut, K. Harmanci, and J. Krolik, "Space-time adaptive processing for over-the-horizon spread-Doppler clutter estimation," in *Proc. ICASSP*, Istanbul, Turkey, pp. 3401–3044, June 2000.

[10] G. Wang, X-G. Xia, B. T. Root, V. C. Chen, Y. Zhang, and M. G. Amin, "Maneuvering target detection in over-the-horizon radar by using adaptive chirplet transform with subspace clutter rejection," submitted to *IEE Proc. Radar, Sonar and Navigation*.

[11] J. Barnum, "Ship detection with high-resolution HF skywave radar," *IEEE J. Oceanic Engineering*, vol. 11, no. 2, pp. 196–209, April 1986.

[12] T. J. Nohara and S. Haykin, "AR-based growler detection in sea clutter," *IEEE Trans. Signal Processing*, vol. 41, no. 3, pp. 1259–1271, March 1993.

[13] S. M. Kay, *Modern Spectral Estimation: Theory and Applications*, Englewood Cliffs, NJ: Prentice Hall, 1998.

[14] R. M. Mickel and W. J. Williams, "High resolution frequency tracking via non-negative time-frequency distributions," in *Proc. IEEE Workshop on Statistical Signal and Array processing*, Pocono, PA, Aug. 2000.

TABLE I

MAJOR PARAMETERS

Parameter	Notation	Value
initial range	$R(0)$	2000 km
ionosphere height	H	350 km
aircraft initial height	$h(0)$	10000 m
maximum range speed	v_R	500 km/hr
maximum climbing speed	v_c	1500 m/min
carrier frequency	f_c	20 MHz
waveform repetition frequency	f_s	50 Hz
samples per block	N	256 samples
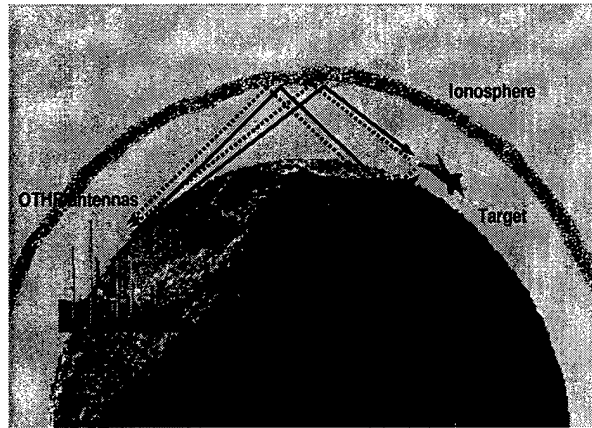
(a)
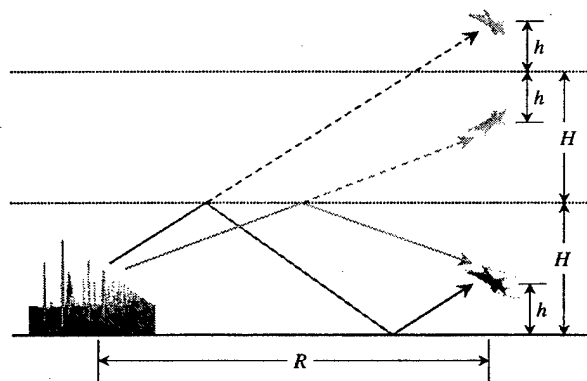
(b)

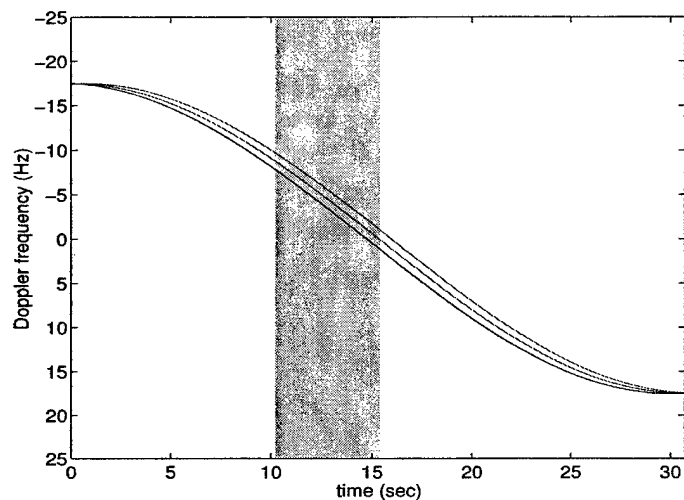Fig. 1. (a) OTHR systems. (b) Flat ground approximation.

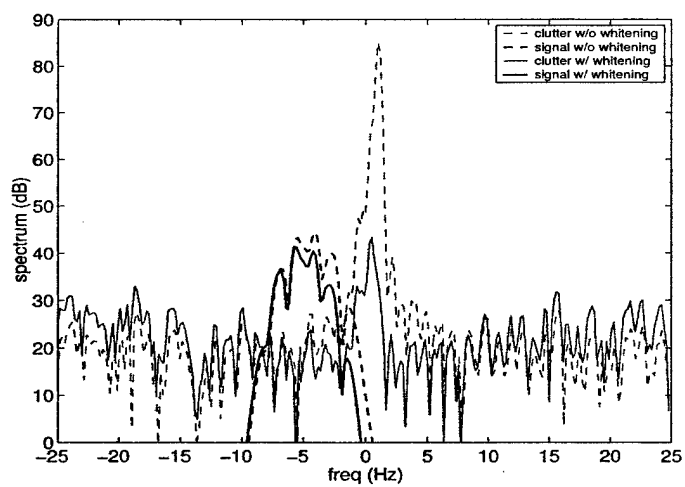Fig. 2. Time-Doppler frequency signatures.

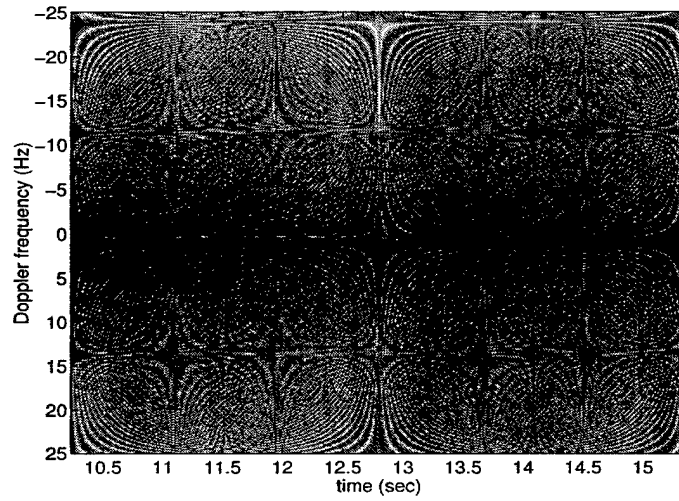Fig. 3. Block-wise spectrogram of the received signal before and after AR pre-whitening.

15

Fig. 4. WVD of received signal $y(t)$ before AR pre-whitening (block 3).
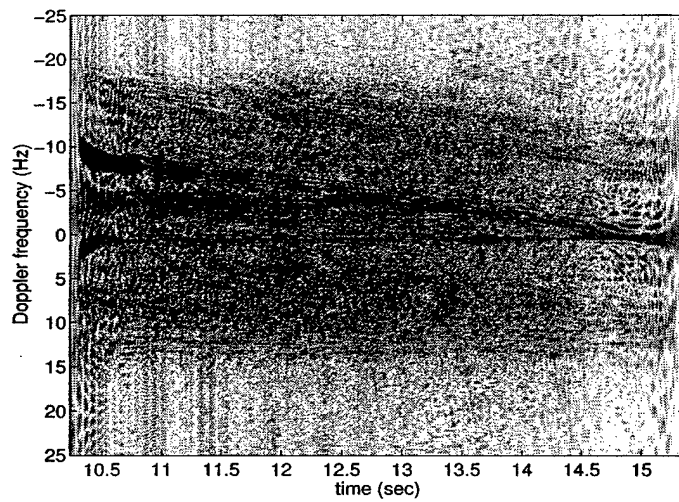
Fig. 5. WVD of the received signal $z(t)$ after AR pre-whitening (block 3).
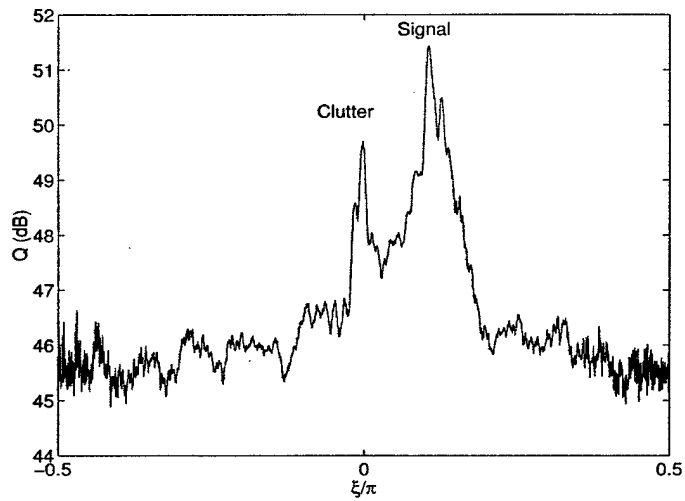
Fig. 6. Q function calculated (block 3).
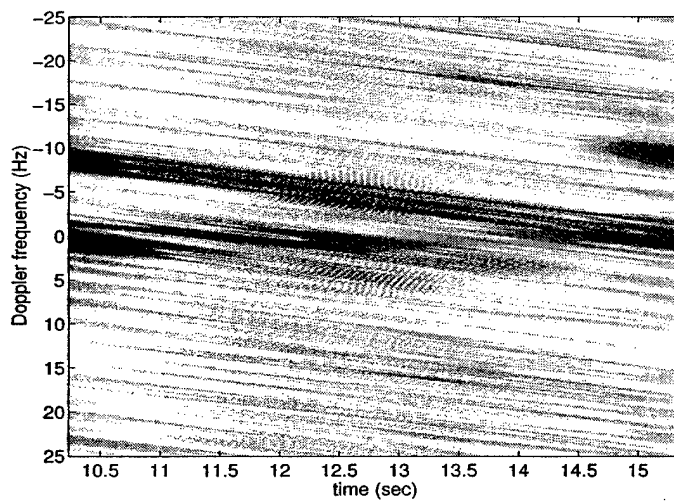
Fig. 7. Adaptive time-Doppler distribution of the pre-whitened received signal (block 3).
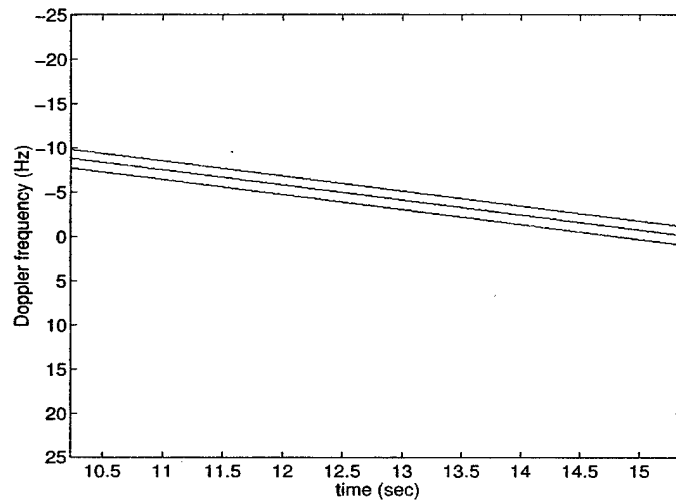
Fig. 8. Estimated time-Doppler signature via chirp root-MUSIC algorithm (block 3).
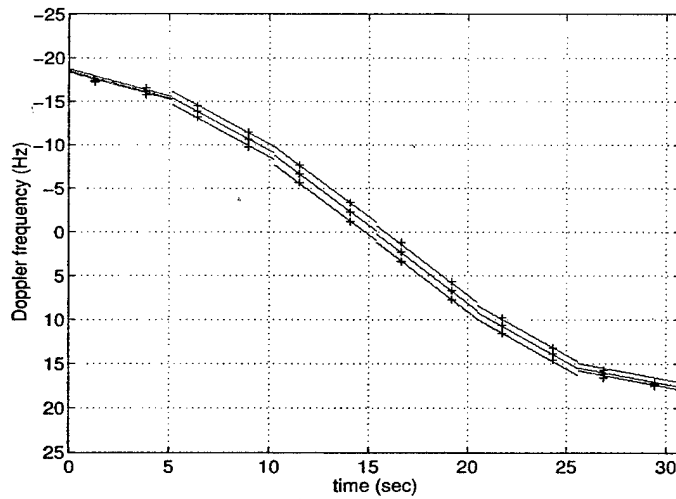
Fig. 9. Estimated time-Doppler signature of all blocks with magnitude compression ('+' marks show the theoretical Doppler frequencies for the three paths).

18

Fig. 10. Estimated time-Doppler signature of all blocks without magnitude compression ('+' marks show the theoretical Doppler frequencies for the three paths).

Maneuvering Target Detection in Over-the-Horizon Radar Using Adaptive Clutter Rejection and Adaptive Chirplet Transform

Genyuan Wang and Xiang-Gen Xia
Department of Electrical and Computer Engineering
University of Delaware
Newark, DE 19716
{gwang, xxia}@ee.udel.edu

Benjamin T. Root and Victor C. Chen
Radar Division
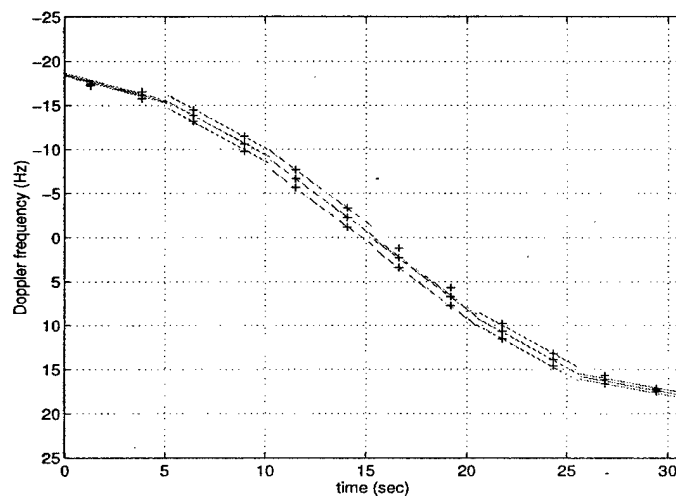Naval Research Laboratory
Washington, DC 20375
{benroot, vchen}@radar.nrl.navy.mil

Yimin Zhang and Moeness Amin
Center for Advanced Communications
Villanova University
Villanova, PA 19085
{zhang, amin}@ece.villanova.edu

Abstract

In over-the-horizon radar (OTHR) systems, the signal-to-clutter ratio (SCR) used for moving target detection is very low. For slowly moving targets such as ships, the SCR is typically from −50 dB to −60 dB and their Doppler frequencies are close to that of the clutter. For maneuvering targets, such as aircrafts and missiles, the Doppler frequencies are time-varying when a long integration time is considered. When a target does not move uniformly, the Fourier transform based target detection techniques, including super-resolution spectrum techniques, may fail to work appropriately. In such situations, the Doppler signatures are time-varying and, therefore, time-frequency analysis techniques can be used for maneuvering target detection. In addition, clutter rejection is also required for target detection due to the low SCR. The existing adaptive clutter rejection algorithms combine clutter rejection with spectrum analysis methods which usually assume uniformly moving target (i.e., sinusoidal Doppler signature) models. In this paper, we propose an adaptive clutter reject algorithm together with the adaptive chirplet transform technique for maneuvering target detection in a multipath environment. Simulation results using simulated maneuvering target signal with received raw OTHR clutter data show that targets with SCR below −50 dB can be detected by using the proposed algorithm.

1. Introduction

Over-the-horizon radar (OTHR) systems have been widely used to detect and track targets, such as aircrafts and surface ships, in wide-area surveillance at long ranges [1-5]. The existing OTHR detection and tracking algorithms are based on the assumption that the Doppler frequency of each target is constant or at least approximately constant during each dwell. Targets are detected from amplitude peaks away from the zero frequency. The detection capability of an algorithm depends on the SCR and the Doppler resolution which, in turn, depends on the length of the coherent integration time (CIT). In the existing Fourier transform based techniques for maneuvering target detection and tracking, there is a trade-off between the CIT length, SCR, and the Doppler resolution. For a slowly or uniformly moving target, such as a ship, the Fourier transform based techniques work well, where a long CIT can be used for clutter spread reduction. However, for a fast maneuvering target, such as fast boat, aircraft, or missile, in Fourier transform based techniques, a long CIT can not be used and, therefore, the Doppler resolution is limited. In such situations, time-frequency analysis becomes an important technique for effective maneuvering target detection and tracking. Time-frequency analysis methods [6-9] have found wide applications in radar, [10-15]. Because the radar return signals from maneuvering targets have chirp-like characteristics, a new Doppler processing method based on the adaptive chirplet transform (ACT), instead the Fourier transform, is proposed in this paper. With the adaptive chirplet transform technique, the CIT can be substantially extended and, therefore, the Doppler resolution can be improved compared with the Fourier transform based techniques.

In an OTHR system, the detection of slow targets is often difficult, due to clutter from the ground or ocean and the low SCR (typically about −50 dB to −60 dB). Therefore, clutter rejection is necessary to improve the target detect capability. The available clutter rejection algorithms include Fourier transform based adaptive clutter rejection method recently proposed by Root [2], and super-resolution spectrum estimation algorithms, for example, [16,17]. In this paper, an adaptive clutter rejection algorithm is proposed. After clutter rejection, the ACT is then applied to the clutter-mitigated signal, which makes the

energy of the maneuvering targets concentrated. By using the proposed algorithm, the maneuvering targets can be correctly detected even when the SCR is below –50 dB.

This paper is organized as follows. In Section 2, the OTHR signal model is briefly reviewed. In Section 3, the adaptive chirplet transform for OTHR is introduced. In Section 4, the adaptive clutter rejection algorithm is proposed. In Section 5, simulation results of maneuvering target detection are provided.

2. OTHR Signal Model and Problem Description

In this section, we first describe the OTHR signal model and the conventional OTHR processing for uniformly moving targets, and then the problem of interest in this paper for maneuvering targets.

2.1 OTHR Signal Model for OTHR Processing

After the low pass filtering and sampling, the received signal $s(m,n)$ for a target p with ground range r is (see for example [4, 5])

$$s(m,n) = A_p \exp(j\omega_p mT_c) \exp\left\{ j\left[\omega_p - 2\pi Bf(\frac{d_p}{c} - T_0) \right] nT_s \right\} + \xi_{n,m} \qquad (1)$$

where n, m, T_0, ω_p, d_p, f, B, T_c and $\xi_{n,m}$ are the fast time sample index, chirp pulse index, the minimum delay, Doppler frequency shift, the two-way slant rang, waveform repetition frequency, bandwidth of radar, coherent integration time and additive noise, respectively. A_p in equation (1) is the amplitude of the received signal from target (source) or clutter p. The power A_p^2 of the signal has the expression as [21] $A_p^2 = \frac{P_t G_t}{4\pi R_t^2} \times \frac{\sigma}{4\pi R_r^2} \times A_e$, where R_t and R_r are the distances (meters) of transmitter and receiver of radar to the target respectively, P_t is the power (watts) of antenna with gain G_t, σ is the cross section (in square meters) of the target, and A_e is the effective area of antenna aperture. From (1), we find that the signal part in $s(m,n)$ in terms of index n is a complex sinusoidal signal. It is also a

22

sinusoidal function of index m if the Doppler frequency ω_p does not change with m. In this case, a two-dimensional discrete Fourier transform over m and n provides the range-Doppler surface $S(m',n')$. The received clutter signal is the signal of coming from the ground and surface of sea. Signal of clutter is spread in frequency, it is not just appear in zero frequency. In the real OTH radar, there are two high peak correspond to the Bragg lines away from zero frequency which make the target detection more difficult. For a particular OTHR processing algorithm, the target detection capability depends on the SCR. Therefore, in order to improve the target detection performance, one can increase the range, Doppler resolution, and/or the SCR. The range resolution, $\Delta r = \dfrac{c}{2B}$, depends on the bandwidth B of radar. However, the Doppler resolution, $\Delta\omega = \dfrac{2\pi}{T_c}$, depends on the CIT T_c, which is chosen at the receiver. Targets and clutter with Doppler difference less than $\Delta\omega$ are located in one Doppler cell. One Doppler cell is divided into k smaller cells and the SCR is then increased by k times if the CIT increases k times. The assumption here is that the target moves uniformly within the CIT interval. This assumption, however, may not hold when the CIT is long.

2.2 Problem Description on Maneuvering Target Detection

For a maneuvering target, the signal Doppler frequency ω_p in (1), due to the target motion or non-uniform motion of electron density distribution in ionospheric [17], is no longer constant but time varying. Consider a moving target with initial velocity v and acceleration a in the direction of slant range. The Doppler frequency ω_p in (1) is $\omega_p(t) = \dfrac{4\pi}{\lambda}(v + at)$. The Doppler spread is $\Delta\omega_p = \dfrac{4\pi}{\lambda}aT_c$, and thus, the number of Doppler cells that the target energy spreads over is $\dfrac{\Delta\omega_p}{\Delta\omega} = \dfrac{2aT_c^2}{\lambda}$. Therefore, when the target moves uniformly, i.e., $a = 0$, the target energy is always concentrated in a single Doppler cell. It becomes different, however, when the target moves non-uniformly, i.e., $a \neq 0$. As an example, let

23

us assume $2a/\lambda = 1$. In this case, the target energy spreads over T_c^2 Doppler cells. This implies that, if the CIT T_c increases k times, the number of Doppler cells over which the target energy spreads increases k^2 times. Therefore, in this case, the SCR in Doppler reduces k^2 times compared to that in the uniform moving target case. This tells us that, for a maneuvering target, the CIT increase does not benefit the OTHR target detection if the Fourier transform is used in the Doppler processing. We next want to propose an adaptive chirplet transform (ACT) in the Doppler processing that may take the advantage of the long CIT no matter whether the target moves uniformly or not.

3. Chirp Signal Detection and Adaptive Chirplet Transform

In OTHR, the received signal corresponding to a range cell is typically a multi-component signal with time-varying frequency signatures corresponding to the multiple targets with different velocities and the clutter. In this section, we first review the Wigner-Ville distribution (WVD) and Radon-Wigner transform (RWT) for multiple chirp detection. We then describe the adaptive chirplet transform method which is used in the simulation in Section 5.

3.1 Chirp Signal Detection Using Radon-Wigner Transform

WVD of a signal $s(t)$ is defined as follows [7,8]

$$W_s(t,\omega) = \int_{-\infty}^{\infty} s(t+\frac{\tau}{2})s^*(t-\frac{\tau}{2})\exp(-j\omega\tau)d\tau, \tag{2}$$

where variables t and ω represent the time and frequency, respectively. WVD has the highest resolution for a single chirp signal, but its major disadvantage is the presence of artificial cross-terms caused by the quadratic multiplication nature. For a signal containing multiple linear chirps, the desired WVD auto-terms are straight lines in the Wigner plane, while the undesired cross-terms are manifested as the high frequency oscillating characteristics. To suppress the cross-terms, we consider the Radon-Wigner transform (RWT) which takes advantage of the above oscillating properties by integrating the WVD along lines with different chirp rate and frequency shift combinations. A large part of the WVD cross-

24

terms is cancelled to each other through the integration, and the residual part of the cross-terms can be further reduced in the Radon-Wigner plane by noting the fact that the RWT auto- and cross-terms have different characteristics. Therefore, a proper mask can be applied to the RWT to reduce the cross-terms with minimum distortion to the auto-terms. The WVD with substantially suppressed cross-terms can be obtained by transforming the masked RWT back to the Wigner plane [20]. It is proved in [20] that the WVD auto-terms after the inverse Radon transform of the masked coefficients are the same as those in the original WVD. These WVD auto-terms are then used to estimate the instantaneous Doppler frequencies of targets. For other instantaneous Doppler frequency estimation methods, see for example [6].

For multi-component signals with approximately equal magnitudes, the RWT filtering in the Radon-Wigner plane is effective. However, when the magnitudes of the signal components are significantly different, the method may not be effective because the cross-terms between stronger signal components may be larger than the auto-terms of weaker components. In this case, a weaker signal may be shaded in the presence of strong cross-terms and can hardly be detected. In OTHR systems, the signal echo from small targets, such as small boats, are often much weaker than that of the clutter even after the clutter cancellation. In this case, the method we introduced above can be used to detect the strongest signal component and then remove it from the original signal. This procedure is repeated until all the signal components are detected.

3. 2 Adaptive Chirplet Transform for High Order Time-Varying Frequency Signals

For a long CIT, the received signal from a maneuvering target is no longer a linear chirp signal. When the time-varying frequency is a higher order polynomial of time, the signal can be expressed as a combination of several linear chirps over different time intervals. Such kind of signal representations, introduced by Mann and Haykin [15], is called chirplet transform.

The procedure of chirplet decomposition of a signal is first to estimate the chirp rates α_1, α_2, ..., α_{N_0} of $s(t)$ over different segments, and the respective chirps $u_i(t) = \exp\left\{ j(\frac{1}{2}\alpha_i t^2) \right\}$ are then constructed. For a given frame $\{h_k(t), k \in Z\}$ and N_0 chirp rates, a new chirplet frame $\{h_k(t)u_i(t), k, i \in Z\}$ is obtained. Based on this chirplet frame $\{h_k(t)u_i(t)\}$, $s(t)$ is divided as

$$s(t) = \sum_{i=1}^{N_0} \sum_k C_{i,k} \varsigma_i h_k(t) u_i(t) \tag{3}$$

where $C_{i,k} = \langle s(t), h_k^{'}(t)u_i(t) \rangle$ are the frame decomposition and $\{h_k^{'}(t), k \in Z\}$ is the dual frame of $\{h_k(t), k \in Z\}$, $\langle \bullet, \bullet \rangle$ represents the inner product, ς_i are arbitrary weights satisfying

$$\sum_{i=1}^{N_0} \varsigma_i = 1, \quad 0 \le \varsigma_i \le 1. \tag{4}$$

For details about (3), see [13]. To have an efficient frame decomposition, $\{h_k(t), k \in Z\}$ should include functions with different time and frequency bandwidths and center (mean) locations. For example, the following modulated Gaussian functions

$$h_k(t) = \left(\frac{\gamma_k}{\pi}\right)^{1/4} \exp\left\{ -\gamma_k(t-t_k)^2 + j\left[\phi_k + \frac{\beta_k}{2}(t-t_k) \right] \right\} \tag{5}$$

are usually used, where γ_k, ϕ_k are parameters that control the envelop and phase of the chirplet, and β_k and t_k denote the frequency and time centers, respectively.

Next, we consider how to construct the chirplet frame. Radon-Wigner transform can be used to estimate these chirp rates. For a given signal $s(t)$, chirp rate α_1 is obtained by searching the largest peak in the Radon-Wigner plane after taking the RWT of the signal. We then obtain the chirplet frame $\{h_k(t)u_1(t)\}$ by modulating the frame $\{h_k(t)\}$ in (5) with $u_1(t) = \exp(j\frac{\alpha_1}{2}t^2)$. We next estimate which element in the modified frame $\{h_k(t)u_1(t)\}$ optimally matches the signal $s(t)$ and denote this element as $u_1(t)h_{k_1}(t)$ where

$$h_{k_1}(t) = \arg\min_k \left\{ \| s(t) - \frac{\langle s(t), u_1(t)h_k(t) \rangle}{\| h_k(t) \|} u_1(t)h_k(t) \| \right\}. \tag{6}$$

Define signal $s_1(t)$ as

$$s_1(t) = s(t) - \frac{\langle s(t), u_1(t)h_{k_1}(t) \rangle}{\| h_k(t) \|} u_1(t)h_{k_1}(t). \tag{7}$$

By repeating the same procedure of $s(t)$ to $s_1(t)$, we obtain the chirp rate α_2 corresponding to the second largest component of $s(t)$. Let $u_2(t) = \exp(j\frac{\alpha_2}{2}t^2)$, we obtain

$$h_{k_2}(t) = \arg\min_k \left\{ \| s_1(t) - \frac{\langle s_1(t), u_2(t)h_k(t) \rangle u_2(t)h_k(t)}{\| h_k(t) \|} \| \right\}, \tag{8}$$

and

$$s_2(t) = s_1(t) - \frac{\langle s_1(t), u_2(t)h_{k_2}(t) \rangle}{\| h_k(t) \|} u_2(t)h_{k_2}(t). \tag{9}$$

Repeating the above procedure, all signal components can be obtained, and signal $s(t)$ can be expressed as $s(t) = \sum_i s_i(t)$. Based on the above decomposition, the instantaneous frequencies of all signal components can be obtained and then used for OTHR target detection.

One can see that the search in (6) and (8) is four-dimensional and thus has a high computational complexity. In order to reduce the complexity, a sub-optimal adaptive chirplet transform algorithm with two dimensional search is given in [13] and is summarized as follows:

Step 1. Chirp rate α_1, and frequency ω_1 are estimated by

$$(\alpha_1, \omega_1) = \arg\max_{(\alpha,\omega)} |D_s(\alpha,\omega)|, \tag{10}$$

where $D_s(\alpha,\omega)$ is the RWT of $s(t)$.

Step 2. Let $g(t)$ denote a match filter with center frequency ω_1. Also, denote $u_1(t) = \exp(j\frac{\alpha_1}{2}t^2)$ and

$$h_1(t) = g(t) \circ (s(t)u_1^*(t)) \tag{11}$$

where ∘ is the convolution operator.

Step 3. The coefficient $C_{1,1}$ in (3) is obtained as

$$C_{1,1} = \langle s(t), h_1(t)u_1(t) \rangle = \int s(t)h_1^*(t)u_1^*(t)dt .$$

(12)

Step 4. Let

$$s_1(t) = C_{1,1}h_1(t)\,u_1(t), \text{ and } y_1(t) = s(t) - s_1(t).$$

(13)

Step 5. Set $s = y_1(t)$.

Step 6. Stop if the energy of $s(t)$ is small enough, otherwise go to Step 1.

Other adaptive chirplet transforms can be found in, for example [9].

4. Clutter Rejection

In OTHR, clutter is a multi-component signal with much stronger power than that of target signal. To achieve effective target detection, clutter rejection is necessary before ACT is applied. A clutter rejection algorithm using adaptive Fourier transform was proposed by Root [2]. There are some other algorithms [17,18], in which adaptive clutter rejection and maximum likelihood target detection are combined based on the sinusoidal target signal model. In this section, adaptive clutter rejection algorithms are discussed, which are independent of target detection methods and do not assume any target signal model. After clutter rejection, time-frequency analysis can be used to make the energy of maneuvering target focused.

4.1 "Adaptive Noise Canceling" Method Used to Clutter Rejection

To effectively suppress the clutter, we notice the fact that the clutter has high space correlation to its neighboring range cells. The correlation coefficient may be as high as 0.8-0.9 [17, 18]. Therefore, the received signals at neighboring range cells can be used to estimate the clutter covariance matrix of the current range cell. The idea of adaptive noise canceller can be used to the underlying OTHR clutter rejection problem. An adaptive noise canceller is a dual-input, closed-loop adaptive feedback system [19],

28

which makes use of the signal $d(n)$ received at the primary sensor and the signal $v_1(n)$ received at a reference sensor. The signal received $d(n)$ at the primary sensor is composed of the interested signal $s(n)$ and additive noise $v_0(n)$, i.e.,

$$d(n) = s(n) + v_0(n) \qquad (14)$$

It is assumed that the signal $s(n)$ and noise $v_0(n)$ are uncorrelated to each other, and $v_1(n)$ is correlated to the noise $v_0(n)$ but is uncorrelated to the signal $s(n)$. The reference signal $v_1(n)$ is used to estimated the noise component in $d(n)$,

$$y(n) = \sum_{k=0}^{K-1} w_k(n) v_1(n-k) \qquad (15)$$

where $w_k(n)$ are the adjustable tap weights of the adaptive filter. The filter output $y(n)$ is subtracted from the primary signal $d(n)$, resulting in the following error signal

$$e(n) = d(n) - y(n) = s(n) + v_0(n) - y(n). \qquad (16)$$

The error signal is used to adjust the tap weights of the adaptive filter. The error signal $e(n)$ is the overall system output, which contains the desired signal $s(n)$ with the noise suppressed.

In the OTHR target detection, the desired signal is the echo from targets, whereas the undesired signal is clutter and noise. As the OTHR signal is usually processed after beamforming, a reference sensor receiving only the clutter is not available. However, as we mentioned before, the clutter in one range cell has high correlation with that of its neighboring range cells whereas the target signals do not. Therefore, the signals received at neighboring range cells can be used for clutter suppression, resemble to the signal received at the reference sensor in an adaptive noise canceller.

4.2 Adaptive Clutter Rejection Algorithm

In this subsection, an adaptive signal subspace method is used to clutter rejection. Let $s_c(t)$ be the received signal after range compression in the current interested range cell, $s_{n_1}(t), ..., s_{n_N}(t)$ are received

signals after range compression from N neighboring range cells. Define the following signal vectors S_c and S_i constructed for the current and the ith neighboring range cells from the all M samples over the CIT,

$$S_c = [s_{c_i}(0), s_{c_i}(1), ..., s_{c_i}(M-1)]^T.$$

(17)

$$S_i = [s_{n_i}(0), s_{n_i}(1), ..., s_{n_i}(M-1)]^T.$$

(18)

Then, the covariance matrix of clutter and external noise can be estimated by

$$R = \frac{\sum_{i=1}^{N} |\eta_i|^\gamma S_i S_i^H}{\sum_{i=1}^{N} |\eta_i|^\gamma},$$

(19)

where

$$\eta_i = \frac{S_c^H S_i}{\|S_c\| \|S_i\|}$$

(20)

is the correlation coefficient between the received signal vectors at the current range cell and the ith neighboring cell, and γ is a positive scalar, typically takes value between 1 and 2.

The introduction of term $|\eta_i|^\gamma$ in (19) allows weighting differently the contributions of the neighboring range cells depending on their respective correlation coefficients with the current range cell. By doing this, the contributions from less correlated range cells can be effectively eliminated.

The SVD of R can be written as

$$R = UVU^H,$$

(21)

where U is a unitary matrix and V is a diagonal matrix. Columns of U are eigenvectors of R, and the elements in the diagonal of V are the corresponding eigenvalues. As the clutter is the dominant component in the received signal, the eigenvectors $u_1, u_2, ..., u_M$ corresponding to the M largest eigenvalues can be reasonably associated to the clutter. The projection of the received signal to the orthogonal subspace of the clutter,

$$S_{proj} = (I - \sum_{i=1}^{M} u_{n_i} u_{n_i}^H) S_c , \qquad (22)$$

results in clutter-suppressed signal.

In (17), because the number of neighboring range cells is usually smaller than the dimension of the variance matrix R to be estimated, it is rank deficient. By considering the existence of thermal noise, the full-rank covariance matrix R_1 of clutter and noise can be estimated as

$$R_1 = R + \sigma^2 I , \qquad (23)$$

where σ^2 is the noise variance which can be roughly estimated, and I is the identity matrix. Performing singular value decomposition (SVD) of R_1 yields

$$R_1 = U_1 V_1 U_1^H = \sum_{i=1}^{N} \lambda_i \tilde{u}_i \tilde{u}_i^H = \sum_{i=1}^{N} \lambda_i P_i \qquad (24)$$

where λ_i is the i-th largest eigenvalue of R_1, $\tilde{u}_i$ is its eigen vector, and $P_i = \tilde{u}_i \tilde{u}_i^H$ is the projection operator to the subspace generated by $\tilde{u}_i$. From (21), we know that more clutter energy distributed in the subspace vector $\tilde{u}_i$ corresponding to a larger eigenvalue λ_i. The following algorithm provides an efficient way to remove strong clutter without any knowledge of signal,

$$S_{proj} = \sum_{i=1}^{N} f(\lambda_i) P_i S_c , \qquad (25)$$

where $f(\lambda_i)$ is a weighting function that takes a smaller value for a larger value of λ_i. In this paper, $f(\lambda_i)$ is chosen as

$$f(\lambda_i) = \frac{1}{\lambda_i} . \qquad (26)$$

Therefore, the signal vector, after the adaptive clutter rejection, becomes

$$S_{proj} = \sum_{i=1}^{N} f(\lambda_i) P_i S_c = \sum_{i=1}^{N} \frac{1}{\lambda_i} P_i S_c = R_1^{-1} S_c = (R + \sigma^2 I)^{-1} S_c . \qquad (27)$$

The noise variance estimate σ^2 controls the rejection level against the clutter components.

5. Simulation Results

In this section, the performance of the proposed algorithms for maneuvering target detection is shown by some simulation results. The signal data coming from maneuvering targets is generated based on the signal model (1) and then added to the raw OTHR clutter data. The radar working frequency is 20MHz. There are 54 range cells in the data. The coherent integration time (CIT) is $T_c = 12.3$ seconds. The velocity and acceleration of targets in the range direction are from $40\, m/s$ and 3 m/s^2 respectively. The signal to clutter ratio is about -53.5 dB.

In our simulations, the following steps are implemented. For the received signal, matched filtering and range compression are first implemented in the range direction. Then, the signal subspace clutter rejection algorithm is applied to remove the clutter where $\gamma=1$ is used. At last ACT is used to the clutter-rejected signal for target detection.

The signal waveforms before and after adaptive signal subspace clutter rejection to the range cell that contains target are shown in Fig1.(a). We can see that the clutter energy is removed about 15 dB by using the signal subspace algorithm. The results can also be verified by the results of Fig.1(b) and Fig.1(c), which are the mesh of range-Doppler results to the data before and after clutter rejection by adaptive subspace clutter rejection algorithm. It is noted that the clutter suppression at edge range cells is not as effective as the other cells because less neighboring range cells are available for clutter subspace estimation.

The processing results with different methods are shown in Fig.2. The target can not be detected from the range-Doppler results obtained by using the Fourier transform to the pre-clutter rejection data, which is shown in Fig2.(a). Because the Fourier transform spreads the target energy of the maneuvering targets, as shown in Fig. 2(b), the target is still undetectable even after the clutter rejection and SCR enhancement. Instead of the Fourier transform in Fig.2(b), ACT is used in Fig.2(c). The target, however, can be easily detected now in Fig.2(c) at range 2250 km with Doppler about -4 Hz. The amplitudes of the signal in the range cell containing the target are shown in Figs.3(a)-(c) for the Fourier transform without

32

clutter rejection, the Fourier transform with clutter rejection, and the ACT with clutter rejection, respectively. From Fig.3(a), we can see that the clutter amplitude of the main lobe around 0 Hz is about 20 dB higher than that of the side lobes including the region around −5 Hz where the target is located. In Fig.3(b), although the clutter amplitude of the main lobe is reduced by about 15 dB and the side lode is reduced about 5 to 10 dB, the target still can not be detected. But in Fig.3(c), the target energy is focused. The amplitude of the target signal is about 4 dB higher than that of the clutter in target's neighboring frequency bands.
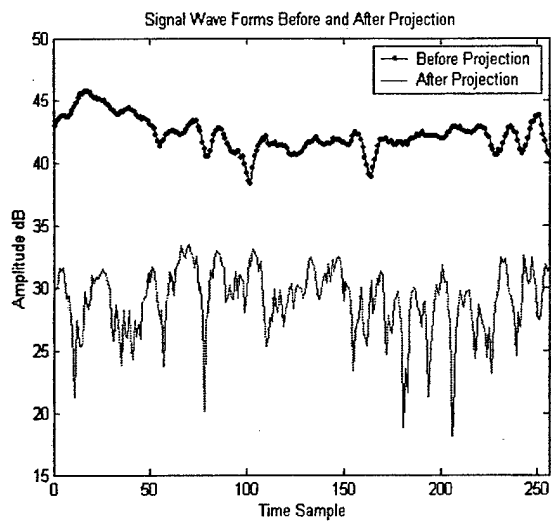
6. Conclusion

In this paper, an adaptive clutter rejection algorithm was proposed to maneuvering target detection in OTHR systems. This algorithm can reduce clutter energy by about 15 to 20 dB with negligible distortion to the waveform of the signal returned from maneuvering targets. An adaptive chirplet transform algorithm was applied to the clutter-mitigated signal for improved Doppler processing. Simulation results showed that the proposed method substantially enhances the target detection ability. Particularly, several simulation examples showed that the proposed method can successfully detect weak target signals where other methods can not be used directly with adaptive chirplet transform for maneuvering target detection.
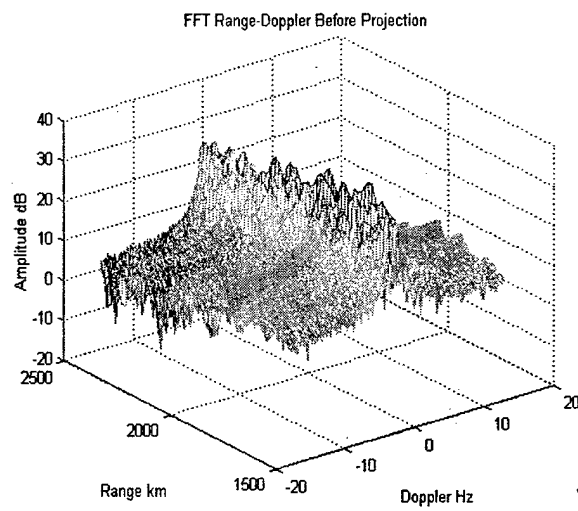
References

[1] J. M. Headrick and J. F. Thomason, "Naval applications of high frequency over-the-horizon radar," *Nav. Eng. J.*, vol.108, pp.353-359, May 1996

[2] B. T. Root, "HF-over-the-horizon radar ship detection with short dwells using clutter cancellation," *Radio Science*, vol.33 no. 4, pp.1095-1111, 1998.

[3] G. D. McNeal, "The high-frequency environment at the ROTHR Amchitka radar site," *Radio Science*, vol.30, pp.739-746, May-June 1995.

[4] R. Anderson and J. Krolik, "Target localization and track association for over-the-horizon radar with a statistical ionospheric model," *Technical Report*, Department of Electrical and Computer Engineering, Duke University, July 23, 1999.

[5] R. H. Anderson and J. L. Krolik, "Over-the horizon radar target location using a hidden markov model estimated from ionosonde data," *Radio Science*, vol.33 no. 4, pp.1199-1213, 1998.

[6] B. Boashash, "Estimating and interpreting the instantaneous frequency of a signal: Part 1&II," *Proc. IEEE*, vol.80, pp.519-538, April 1992.

[7] L. Cohen, *Time-Frequency Analysis*, Englewood Cliffs, NJ: Prentice Hall, 1995.

[8] S. Qian and D. Chen, *Joint Time-Frequency Analysis*, Englewood Cliffs, NJ: Prentice Hall, 1996.

[9] S. Qian, D. Chen, and Q. Yin, "Adaptive chirplet based signal approximation," *Proc. ICASSP'98*, Seattle, WA, 1998.

[10] V. C. Chen and S. Qian, "Joint time-frequency transform for radar range-Doppler imaging," *IEEE Trans. Aerospace and Electronic Systems*, vol.34, May 1998.

[11] L. Trintinalia and H. Ling, "Joint time-frequency transform for radar-Doppler imaging," *IEEE Trans. Aerospace and Electronic Systems*, vol. 34, May 1998.

[12] V. C. Chen and W. J. Miceli, "Time-varying spectral analysis for radar imaging of maneuvering targets," *IEE Proceedings on Radar Sonar and Navigation*, vol. 145, Special Issue on radar Signal Processing, pp. 262-268, 1998.
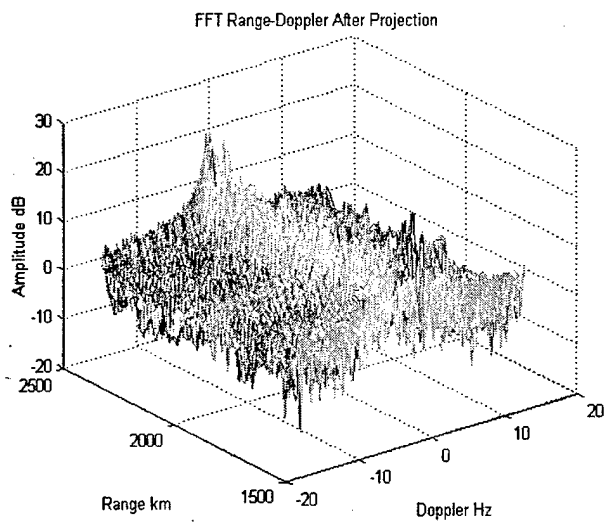
[13] G. Wang and Z. Bao, "Inverse synthetic aperture radar imaging of maneuvering targets based on chirplet decomposition," *Optical Engineering,* vol. 39, no.9, pp. 1534-1541, 1999.

[14] S. Barbarossa and A. Farina, "Detection and imaging of moving target with synthetic aperture radar. Part 2: Joint time-frequency analysis and Wigner-Ville distribution," *IEE Proc. on Radar Sonar and Navigation,* vol. 139, pp.89-97, 1992.

[15] S. Mann and S. Haykin, "The chirplet transform: physical considerations," *IEEE Trans. Signal Processing,* vol.43, pp.2745-2761, 1995.

[16] K. Harmanci and J.Krolik, "Adaptive temporal processing for equatorial spread Doppler clutter suppression," *Proc. IEEE Workshop on Statistical Signal and Array Processing,* Pocono, PA, pp. 245-249, Aug. 2000.

[17] S. Kraut, K. Harmanci, and J. Krolik, "Space-time adaptive processing for over-the-horizon spread-Doppler clutter estimation," *Proc. ICASSP'2000,* pp. 3041-3044, Istanbul, Turkey, June 2000.

[18] L. J. Nickisch, "Non-uniform motion and extended media effects on the mutual coherence function: an analytic solution for spaced frequency, position, and time," *Radio Science,* vol.27, pp. 9-22, 1992.

[19] S. Haykin, *Adaptive Filter Theory,* Third edition, Englewood Cliffs, NJ: Prentice Hall, 1996.

[20] Z. Bao, G. Wang and L. Luo, "Inverse synthetic aperture radar imaging of maneuvering targets," *Optical Engineering,* vol. 37, no. 5, pp.1582-1588, 1998.

[21] M. Skolnik, Radar Handbook, Second edition, McGraw-Hill Publishing Company, 1990.

[22] J. Headrick, and M. Skolnik, "Over-the-Horizon Radar in the HF Band," *Proc. Of the IEEE,* vol. 62, no. 6, pp. 664-673, 1974.

(a)

(b)

(c)

Fig. 1. Signal amplitude before and after clutter rejection.

FFT Range-Doppler Before Projection

(a)

FFT Range-Doppler After Projection

(b)

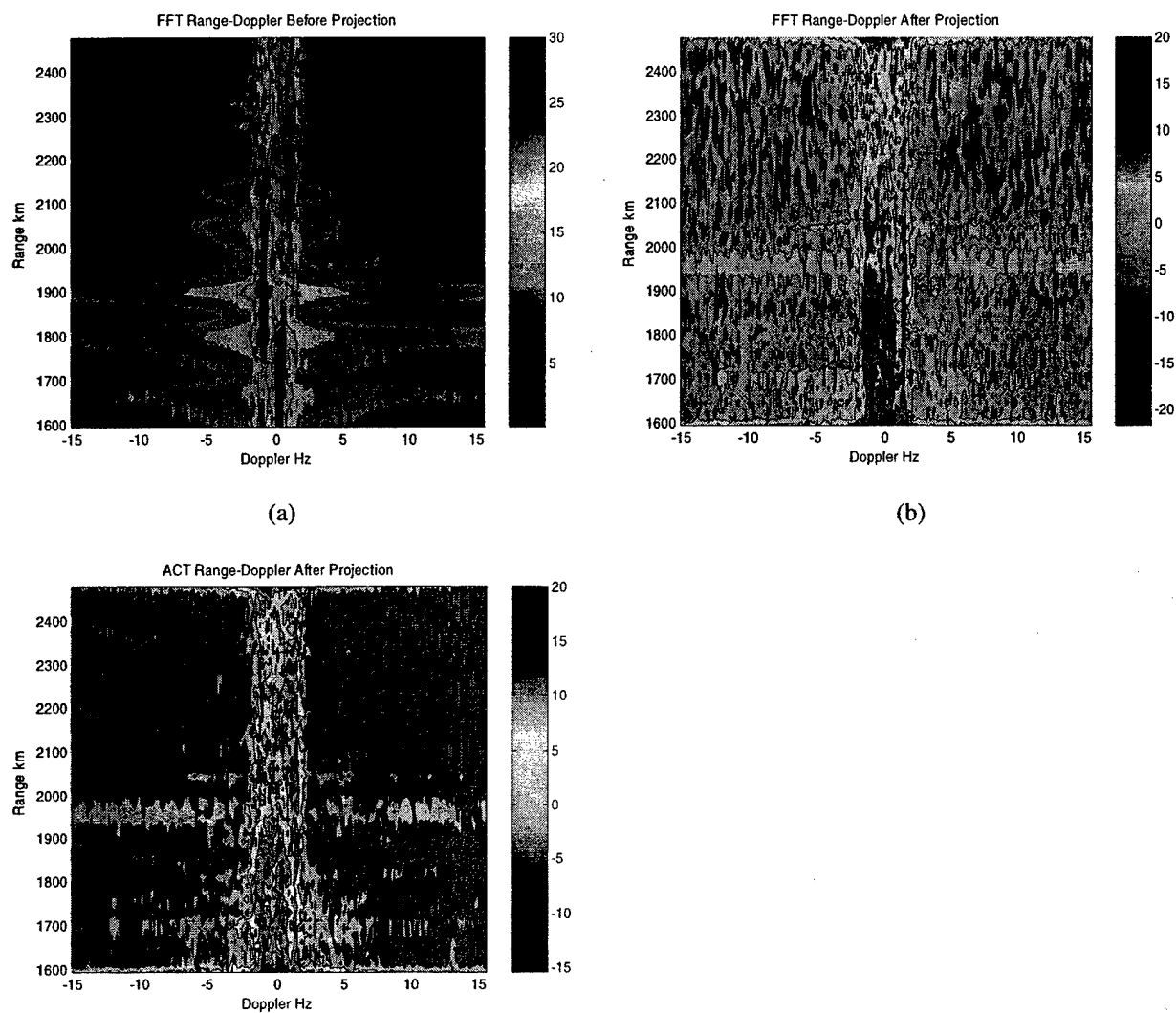**ACT Range-Doppler After Projection**

Fig. 2. OTHR results with different processing methods
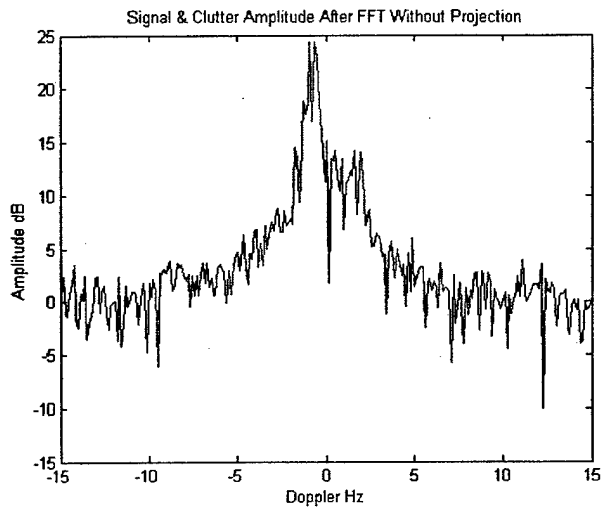
(a)
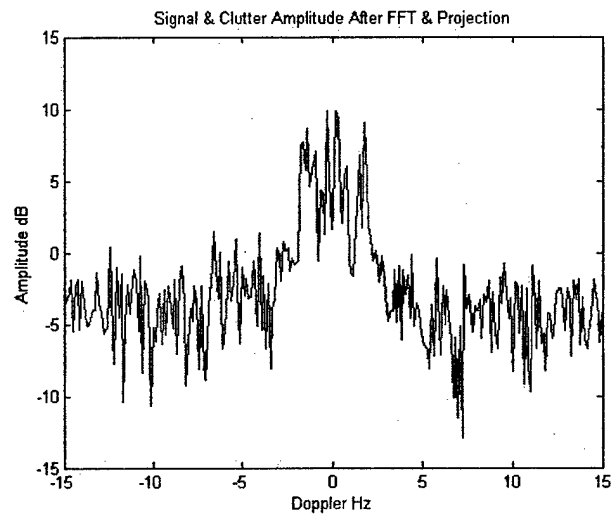
(b)
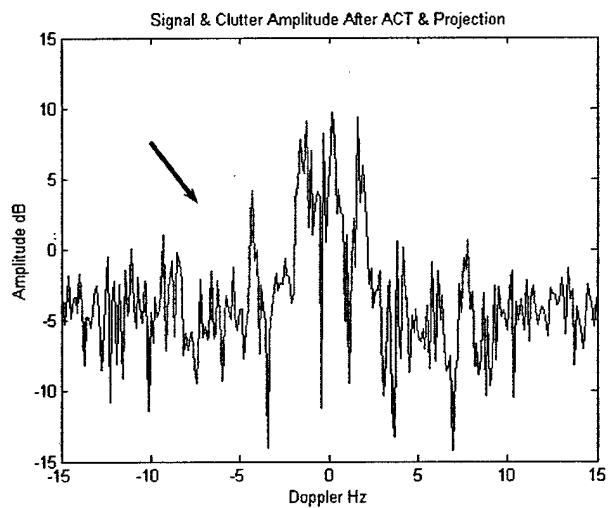
(c)

Fig. 3. The processing results with different method to the range containing targets

Bilinear Signal Synthesis Using Polarization Diversity

Moeness G. Amin and Yimin Zhang

Center for Advanced Communications

Villanova University, Villanova, PA 19085, USA

Abstract

Bilinear synthesis of nonstationary signals impinging on a multi-antenna receiver has been recently introduced. The distinction in the spatial signatures of the sources provides a vehicle to reduce noise and source signal interactions in the time-frequency domain, and hence improves signal synthesis. In this letter, we utilize another form of diversity for enhanced source time-frequency signal representations. It is shown that cross-polarization antennas can be used to mitigate crossterms via simple polarization averaging.

I. Introduction

Time-frequency distributions (TFDs) have been found useful in the analysis and classification of nonstationary signals [1], [2]. In [3], it is shown that the array manifold can be used to improve syntheses of signals with rapid time-varying frequency characteristics. In essence, averaging TFDs across different array sensors trades off the spatial dimension for enhanced auto-source TFDs. Spatial averaging mitigates the cross-source time-frequency (t-f) terms as well as reduces the noise contribution.

When the receiver is not equipped with an antenna array, or the array is of small aperture, the spatial averaging of TFDs proposed in [3] will no longer be effective or applicable. A possible alternative is to use cross-polarization antennas where the polarization dimension can be utilized to enhance t-f signature estimation and subsequently leads to improved signal synthesis performance. The polarization-based t-f signal synthesis can be used for a single as well as multiple antennas. In this letter, we restrict our discussion to the simple case of a single pair of cross-polarization antennas. The generalization to applications of multi-sensor receivers is straightforward and is addressed in [4].

Signal polarization properties have been commonly utilized in wireless communications and synthetic aperture radars (SARs) [5], [6]. Distinct polarization signatures of different sources can be observed when the sources have different transmitter polarizations or distinct channel characteristics.

This letter is organized as follows. The signal model is presented in Section II. Section III proposes the polarization averaging for t-f signal synthesis. The analogy between the proposed method and the array averaging is also considered. Numerical simulations are given in Section IV.

II. Signal Model

The discrete-time data received at a cross-polarization antenna, which receives two orthogonal polarizations (e.g., vertical and horizontal polarizations), is expressed in the following vector format

$$\mathbf{x}(t) = \left[x^{[p]}(t) \quad x^{[q]}(t) \right]^T, \tag{1}$$

where $[p]$ and $[q]$ represent the two orthogonal polarizations, and T denotes transpose.

The following expression

$$D_{x^{[i]}x^{[k]}}(t,f) = \int\limits_{-\infty}^{\infty} \int\limits_{-\infty}^{\infty} \phi(t-u,\tau)x^{[i]}(t+\frac{\tau}{2})(x^{[k]}(t-\frac{\tau}{2}))^{*}e^{-j2\pi ft}dud\tau \qquad (2)$$

defines the auto- ($i = k$) and cross-polarized ($i \neq k$) TFDs of the two polarizations, where t and f are the time and the frequency indeces, respectively, and $\phi(t,\tau)$ is the time-frequency kernel [7]. Each of i and k takes either value of the polarization index p or q. The auto- and cross-polarized TFDs can be combined to form the following 2×2 polarization TFD matrix,

$$\mathbf{D_{xx}}(t,f) = \int\limits_{-\infty}^{\infty} \int\limits_{-\infty}^{\infty} \phi(t-u,\tau)\mathbf{x}(t+\frac{\tau}{2})\mathbf{x}^{H}(t-\frac{\tau}{2})e^{-j2\pi ft}dud\tau. \qquad (3)$$

where superscript ^{H} denotes transpose conjugation. The diagonal entries of $\mathbf{D_{xx}}(t,f)$ are the auto-polarized TFDs, whereas the off-diagonal elements are cross-polarized TFDs.

Assume L source signals $s_l(t), l = 1, ..., L$, are incident on the antenna. The received data for each polarization is the linear combination of the same polarization components of the source signals and noise. That is,

$$x^{[i]}(t) = \sum_{l=1}^{L} a_l^{[i]}s_l(t) + n^{[i]}(t), \quad i = p,q, \qquad (4)$$

where $a_l^{[i]}$ represents the mixing coefficient of the lth source along the ith polarization, and $n^{[i]}(t)$ is the noise component at the same polarization. In the vector form, $\mathbf{x}(t)$ can be decomposed into the following terms

$$\mathbf{x}(t) = \mathbf{y}(t) + \mathbf{n}(t) = \mathbf{As}(t) + \mathbf{n}(t) = \sum_{l=1}^{L} \mathbf{a}_l s_l(t) + \mathbf{n}(t), \qquad (5)$$

where $\mathbf{a}_l = [a_l^{[p]}\, a_l^{[q]}]^T$, $\mathbf{A} = [\mathbf{a}_1, \ldots, \mathbf{a}_L]$, $\mathbf{s}(t) = [s_1(t), \ldots, s_L(t)]^T$, and $\mathbf{n}(t) = [n^{[p]}(t)\, n^{[q]}(t)]^T$. Because of the ambiguity with respect to the signal strength and the propagation attenuation, it is convenient to assume that $\|\mathbf{a}_l\|_2^2 = 2$, $l = 1, \cdots, L$, and the propagation attenuation scalar is absorbed in $s_l(t)$. The noise elements are modelled as stationary and white complex Gaussian processes with zero mean and variance σ^2 in each polarzation, i.e.,

$$E\left[\mathbf{n}(t+\tau)\mathbf{n}^{H}(t)\right] = \sigma^2\delta(\tau)\mathbf{I}_2, \qquad (6)$$

where $\delta(\tau)$ is the Kronecker delta and $\mathbf{I}_N$ denotes the $N \times N$ identity matrix.

41

III. Polarization Averaging

It is clear from Section II that the signal model of the cross-polarization antenna case is similar to that of a two-antenna array. The only difference is that the source polarization vector $\mathbf{a}_l$ is used in place of the source spatial signature, or steering vector. Accordingly, polarization averaging can be equally effective as spatial averaging in mitigating the TFD crossterms.

From eqns. (2) and (4), the auto-polarization TFD of $x^{[i]}(t)$ is given by

$$D_{x^{[i]}x^{[i]}}(t,f) = \sum_{l=1}^{L}\sum_{m=1}^{L} a_l^{[i]}(a_m^{[i]})^* D_{s_l s_m}(t,f) + D_{n^{[i]}n^{[i]}}(t,f), \quad i = p,q, \tag{7}$$

where $D_{s_l s_m}(t,f)$ represents the auto-source TFD (if $l=m$) or the cross-source TFD (if $l \neq m$). The presence of cross-source terms often obscures the true power localization over time and frequency.

Averaging the auto-polarization TFDs over the two polarization branches yields

$$
\begin{aligned}
\bar{\mathbf{W}}(t,f) &= \frac{1}{2}\sum_{i=p}^{q} D_{x^{[i]}x^{[i]}}(t,f) \\
&= \sum_{i=1}^{L}\sum_{j=1}^{L}\left(\frac{1}{2}\sum_{i=p}^{q} a_l^{[i]}(a_m^{[i]})^*\right) D_{s_l s_m}(t,f) + \frac{1}{2}\sum_{i=p}^{q}[D_{n^{[i]}n^{[i]}}(t,f)] \\
&= \sum_{i=1}^{L}\sum_{j=1}^{L}\left(\frac{1}{2}\mathbf{a}_m^H \mathbf{a}_l\right) D_{s_l s_m}(t,f) + \frac{1}{2}\sum_{i=p}^{q}[D_{n^{[i]}n^{[i]}}(t,f)].
\end{aligned}
\tag{8}
$$

In eqn. (8), $\mathbf{a}_m^H \mathbf{a}_l$ is the inner product of the polarization signatures $\mathbf{a}_m$ and $\mathbf{a}_l$. Define the polarization correlation coefficient

$$\beta_{lm} = \frac{1}{2}\mathbf{a}_m^H \mathbf{a}_l, \tag{9}$$

Accordingly, eqn. (8) can be expressed as

$$\bar{\mathbf{W}}(t,f) = \sum_{i=1}^{L}\sum_{j=1}^{L} \beta_{lm} D_{s_l s_m}(t,f) + \frac{1}{2}\sum_{i=p}^{q}[D_{n^{[i]}n^{[i]}}(t,f)]. \tag{10}$$

The above equation shows that $\bar{\mathbf{W}}(t,f)$ is a linear combination of the auto- and cross-polarization TFDs of all signal arrivals. It is straightforward to show that for the lth and the mth sources,

$$|\beta_{lm}| \leq 1, \quad \text{if } l \neq m \quad \text{and} \quad \beta_{lm} = 1, \quad \text{if } l = m, \tag{11}$$

indicating that the constant coefficients in (10) for the auto-polarization TFDs are always greater than, or at least equal to, those for the cross-polarization TFDs. For sources with distinct polarizations, $|\beta_{lm}| \ll 1$, leading to significant suppression of crossterms, and thereby enhancing the signal signature estimation.

An interesting case arises when two signals have orthogonal polarization signatures, i.e., $\beta_{lm} = 0$ for $l \neq m$. In this case, the crossterms between these two source signals will be entirely eliminated and only the autoterms will be maintained.

The t-f kernel in eqns. (2) and (3), which introduces temporal averaging of the local autocorrelation functions at consecutive time samples, can be selected to reduce the TFD noise effect for the single antenna case, as discussed in [8], [9]. However, even without kernel smoothing, the polarization averaging in eqn. (10), similar to spatial averaging [10], decreases the noise variance and its interaction with the signal components beyond that achieved in a single antenna (polarization) case. Once the polarization averaging is performed and the t-f signature is identified, we can then proceed with the bilinear syntheses using the methods described in [2].

It is noted that, although the model used allows for L source signals to be present, there are only two dimensions of polarization diversity for a single cross-polarization antenna. Therefore, when $L > 2$, while the crossterms between different source signals can still be substantially mitigated, it becomes impossible to completely eliminate all the crossterms unless more sensors are used.

IV. Simulation Results

In this section, we provide computer simulations to demonstrate the improvement gained by the proposed technique in the reduction or elimination of crossterms and signal synthesis. Two high-order frequency modulated signals are considered on a dual-polarization dipole. Their polarizations are assumed to be orthogonal, with the following mixing matrix:

$$\mathbf{A} = \begin{bmatrix} 1 & 1 \\ 1 & -1 \end{bmatrix}.$$

The length of the signal sequence is set to $N = 256$. The additive noise is zero mean, Gaussian distributed, and white. The input signal-to-noise ratio (SNR) is 3 dB.

With the presence of high-level noise and close t-f signatures, it is very difficult to identify these t-f signatures when only a single-polarization sensor is used. Fig. 1 shows the extended discrete-time Wigner-Ville distribution (EDTWVD) [11] of the data received at the vertically polarized antenna. However, as evident from Fig. 2, the t-f signatures of the two signals can be revealed when polarization averaging is applied. Fig. 2 shows that the crossterm between the two signals are completely eliminated and the variance of noise terms is reduced. Masking the first signal and applying standard signal synthesis techniques yield a high quality signal recovery. Fig. 3 shows the TFD of the synthesized signal waveform of the first signal.
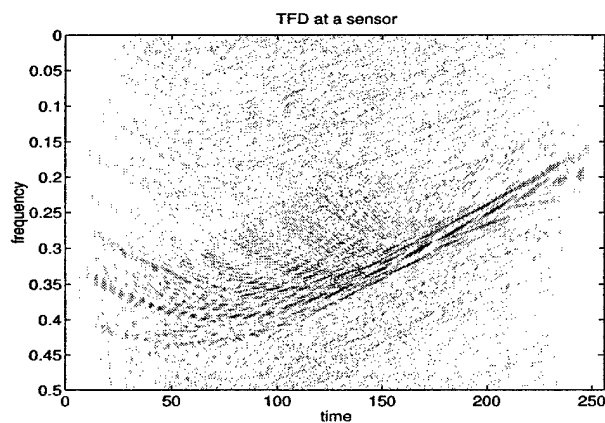

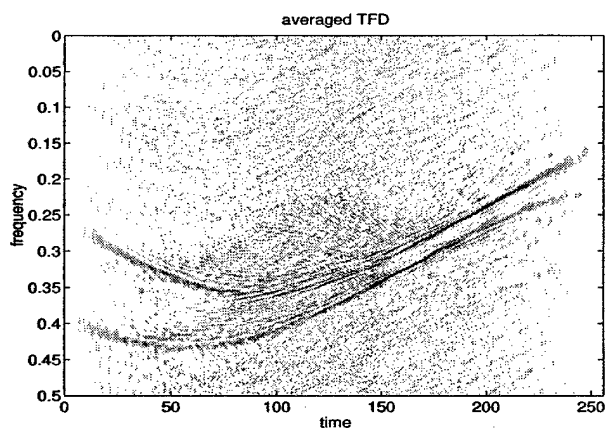Fig. 1. EDTWVD computed from the signal received at the vertical polarization antenna.

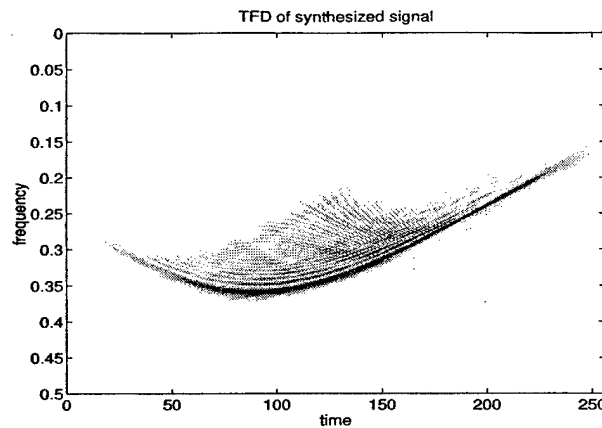Fig. 2. EDTWVD averaged over two polarizations.

Fig. 3. EDTWVD of the synthesized waveform of the first signal.

V. Conclusion

Polarization averaging allows effective crossterm reduction and autoterm enhancement, aiding source time-frequency signature estimations and waveform recovery. Averaging TFDs across polarizations can be performed concurrently with TFD averaging across the array, thereby utilizing both spatial and polarization diversity in syntheses of nonstationary signals. However, polarization averaging can be applied alone if the difference in the source spatial signatures is insufficient for crossterm reduction, or the receiver is not equipped with antenna arrays.

References

[1] B. Boashash, "Time-frequency signal analysis," in S. Haykin ed., *Advances in Spectrum Analysis and Array Processing*, vol. 1, Ch. 9, pp. 21–68, Englewood Cliffs, NJ: Prentice Hall, 1990.

[2] F. Hlawatsch and G. Boudreaux-Bartles, "Linear and quadratic time-frequency signal representations," *IEEE Signal Processing Magazine*, vol. 9, no. 2, pp. 21–68, April 1992.

[3] W. Mu, M. G. Amin, and Y. Zhang, "Bilinear signal synthesis in array processing," *IEEE Trans. Signal Processing*, vol. 51, no. 1, pp. 90-100, Jan. 2003.

[4] Y. Zhang, M. G. Amin, and B. A. Obeidat, "The spatial polarimetric time-frequency distributions and their applicaiton to direction-of-arrival estimation," *Proc. SPIE*, vol. 5205, Aug. 2003.

[5] J. D. Gibson, *The Mobile Communications Handbook*, CRC Press, 1996.

[6] F. Sadjadi, "Improved target classification using optimum polarimetric SAR signatures," *IEEE Trans. Aerospace and Electronic Systems*, vol. 38, no. 1, pp. 38 –49, Jan. 2002.

[7] L. Cohen, *Time–Frequency Analysis*, Englewood Cliffs, NJ: Prentice Hall, 1995.

[8] M. G. Amin, "Minimum-variance time-frequency distribution kernels for signals in additive noise," *IEEE Trans. Signal Processing*, vol. 44, no. 9, pp. 2352–2356, Sept. 1996.

[9] LJ. Stankovic, "Analysis of noise in time-frequency distributions," *IEEE Signal Processing Letters*, vol. 9, no. 9, pp. 286 – 289, Sept. 2002.

[10] Y. Zhang, A. R. Lindsey, and M. G. Amin, "Combined synthesis and projection techniques for jammer suppression in DS/SS communications," *Proc. ICASSP*, Orlando, FL, May 2002.

[11] J. Jeong and W. Williams, "Time–varying filtering and signal synthesis," in B. Boashash, ed., *Time–Frequency Signal Analysis — Methods and Applications*, Longman Cheshire, 1995.

Spatial Time-Frequency Distributions:

Theory and Applications

Moeness G. Amin and Yimin Zhang

Center for Advanced Communications, Villanova University, Villanova, PA 19085

Gordon J. Frazer

ISR Division, DSTO, Edinburgh, Australia

Alan R. Lindsey

Air Force Researcg Lab, Rome, NY 13441

Abstract

This chapter presents a comprehensive treatment of the hybrid area of time-frequency distribution (TFD) and array signal processing. The application of quadratic time-frequency distributions to sensor signal processing has recently become of interest, and it was necessitated by the need to address important problems related to processing nonstationary signals incident on multi-antenna receivers. Over the past few years, major contributions have been made to improve direction finding and blind source separation using time-frequency signatures. This improvement has cast quadratic time-frequency distributions as a key tool for source localization and signal recovery, and put bilinear transforms at equal footing with second-order and higher-order statistics as bases for effective spatial-temporal signal processing. This chapter discusses the advances made through time-frequency analysis in direction-of-arrival estimation, signal synthesis, and near-field source characterization.

I. Introduction

Time-frequency distributions (TFDs) are used in various applications, including speech, biomedicine, sonar, radar, GPS, and geophysics. Over the past two decades, most of the work on quadratic TFDs has focused on the mono-component and multi-component temporal signal structures and the corresponding time-frequency (t-f) signatures. This work has led to major advances in nonstationary signal analysis and processing. Information on the signal instantaneous frequency and instantaneous bandwidth obtained from the t-f domain has allowed improved separation, suppression, classification, identification, and detection of signals with time varying spectra [1], [2], [3], [4], [5], [6].

Applications of the quadratic distributions to array signal processing began to flourish in the mid-nineties. The main objective was to enhance direction-finding and blind source separation of nonstationary signals using their t-f signatures. Another important but different objective was to characterize near-field and far-field emitters based on their spatial signatures. In order to achieve both objectives, new definitions and generalization of quadratic distributions were in order.

The spatial time-frequency distribution (STFD) has been introduced to describe the mixing of nonstatioanry signals at the different sensors of the array. The relationship between the TFDs of the sensors to the TFDs of the individual source waveforms is defined by the steering, or the array, matrix, and was found to be similar to that encountered in the traditional data covariance matrix approach to array processing. This similarity has allowed a rapid progress in nonstationary array processing from the TFD perspective [7].

This chapter discusses two fundamental formulations to incorporate the spatial information into quadratic distributions. One formulation is based on STFDs and the localization of the signal arrivals in the t-f domain. The corresponding analysis, theory, and applications are covered in the first six sections of this Chapter. Section VII deals with another formulation, in which the quadratic distribution of the spatial signal across the array is computed. This sensor-angle distribution (SAD) localizes the source angle at each sensor, and is the dual in sensor number and angle to Cohen's class of time-frequency distributions. The SAD is particularly appropriate for characterizing sources and scatter in the near-field of an array. Sources arriving from the far-field have the same angle at each sensor. In con-

trast, sources in the near-field have differing angle at each sensor, and a full sensor-angle distribution provides a complete characterization of the near-field source and scatter environment. Knowledge of this characterization can be important when calibrating arrays of sensors placed in a non-homogeneous environment, such as a radar or communications array deployed in a built-up environment and surrounded by other metallic structures that are not part of the array.

II. Spatial Time-Frequency Distributions

A. Signal Model

In narrowband array processing, when n signals arrive at an m-element (sensor) array, the linear data model

$$\mathbf{x}(t) = \mathbf{y}(t) + \mathbf{n}(t) = \mathbf{A}\mathbf{d}(t) + \mathbf{n}(t) \tag{1}$$

is commonly assumed, where the $m \times n$ spatial matrix $\mathbf{A} = [\mathbf{a}_1, \cdots, \mathbf{a}_n]$ represents the mixing matrix or the steering matrix. In direction finding problems, we require $\mathbf{A}$ to have a known structure, and each column of $\mathbf{A}$ corresponds to a single arrival and carries a clear bearing. For blind source separation problems, $\mathbf{A}$ is a mixture of several steering vectors, due to multipaths, and its columns may assume any structure.

The mixture of the signals at each sensor renders the elements of the $m \times 1$ data vector $\mathbf{x}(t)$ to be multicomponent signals, whereas each source signal $d_i(t)$ of the $n \times 1$ signal vector $\mathbf{d}(t)$ is typically a monocomponent signal. $\mathbf{n}(t)$ is an additive noise vector whose elements are modeled as stationary, spatially and temporally white, zero-mean complex Gaussian random processes, independent of the source signals. That is,

$$E[\mathbf{n}(t + \tau)\mathbf{n}^H(t)] = \sigma\delta(\tau)\mathbf{I} \quad \text{and} \quad E[\mathbf{n}(t + \tau)\mathbf{n}^T(t)] = \mathbf{0} \quad \text{for any } \tau \tag{2}$$

where $\delta(\tau)$ is the delta function, $\mathbf{I}$ denotes the identity matrix, σ is the noise power at each sensor, superscript ^{H} and ^{T}, respectively, denote conjugate transpose and transpose, and $E(\cdot)$ is the statistical expectation operator.

B. Spatial Time-Frequency Distributions

We first review the definition and basic properties of the spatial time-frequency distributions (STFDs). STFDs based on Cohen's class of time-frequency distribution (TFD) were

introduced in [8] and their applications to direction finding and blind source separation have been discussed in [9], [10] and [8], [11], respectively.

The discrete form of TFD of a signal $x(t)$ is given by

$$D_{xx}(t,f) = \sum_{v=-\infty}^{\infty} \sum_{l=-\infty}^{\infty} \phi(v,l)x(t+v+l)x^*(t+v-l)e^{-j4\pi fl}, \tag{3}$$

where $\phi(v,l)$ is a kernel function and * denotes complex conjugate. The STFD matrix is obtained by replacing $x(t)$ by the data snapshot vector $\mathbf{x}(t)$,

$$\mathbf{D_{xx}}(t,f) = \sum_{v=-\infty}^{\infty} \sum_{l=-\infty}^{\infty} \phi(v,l)\mathbf{x}(t+v+l)\mathbf{x}^H(t+v-l)e^{-j4\pi fl}, \tag{4}$$

Substitute (1) into (4), we obtain

$$\mathbf{D_{xx}}(t,f) = \mathbf{D_{yy}}(t,f) + \mathbf{D_{yn}}(t,f) + \mathbf{D_{ny}}(t,f) + \mathbf{D_{nn}}(t,f). \tag{5}$$

We note that $\mathbf{D_{xx}}(t,f)$, $\mathbf{D_{yy}}(t,f)$, $\mathbf{D_{yn}}(t,f)$, $\mathbf{D_{ny}}(t,f)$, and $\mathbf{D_{nn}}(t,f)$ are matrices of dimension $m \times m$. Under the uncorrelated signal and noise assumption and the zero-mean noise property, the expectation of the crossterm STFD matrices between the signal and noise vectors is zero, i.e., $E[\mathbf{D_{yn}}(t,f)] = E[\mathbf{D_{ny}}(t,f)] = \mathbf{0}$. Accordingly,

$$\begin{aligned} E[\mathbf{D_{xx}}(t,f)] &= \mathbf{D_{yy}}(t,f) + E[\mathbf{D_{nn}}(t,f)] \\ &= \mathbf{A}\mathbf{D_{dd}}(t,f)\mathbf{A}^H + E[\mathbf{D_{nn}}(t,f)], \end{aligned} \tag{6}$$

where the source TFD matrix

$$\mathbf{D_{dd}}(t,f) = \sum_{v=-\infty}^{\infty} \sum_{l=-\infty}^{\infty} \phi(v,l)\mathbf{d}(t+v+l)\mathbf{d}^H(t+v-l)e^{-j4\pi fl} \tag{7}$$

is of dimension $n \times n$. For narrowband array signal processing applications, the mixing matrix $\mathbf{A}$ holds the spatial information and maps the auto- and cross-TFDs of the source signals into auto- and cross-TFDs of the data.

Equation (6) is similar to the formula that has been commonly used in direction finding and blind source separation problems, relating the signal correlation matrix to the data spatial correlation matrix. In the above formulation, however, the correlation matrices are replaced by the STFD matrices. The well established results in conventional array signal processing could, therefore, be utilized and key problems in various applications of

50

array processing, specifically those dealing with nonstationary signal environments, can be approached using bilinear transformations.

Initially, only the time-frequency (t-f) points in the autoterm regions of TFD are considered for STFD matrix construction. The autoterm region refers to the t-f points along the true instantaneous frequency (IF) of each signal. The crossterms, which can intrude on the autoterms through the power in their mainlobes or/and sidelobes, were avoided. This intrusion depends on the signal temporal structures and the window size. Recently, the crossterms have also been utilized and integrated into STFDs. The effect of crossterms on direction finding and blind source separation will be discussed in IV-C and V-C, respectively. In the other parts of this chapter, it is assumed that the t-f points reside in an autoterm region, which has negligible crossterm effect.

C. Joint-Diagonalization and Time-Frequency Averaging

In the rest of this chapter, we will address the application of STFDs to direction finding and blind source separation. These applications are based on the eigendecomposition of the STFD matrix. In direction finding, the source TFD matrix must be full rank (Section V), whereas, to perform blind source separation, the source TFD matrix must be diagonal (Section IV). For either case, the STFD matrix of the data vector should be full column rank.

It is noted that the relationship (6) holds true for every (t, f) point. In order to ensure the full column rank property of the STFD matrix as well as to reduce the effect of noise, we consider multiple t-f points, instead of a single one. This allows more information of the source signal t-f signatures to be included into their respective eigenstructure formulation, and as such enhances direction finding and source separation performance. Joint-diagonalization and t-f averaging are the two main approaches that have been used for this purpose [8], [9], [12].

C.1 Joint Diagonalization

The JD can be explained by first noting that the problem of the diagonalization of a single $n \times n$ normal matrix $\mathbf{M}$ is equivalent to the minimization of the criterion [13]

$$C(\mathbf{M}, \mathbf{V}) = -\sum_i \left| \mathbf{v}_i^H \mathbf{M} \mathbf{v}_i \right|^2 \tag{8}$$

over the set of unitary matrices $\mathbf{V} = [\mathbf{v}_1, \cdots, \mathbf{v}_n]$. Hence, the JD of a set $\{\mathbf{M}_k | k = 1, \cdots, K\}$ of K arbitrary $n \times n$ matrices is defined as the minimization of the following JD criterion:

$$C(\mathbf{V}) = -\sum_k C(\mathbf{M}, \mathbf{V}) = -\sum_k \sum_i \left| \mathbf{v}_i^H \mathbf{M}_k \mathbf{v}_i \right|^2 \tag{9}$$

under the same unitary constraint. It is important to note that the above definition of JD does not require the matrix set under consideration to be exactly and simultaneously diagonalized by a single unitary matrix. This is because we do not require the off-diagonal elements of all the matrices to be cancelled by a unitary transform; a joint diagonalizer is simply a minimizer of the criterion. If the matrices in $\mathbf{M}$ are not exactly joint diagonalizable, the criterion cannot be zeroed, and the matrices can only be approximately joint diagonalized. Hence, an (approximate) joint diagonalizer defines a kind of average eigenstructure.

C.2 Joint Block-Diagonalization

For direction finding methods such as t-f MUSIC, the source TFD matrix should not be singular but not necessarily diagonal. In this case, the joint block-diagonalization (JBD) is used to incorporate multiple t-f points rather than JD [9]. The JBD is achieved by the maximization under unitary transform of the following criterion

$$C(\mathbf{U}) = \sum_k \sum_{i,l} \left| \mathbf{u}_i^H \mathbf{M} \mathbf{u}_l \right|^2 \tag{10}$$

over the set of unitary matrices $\mathbf{U} = [\mathbf{u}_1, \cdots, \mathbf{u}_n]$.

C.3 Time-Frequency Averaging

Time-frequency averaging is a linear operation that adds the STFDs over a t-f region where, typically, the desired signal is highly localized and the crossterms are negligible.

The averaged STFD is defined as

$$\mathbf{D} = \frac{1}{A} \sum_{(t,f) \in \Omega} \mathbf{D}_{\mathbf{xx}}(t,f). \tag{11}$$

where Ω is the t-f region of interest and A is a normalization constant which, for example, can be chosen as the total number of (t,f) points in the region Ω. The eigendecomposition of $\mathbf{D}$ is addressed in III-C.

III. Properties of STFDs

To understand the properties of STFDs, we consider the case of frequency modulated (FM) signals and the simplest form of TFD, namely, the pseudo Wigner-Ville distribution (PWVD) [14]. The consideration of FM signals is motivated by the fact that these signals are uniquely characterized by their IFs, and therefore, they have clear t-f signatures that can be utilized by the STFD approach. Also, FM signals have constant amplitudes.

The FM signals can be modeled as

$$\mathbf{d}(t) = [d_1(t), ..., d_n(t)]^T = [D_1 e^{j\psi_1(t)}, ..., D_n e^{j\psi_n(t)}]^T, \tag{1}$$

where D_i and $\psi_i(t)$ are the fixed amplitude and time-varying phase of ith source signal. For each sampling time t, $d_i(t)$ has an instantaneous frequency $f_i(t) = d\psi_i(t)/(2\pi dt)$.

The discrete form of PWVD of a signal $x(t)$, using a rectangular window of odd length L, is a special case of (3) and is given by

$$D_{xx}(t,f) = \sum_{\tau=-(L-1)/2}^{(L-1)/2} x(t+\tau)x^*(t-\tau)e^{-j4\pi f\tau}. \tag{2}$$

Similarly, the spatial pseudo Wigner-Ville distribution (SPWVD) matrix is obtained by replacing $x(t)$ by the data snapshot vector $\mathbf{x}(t)$,

$$\mathbf{D}_{\mathbf{xx}}(t,f) = \sum_{\tau=-(L-1)/2}^{(L-1)/2} \mathbf{x}(t+\tau)\mathbf{x}^H(t-\tau)e^{-j4\pi f\tau}. \tag{3}$$

A. Subspace Analysis for FM Signals

Analysis of the eigendecomposition of the STFD matrix is closely related to the analysis of subspace decomposition of the covariance matrix [15]. Before elaborating on this

relationship, we present the case of FM signals using the conventional covariance matrix approach.

In equation (1), it is assumed that the number of sensors is greater than the number of sources, i.e., $m > n$. Further, matrix $\mathbf{A}$ is full column rank. We further assume that the correlation matrix

$$\mathbf{R_{xx}} = E[\mathbf{x}(t)\mathbf{x}^H(t)] \tag{4}$$

is nonsingular, and the observation period consists of N snapshots with $N > m$. Under the above assumptions, the correlation matrix is given by

$$\mathbf{R_{xx}} = E[\mathbf{x}(t)\mathbf{x}^H(t)] = \mathbf{A}\mathbf{R_{dd}}\mathbf{A}^H + \sigma\mathbf{I}, \tag{5}$$

where $\mathbf{R_{dd}} = E[\mathbf{d}(t)\mathbf{d}^H(t)]$ is the source correlation matrix.

Let $\lambda_1 > \lambda_2 > \cdots > \lambda_n > \lambda_{n+1} = \lambda_{n+2} = \cdots = \lambda_m = \sigma$ denote the eigenvalues of $\mathbf{R_{xx}}$. It is assumed that λ_i, $i = 1, \cdots, n$, are distinct. The unit-norm eigenvectors associated with $\lambda_1, ..., \lambda_n$ constitute the columns of matrix $\mathbf{S} = [\mathbf{s}_1, ..., \mathbf{s}_n]$, and those corresponding to $\lambda_{n+1}, ..., \lambda_m$ make up matrix $\mathbf{G} = [\mathbf{g}_1, ..., \mathbf{g}_{m-n}]$. Since the columns of $\mathbf{A}$ and $\mathbf{S}$ span the same subspace, then $\mathbf{A}^H\mathbf{G} = \mathbf{0}$.

In practice, $\mathbf{R_{xx}}$ is unknown, and therefore should be estimated from the available data samples (snapshots) $\mathbf{x}(i)$, $i = 1, 2, ..., N$. The estimated correlation matrix is given by

$$\hat{\mathbf{R}}_{xx} = \frac{1}{N}\sum_{i=1}^{N}\mathbf{x}(i)\mathbf{x}^H(i). \tag{6}$$

Let $\{\hat{\mathbf{s}}_1, ..., \hat{\mathbf{s}}_n, \hat{\mathbf{g}}_1, ..., \hat{\mathbf{g}}_{m-n}\}$ denote the unit-norm eigenvectors of $\hat{\mathbf{R}}_{xx}$, arranged in the descending order of the associated eigenvalues, and let $\hat{\mathbf{S}}$ and $\hat{\mathbf{G}}$ denote the matrices defined by the set of vectors $\{\hat{\mathbf{s}}_i\}$ and $\{\hat{\mathbf{g}}_i\}$, respectively. The statistical properties of the eigenvectors of the sample covariance matrix $\hat{\mathbf{R}}_{xx}$ for signals modeled as independent processes with additive white noise are given in [15].

We assume that the transmitted signals propagate in a stationary environment and are mutually uncorrelated over the observation period $1 \leq t \leq N$. Subsequently, the corresponding covariance matrices are time-independent. Under these assumptions,

$$\frac{1}{N}\sum_{k=1}^{N}d_i(k)d_j^*(k) = 0 \qquad \text{for } i \neq j, \; i, j = 1, ..., n. \tag{7}$$

In this case, the signal correlation matrix is

$$\mathbf{R_{dd}} = \lim_{T \to \infty} \frac{1}{T} \sum_{t=1}^{T} \mathbf{d}(t)\mathbf{d}^H(t) = diag\left[D_i^2, \ i = 1, 2, ..., n\right] \tag{8}$$

where $diag[\cdot]$ is the diagonal matrix formed with the elements of its vector valued arguments. From the above assumptions, we have the following Lemma.

Lemma 1 [14]: For uncorrelated FM signals with additive white Gaussian noise,

a) The estimation errors $(\hat{\mathbf{s}}_i - \mathbf{s}_i)$ are asymptotically (for large N) jointly Gaussian distributed with zero means and covariance matrices given by

$$E\left[(\hat{\mathbf{s}}_i - \mathbf{s}_i)(\hat{\mathbf{s}}_j - \mathbf{s}_j)^H\right]$$
$$= \frac{\sigma}{N}\left[\sum_{\substack{k=1 \\ k \neq i}}^{n} \frac{\lambda_i + \lambda_k - \sigma}{(\lambda_k - \lambda_i)^2}\mathbf{s}_k\mathbf{s}_k^H + \sum_{k=1}^{m-n} \frac{\lambda_i}{(\sigma - \lambda_i)^2}\mathbf{g}_k\mathbf{g}_k^H\right]\delta_{i,j}, \tag{9}$$

$$E\left[(\hat{\mathbf{s}}_i - \mathbf{s}_i)(\hat{\mathbf{s}}_j - \mathbf{s}_j)^T\right] = -\frac{\sigma}{N}\frac{(\lambda_i + \lambda_j - \sigma)}{(\lambda_j - \lambda_i)^2}\mathbf{s}_j\mathbf{s}_i^T(1 - \delta_{i,j}). \tag{10}$$

where

$$\delta_{i,j} = \begin{cases} 1, & i = j, \\ 0, & i \neq j. \end{cases}$$

b) The orthogonal projections of $\{\hat{\mathbf{g}}_i\}$ onto the column space of $\mathbf{S}$ are asymptotically (for large N) jointly Gaussian distributed with zero means and covariance matrices given by

$$E\left[\left(\mathbf{SS}^H\hat{\mathbf{g}}_i\right)\left(\mathbf{SS}^H\hat{\mathbf{g}}_j\right)^H\right] = \frac{\sigma}{N}\left[\sum_{k=1}^{n} \frac{\lambda_k}{(\sigma - \lambda_k)^2}\mathbf{s}_k\mathbf{s}_k^H\right]\delta_{i,j} \stackrel{\text{def}}{=} \frac{1}{N}\mathbf{U}\delta_{i,j}, \tag{11}$$

$$E\left[\left(\mathbf{SS}^H\hat{\mathbf{g}}_i\right)\left(\mathbf{SS}^H\hat{\mathbf{g}}_j\right)^T\right] = 0 \ \text{ for all } i, \ j. \tag{12}$$

Equations (9) and (10) hold strong similarity to those of [15]. The only difference is that the term $(\lambda_i\lambda_k)$ in [15] is replaced by $\sigma(\lambda_i + \lambda_k - \sigma)$ in (9) and (10), due to the uncorrelation property (7). Equations (11) and (12) are identical to those derived in reference [15].

B. SNR Enhancement

The TFD maps one-dimensional signals in the time domain into two-dimensional signals in the t-f domain. The TFD property of concentrating the input signal around its IF

while spreading the noise over the entire t-f domain increases the effective SNR and proves valuable in the underlying problem.

The ith diagonal element of PWVD matrix $\mathbf{D_{dd}}(t, f)$ is given by

$$D_{d_i d_i}(t, f) = \sum_{\tau=-(L-1)/2}^{(L-1)/2} D_i^2 e^{j[\psi_i(t+\tau)-\psi_i(t-\tau)]-j4\pi f\tau}. \tag{13}$$

Assume that the third-order derivative of the phase is negligible over the window length L, then along the true t-f points of the ith signal, $f_i(t) = d\psi_i(t)/(2\pi dt)$, and $\psi_i(t+\tau) - \psi_i(t-\tau) - 4\pi f_i(t)\tau = 0$. Accordingly, for $(L-1)/2 \leq t \leq N - (L-1)/2$,

$$D_{d_i d_i}(t, f_i(t)) = \sum_{\tau=-(L-1)/2}^{(L-1)/2} D_i^2 = LD_i^2. \tag{14}$$

Similarly, the noise SPWVD matrix $\mathbf{D_{nn}}(t, f)$ is

$$\mathbf{D_{nn}}(t, f) = \sum_{\tau=-(L-1)/2}^{(L-1)/2} \mathbf{n}(t+\tau)\mathbf{n}^H(t-\tau)e^{-j4\pi f\tau}. \tag{15}$$

Under the spatially and temporally white assumptions, the statistical expectation of $\mathbf{D_{nn}}(t, f)$ is given by

$$E[\mathbf{D_{nn}}(t, f)] = \sum_{\tau=-(L-1)/2}^{(L-1)/2} E\left[\mathbf{n}(t+\tau)\mathbf{n}^H(t-\tau)\right]e^{-j4\pi f\tau} = \sigma\mathbf{I}. \tag{16}$$

Therefore, when we select the t-f points along the t-f signature or the IF of the ith FM signal, the SNR in the model (6) becomes LD_i^2/σ, which has an improved factor L over the one associated with model (5). The IF of the FM signals can be estimated from the employed TFD, or using any appropriate IF estimator. It is noted, however, that the STFD equation (6) provides a natural platform for the direct incorporation of any *a priori* information or estimates of the IF into direction-of-arrival (DOA) estimation.

The PWVD of each FM source has a constant value over the observation period, providing that we leave out the rising and falling power distributions at both ends of the data record. For convenience of analysis, we select those $N' = N - L + 1$ t-f points of constant distribution value for each source signal. In the case where the STFD matrices are averaged over the t-f signatures of n_o sources, i.e., a total of $n_o N'$ t-f points, the result is given by

$$\hat{\mathbf{D}} = \frac{1}{n_o N'} \sum_{q=1}^{n_o} \sum_{i=1}^{N'} \mathbf{D_{xx}}(t_i, f_{q,i}(t_i)), \tag{17}$$

where $f_{q,i}(t_i)$ is the IF of the qth signal at the ith time sample. $\mathbf{x}(t)$ is an instantaneous mixture of the FM signals $d_i(t), i = 1, \cdots, n,$ hence features the same IFs. The expectation of the averaged STFD matrix is

$$
\begin{aligned}
\mathbf{D} &= E\left[\hat{\mathbf{D}}\right] = \frac{1}{n_o N'} \sum_{q=1}^{n_o} \sum_{i=1}^{N'} E\left[\mathbf{D_{xx}}(t_i, f_{q,i}(t_i))\right] \\
&= \frac{1}{n_o} \sum_{q=1}^{n_o} \left[LD_q^2 \mathbf{a}_q \mathbf{a}_q^H + \sigma \mathbf{I}\right] = \frac{L}{n_o} \mathbf{A}^o \mathbf{R_{dd}^o} (\mathbf{A}^o)^H + \sigma \mathbf{I},
\end{aligned}
\tag{18}
$$

where $\mathbf{R_{dd}^o} = diag\,[D_i^2, i = 1, 2, \cdots, n_o]$ and $\mathbf{A}^o = [\mathbf{a}_1, \mathbf{a}_2, \cdots, \mathbf{a}_{n_o}]$ represent the signal correlation matrix and the mixing matrix formulated by considering n_o signals out of the total number of n signal arrivals, respectively.

It is clear from (18) that the SNR improvement $G = L/n_o$ (we assume $L > n_o$) is inversely proportional to the number of sources contributing to matrix $\mathbf{D}$. Therefore, from the SNR perspective, it is best to set $n_o = 1$, i.e., to select the sets of N' t-f points that belong to individual signals one set at a time, and then separately evaluate the respective STFD matrices.

This procedure is made possible by the fact that STFD-based array processing is, in essence, a discriminatory technique in the sense that it does not require simultaneous localization and extraction of all unknown signals received by the array. With STFDs, array processing can be performed using STFDs of a subclass of the impinging signals with specific t-f signatures. In this respect, the t-f based blind source separation and direction finding techniques have implicit spatial filtering, removing the undesired signals from consideration. It is also important to note that with the ability to construct the STFD matrix from one or few signal arrivals, the well known $m > n$ condition on source localization using arrays can be relaxed to $m > n_o$, i.e., we can perform direction finding or source separation with the number of array sensors smaller than the number of impinging signals. Further, from the angular resolution perspective, closely spaced sources with different t-f signatures can be resolved by constructing two separate STFDs, each corresponding to one source, and then proceed with subspace decomposition for each STFD matrix, followed by an appropriate source localization method (MUSIC, for example). The drawback using different STFD matrices separately is of course the need for repeated computations.

57

C. Signal and Noise Subspaces Using STFDs

The following Lemma provides the relationship between the eigendecompositions of the STFD matrices and the data covariance matrices used in conventional array processing.

Lemma 2 [14]: Let $\lambda_1^o > \lambda_2^o > \cdots > \lambda_{n_o}^o > \lambda_{n_o+1}^o = \lambda_{n_o+2}^o = \cdots = \lambda_m^o = \sigma$ denote the eigenvalues of $\mathbf{R}_{xx}^o = \mathbf{A}^o \mathbf{R}_{dd}^o (\mathbf{A}^o)^H + \sigma \mathbf{I}$, which is defined from a data record of a mixture of the n_o selected FM signals. Denote the unit-norm eigenvectors associated with $\lambda_1^o, ..., \lambda_{n_o}^o$ by the columns of $\mathbf{S}^o = [\mathbf{s}_1^o, ..., \mathbf{s}_{n_o}^o]$, and those corresponding to $\lambda_{n_o+1}^o, ..., \lambda_m^o$ by the columns of $\mathbf{G}^o = [\mathbf{g}_1^o, ..., \mathbf{g}_{m-n_o}^o]$. We also denote $\lambda_1^{tf} > \lambda_2^{tf} > \cdots > \lambda_{n_o}^{tf} > \lambda_{n_o+1}^{tf} = \lambda_{n_o+2}^{tf} = \cdots = \lambda_m^{tf} = \sigma^{tf}$ as the eigenvalues of $\mathbf{D}$ defined in (18). The superscript ^{tf} denotes that the associated term is derived from the STFD matrix $\mathbf{D}$. The unit-norm eigenvectors associated with $\lambda_1^{tf}, ..., \lambda_{n_o}^{tf}$ are represented by the columns of $\mathbf{S}^{tf} = [\mathbf{s}_1^{tf}, ..., \mathbf{s}_{n_o}^{tf}]$, and those corresponding to $\lambda_{n_o+1}^{tf}, ..., \lambda_m^{tf}$ are represented by the columns of $\mathbf{G}^{tf} = [\mathbf{g}_1^{tf}, ..., \mathbf{g}_{m-n_o}^{tf}]$. Then,

a) The signal and noise subspaces of $\mathbf{S}^{tf}$ and $\mathbf{G}^{tf}$ are the same as $\mathbf{S}^o$ and $\mathbf{G}^o$, respectively.

b) The eigenvalues have the following relationship:

$$\lambda_i^{tf} = \begin{cases} \dfrac{L}{n_o}(\lambda_i^o - \sigma) + \sigma = \dfrac{L}{n_o}\lambda_i^o + \left(1 - \dfrac{L}{n_o}\right)\sigma & i \leq n_o \\ \sigma^{tf} = \sigma & n_o < i \leq m. \end{cases} \quad (19)$$

An important conclusion from Lemma 2 is that, the largest n_o eigenvalues are amplified using STFD analysis. The amplification of the largest n_o eigenvalues improves detection of the number of the impinging signals on the array, as it widens the separation between dominant and noise-level eigenvalues. Determination of the number of signals is key to establishing the proper signal and noise subspaces, and subsequently plays a fundamental role in subspace-based applications. When the input SNR is low, or the signals are closely spaced, the number of signals may often be underdetermined. When the STFD is applied, the SNR threshold level and/or angle separation necessary for the correct determination of the number of signals are greatly reduced.

Next we consider the signal and noise subspace estimates from a finite number of data samples. We form the STFD matrix based on the true (t, f) points along the IF of the n_o FM signals.

Lemma 3 [14], [10]: If the third-order derivative of the phase of the FM signals is

negligible over the time-period $[t - L + 1, t + L - 1]$, then

a) The estimation errors in the signal vectors are asymptotically (for $N \gg L$) jointly Gaussian distributed with zero means and covariance matrices given by

$$
\begin{aligned}
E &\left(\hat{\mathbf{s}}_i^{tf} - \mathbf{s}_i^{tf} \right) \left(\hat{\mathbf{s}}_j^{tf} - \mathbf{s}_j^{tf} \right)^H \\
&= \frac{\sigma L}{n_o N'} \left[\sum_{\substack{k=1 \\ k \neq i}}^{n_o} \frac{\lambda_i^{tf} + \lambda_k^{tf} - \sigma}{(\lambda_k^{tf} - \lambda_i^{tf})^2} \mathbf{s}_k^{tf} \left(\mathbf{s}_k^{tf} \right)^H + \sum_{k=1}^{m-n_o} \frac{\lambda_i^{tf}}{(\sigma - \lambda_i^{tf})^2} \mathbf{g}_k^{tf} \left(\mathbf{g}_k^{tf} \right)^H \right] \delta_{i,j} \\
&= \frac{\sigma}{N'} \left[\sum_{\substack{k=1 \\ k \neq i}}^{n_o} \frac{(\lambda_i^o - \sigma) + (\lambda_k^o - \sigma) + \frac{n_o}{L}\sigma}{(\lambda_k^o - \lambda_i^o)^2} \mathbf{s}_k^o \left(\mathbf{s}_k^o \right)^H \right. \\
&\qquad \left. + \sum_{k=1}^{m-n_o} \frac{(\lambda_i^o - \sigma) + \frac{n_o}{L}\sigma}{(\sigma - \lambda_i^o)^2} \mathbf{g}_k^o \left(\mathbf{g}_k^o \right)^H \right] \delta_{i,j},
\end{aligned}
\tag{20}
$$

and

$$
\begin{aligned}
E &\left(\hat{\mathbf{s}}_i^{tf} - \mathbf{s}_i^{tf} \right) \left(\hat{\mathbf{s}}_j^{tf} - \mathbf{s}_j^{tf} \right)^T \\
&= -\frac{\sigma L}{n_o N'} \frac{(\lambda_i^{tf} + \lambda_j^{tf} - \sigma)}{(\lambda_j^{tf} - \lambda_i^{tf})^2} \mathbf{s}_j^{tf} \left(\mathbf{s}_i^{tf} \right)^T (1 - \delta_{i,j}) \\
&= -\frac{\sigma}{N'} \cdot \frac{(\lambda_k^o - \sigma) + (\lambda_i^o - \sigma) + \frac{n_o}{L}\sigma}{(\lambda_k^o - \lambda_i^o)^2} \mathbf{s}_j^o (\mathbf{s}_i^o)^T (1 - \delta_{i,j}).
\end{aligned}
\tag{21}
$$

b) The orthogonal projections of $\left\{ \hat{\mathbf{g}}_i^{tf} \right\}$ onto the column space of $\mathbf{S}^{tf}$ are asymptotically (for $N \gg L$) jointly Gaussian distributed with zero means and covariance matrices given by

$$
\begin{aligned}
E &\left(\mathbf{S}^{tf} \left(\mathbf{S}^{tf} \right)^H \hat{\mathbf{g}}_i^{tf} \right) \left(\mathbf{S}^{tf} \left(\mathbf{S}^{tf} \right)^H \hat{\mathbf{g}}_j^{tf} \right)^H \\
&= \frac{\sigma L}{n_o N'} \left[\sum_{k=1}^{n_o} \frac{\lambda_k^{tf}}{(\sigma - \lambda_k^{tf})^2} \mathbf{s}_k^{tf} \left(\mathbf{s}_k^{tf} \right)^H \right] \delta_{i,j} \\
&= \frac{\sigma}{N'} \left[\sum_{k=1}^{n_o} \frac{(\lambda_k^o - \sigma) + \frac{n_o}{L}\sigma}{(\sigma - \lambda_k^o)^2} \mathbf{s}_k^o (\mathbf{s}_k^o)^H \right] \delta_{i,j} \\
&\stackrel{\text{def}}{=} \frac{1}{N'} \mathbf{U}^{tf} \delta_{i,j},
\end{aligned}
\tag{22}
$$

$$
E \left(\mathbf{S}^{tf} \left(\mathbf{S}^{tf} \right)^H \hat{\mathbf{g}}_i^{tf} \right) \left(\mathbf{S}^{tf} \left(\mathbf{S}^{tf} \right)^H \hat{\mathbf{g}}_j^{tf} \right)^T = 0 \quad \text{for all } i,\, j.
\tag{23}
$$

From (20)–(23), two important observations are in order. First, if the signals are both localizable and separable in the t-f domain, then the reduction of the number of signals

from n to n_o greatly reduces the estimation error, specifically when the signals are closely spaced. The second observation relates to SNR enhancements. The above equations show that error reductions using STFDs are more pronounced for the cases of low SNR and/or closely spaced signals. It is clear from (20)–(23) that, when $\lambda_k^o \gg \sigma$ for all $k = 1, 2, ..., n_o$, the results are almost independent of L (suppose $N \gg L$ so that $N' = N - L + 1 \simeq N$), and therefore there would be no obvious improvement in using the STFD over conventional array processing. On the other hand, when some of the eigenvalues are close to σ ($\lambda_k^o \simeq \sigma$, for some $k = 1, 2, ..., n_o$), which is the case of weak or closely spaced signals, all the results of above three equations are reduced by a factor of up to $G = L/n_o$, respectively. This factor represents, in essence, the gain achieved from using STFD processing.

IV. Blind Source Separation

A. Source Separation Based on STFDs

Blind source separation based on STFD was first considered by Belouchrani and Amin [8]. The first step of STFD-based blind source separation is the whitening of the signal part $\mathbf{y}(t)$ of the observation. This is achieved by applying a whitening matrix $\mathbf{W}$ to $\mathbf{y}(t)$, i.e., an $n \times N$ matrix satisfying:

$$\lim_{T \to \infty} \frac{1}{T} \sum_{t=1}^{T} \mathbf{W} \mathbf{y}(t) \mathbf{y}^H(t) \mathbf{W}^H = \mathbf{W} \mathbf{R}_{yy} \mathbf{W}^H = \mathbf{W} \mathbf{A} \mathbf{A}^H \mathbf{A}^H = \mathbf{I}. \tag{1}$$

$\mathbf{W}\mathbf{A}$ is an $n \times n$ unitary matrix $\mathbf{U}$, and matrix $\mathbf{A}$ can be written as

$$\mathbf{A} = \mathbf{W}^{\#} \mathbf{U} \tag{2}$$

where superscript $^{\#}$ denotes pseudo-inverse. The whitened process $\mathbf{z}(t) = \mathbf{W}\mathbf{x}(t)$ still obeys a linear model,

$$\mathbf{z}(t) = \mathbf{W}\mathbf{x}(t) = \mathbf{W}\left[\mathbf{A}\mathbf{s}(t) + \mathbf{n}(t)\right] = \mathbf{U}\mathbf{s}(t) + \mathbf{W}\mathbf{n}(t). \tag{3}$$

By pre- and post-multiplying the STFD matrices $\mathbf{D}_{xx}(t, f)$ by $\mathbf{W}$, we obtain

$$\mathbf{D}_{zz}(t, f) = \mathbf{W}\mathbf{D}_{xx}(t, f)\mathbf{W}^H \tag{4}$$

which is, in essence, the STFD of the whitened data vector $\mathbf{z}(t)$. From the definitions of $\mathbf{W}$ and $\mathbf{U}$,

$$\mathbf{D}_{zz}(t, f) = \mathbf{U}\mathbf{D}_{ss}(t, f)\mathbf{U}^H. \tag{5}$$

60

Equation (5) shows that if $\mathbf{D_{ss}}(t, f)$ is diagonal, which is the case of autoterm points, then any whitened data STFD matrix is diagonal in the basis of the columns of the matrix $\mathbf{U}$, and the eigenvalues of $\mathbf{D_{zz}}(t, f)$ are the diagonal entries of $\mathbf{D_{ss}}(t, f)$. An estimate $\hat{\mathbf{U}}$ of the unitary matrix $\mathbf{U}$ may be obtained as a unitary diagonalizing matrix of a whitening STFD matrix for some t-f points corresponding to the signal autoterm. The source signals can then be estimated as $\hat{\mathbf{s}}(t) = \hat{\mathbf{U}}\hat{\mathbf{W}}\mathbf{x}(t)$, and the mixing matrix $\mathbf{A}$ is estimated by $\hat{\mathbf{A}} = \hat{\mathbf{W}}^{\#}\hat{\mathbf{U}}$.

In order to reduce the noise effect as well as the possibility of having degenerate eigenvalues and subsequently non-unique solutions, the JD and t-f averaging, both discussed in II-C, can be used to incorporate multiple t-f points.

The method discussed above uses STFD matrices to estimate the unitary matrix $\mathbf{U}$, but the covariance matrix is still used for whitening. Therefore, the advantages of STFD matrices are not fully utilized. Using the STFD matrix $\mathbf{D}$, instead of the covariance matrix $\mathbf{R_{xx}}$, to perform whitening is a reasonable alternative [11]. To avoid degenerate eigenvalues, the STFD matrices used for pre-whitening and unitary matrix estimation should be different.

A.1 Example

Fig. 1 shows an example of the application of STFDs to the BSS problem. A three-element equi-spaced linear array is considered where the interelement spacing is half a wavelength. Two chirp signals arrive at $-10°$ and $10°$, respectively. The number of data samples used to compute the STFD is 128. The number of t-f points employed in the JD is p=128, with equal number of points on each signature. Fig. 1(b) shows the Choi-Williams distributions, in which an exponential kernel is applied [16], of two linear mixtures of the original chirp signals depicted in Fig. 1(a), corresponding to the data at the first and the second sensors. Using JD of the STFDs, we are able to recover the original signals from their observed mixture, as shown in Fig. 1(c).

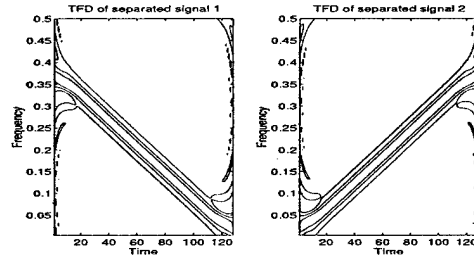### B. Source Separation Based on Spatial Averaging

Source separation based on spatial averaging is proposed by Mu, Amin, and Zhang [17]. This method first performs array averaging of the TFDs of the data across the array,
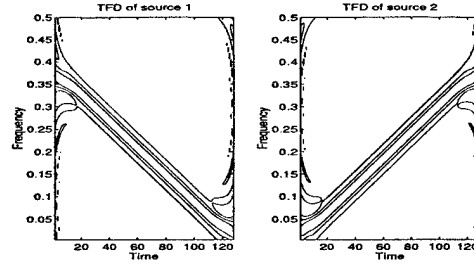
(a) TFDs of the source signals
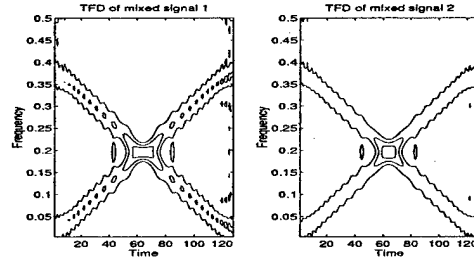
(b) TFDs of the mixed signals

(c) TFDs of the separated signals

Fig. 1. Blind source separation based on STFDs.

permitting the spatial signature of sources to play a fundamental role in improving the synthesis performance.

This method is philosophically different from the one described in the previous section, as it applies the opposite order of operations. It first synthesizes the source signals from the t-f domain, then proceeds to estimate their respective mixing matrix.

The WVD-based synthesis techniques could be found in [18], [19]. Herein, we apply the method of extended discrete-time Wigner distribution (EDTWD), introduced in [19], to the output of array averaged WVD. The advantage of using the EDTWD lies in the fact that it does not require a priori knowledge of the source waveform, and thereby avoids the problem of matching the two "uncoupled" vectors (even-indexed and odd-indexed vectors).

The overall synthesis procedure is summarized in the following steps.

1. Given the received data of the ith sensor $x_i(t)$, compute the EDTWD

$$W_{x_i x_i}(t, f) = \sum_{k:(t+k/2) \in Z} x_i(t + k/2) x_i^*(t - k/2) e^{-j2\pi kf},$$
$$t = 0, \pm 0.5, \pm 1, \ldots \quad (6)$$

2. Apply the averaging process, that is, summing the EDTWD across the array

$$\bar{W}(t, f) = \frac{1}{m} \sum_{k=1}^{m} W_{x_k x_k}(t, f). \quad (7)$$

3. Place an appropriate t-f mask on $\bar{W}(t, f)$ such that only the desired signal autoterms are retained.

4. Take the IFFT of the masked WVD $\bar{W}(t, f)$

$$p(t, \tau) = \sum_f \bar{W}(t, f) e^{j2\pi\tau f}. \quad (8)$$

5. Construct the matrix $\mathbf{Q} = [q_{il}]$ with

$$q_{il} = p\left(\frac{i+l}{2}, i - l\right). \quad (9)$$

6. Apply eigendecomposition to the Hermitian matrix $[\mathbf{Q} + \mathbf{Q}^H]$ and obtain the maximum eigenvalue $\lambda_{\max}$ and the associated eigenvector $\mathbf{u}$. The desired signal is given by

$$\hat{s}_{opt} = e^{j\alpha} \sqrt{2\lambda_{max}} \ \mathbf{u}, \quad (10)$$

where α is an unknown value representing the phase.

7. Repeat step 3 through 6 until all source signals $\hat{d}_1(t), \hat{d}_2(t), \ldots, \hat{d}_L(t)$ are retrieved.

The averaging in step 2 mitigates the crossterms and enforces the autoterms. As such, the source t-f signatures become easier to identify, mask, and synthesize. It is noteworthy that (7) will completely suppress the cross-TFDs for sources with orthogonal spatial signatures.

Upon synthesizing all the source signals, we could utilize these signal waveforms to estimate the mixing, or array, matrix $\mathbf{A}$ through the minimization of the mean square error (MSE),

$$\varepsilon = \sum_{t=1}^{N} \|\mathbf{x}(t) - \mathbf{A}\hat{\mathbf{s}}(t)\|^2. \quad (11)$$

This results in

$$\hat{\mathbf{A}} = \hat{\mathbf{r}}\hat{\mathbf{R}}^{-1}. \tag{12}$$

where $\hat{\mathbf{R}} = \sum_{t=1}^{N} \hat{\mathbf{d}}(t)\hat{\mathbf{d}}^{H}(t)$ represents the estimated signal source covariance matrix, and $\hat{\mathbf{r}} = [\hat{\mathbf{r}}_1, \ldots, \hat{\mathbf{r}}_L]$, with $\hat{\mathbf{r}}_i = \sum_{t=1}^{N} \mathbf{x}(t)\hat{d}_i^*(t)$ being the correlation vector between the data vector received across the array and the ith source signal $\hat{d}_i(t)$.

B.1 Example

We consider three parallel chirp signals. The signals arrive with DOAs of $-20°$, $0°$ and $20°$, with the respective start and end frequencies given by $(0.9\pi, 0.5\pi)$, $(0.66\pi, 0.26\pi)$, and $(0.5\pi, 0.1\pi)$, respectively. The length of the signal sequence is set to $N = 128$. The input SNR is -5 dB. The crossterm of $d_1(t)$ and $d_3(t)$ lies closely to the t-f signature of $d_2(t)$.

We first consider the single antenna case. Fig. 2 depicts both the WVD of the signal arrival and the WVD of the synthesized $\hat{d}_2(t)$. The signal is significantly corrupted by the crossterm of $d_1(t)$ and $d_3(t)$ as well as by the noise components.

Figure 3 depicts, for 16 sensor scenarios, the array averaged WVD and the respective $\hat{d}_2(t)$. Upon averaging, both noise and crossterms are sufficiently reduced to clearly manifest the individual source t-f signatures. The signals could, therefore, be individually recovered by placing appropriate masks in the t-f region. The significance of using array sensors is evident in Fig. 3.
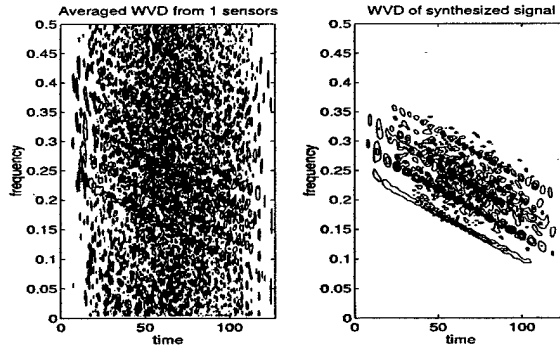

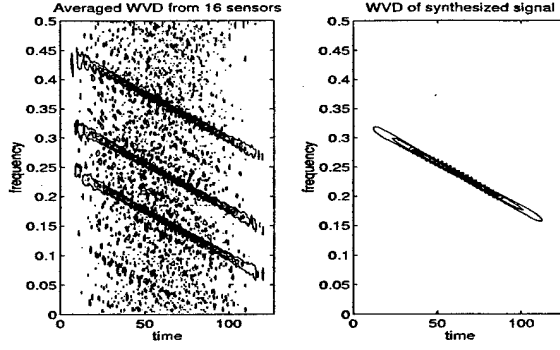Fig. 2. WVD and the synthesized signal ($M = 1$).

Fig. 3. WVD and the synthesized signal ($M = 16$).

C. Effect of Crossterms between Source Signals

In this section, we examine the effect of the t-f crossterms on source separation performance [20]. To simplify the problem, we assume that $\mathbf{R_{dd}}$ is an identity matrix. When crossterms are present at the off-diagonal elements of the TFD matrix $\mathbf{D_{dd}}(t, f)$, then

$$\mathbf{D_{dd}}(t, f) = \mathbf{P}(t, f)\mathbf{G}(t, f)\mathbf{P}^H(t, f) \tag{13}$$

where $\mathbf{G}(t, f)$ is the diagonal matrix with the eigenvalues at the diagonal elements, and $\mathbf{P}(t, f)$ is the matrix whose columns are the corresponding eigenvectors. Note that all the above matrices depend on the selected (t, f) point. From (13), the STFD matrix of the data vector under noise-free conditions becomes

$$\mathbf{D_{xx}}(t, f) = \mathbf{A}\mathbf{D_{ss}}(t, f)\mathbf{A}^H = \mathbf{A}\mathbf{P}(t, f)\mathbf{G}(t, f)\mathbf{P}^H(t, f)\mathbf{A}^H \tag{14}$$

and the STFD matrix of the whitened array signal vector is

$$\mathbf{D_{zz}}(t, f) = \mathbf{W}\mathbf{A}\mathbf{P}(t, f)\mathbf{G}(t, f)\mathbf{P}^H(t, f)\mathbf{A}^H\mathbf{W}^H. \tag{15}$$

Since $\mathbf{G}(t, f)$ is diagonal, $\mathbf{W}\mathbf{A}\mathbf{P}(t, f)$ is unitary. Therefore, the source separation method will assume $\mathbf{W}\mathbf{A}\mathbf{P}(t, f)$ as the unitary matrix and estimates the mixing matrix as

$$\hat{\mathbf{A}} = \mathbf{W}^{\#}\mathbf{W}\mathbf{A}\mathbf{P}(t, f) = \mathbf{A}\mathbf{P}(t, f) \tag{16}$$

which is dependent on the unitary matrix $\mathbf{P}(t, f)$. Furthermore,

$$\hat{\mathbf{A}}^{\#}\mathbf{A} = [\mathbf{A}\mathbf{P}(t, f)]^{\#}\mathbf{A} = \mathbf{P}^H(t, f). \tag{17}$$

65

Matrix $\hat{\mathbf{A}}$ should be close to the true one $\mathbf{A}$ so that $\hat{\mathbf{A}}^{\#}\mathbf{A}$ well approximates the identity matrix. The following variable measures, at separations, the ratio of the power of interference of the qth source signal to the power of the pth source signal [8]

$$I_{pq} = E \left| \left(\hat{\mathbf{A}}^{\#}\mathbf{A} \right)_{pq} \right|^{2}, \tag{18}$$

where $\left(\hat{\mathbf{A}}^{\#}\mathbf{A} \right)_{pq}$ denotes the (p,q)th element of matrix $\hat{\mathbf{A}}^{\#}\mathbf{A}$. The following global rejection level is used to evaluate the overall performance of a blind source separation system

$$I_{perf} = \sum_{q \neq p} I_{pq}. \tag{19}$$

For the mixing matrix estimation given in (17), the global rejection level is approximated by the following normalized global rejection level [20]

$$I'_{perf} = \left[diagonal \left(\hat{\mathbf{A}}^{\#}\mathbf{A} \right) \right] \hat{\mathbf{A}}^{\#}\mathbf{A} = \sum_{q=1}^{n} |p_{qq}(t,f)|^{-2} - n. \tag{20}$$

where $diagonal(\mathbf{F})$ denotes the matrix formed by the diagonal elements of $\mathbf{F}$. In general, since the absolute values of $p_{qq}(t,f)$ are always equal to or smaller than 1, the global rejection level I_{perf} takes a positive value. It is clear that $I_{perf} = 0$ only when $p_{qq}(t,f) = 1$ holds true for all q. That is, $\mathbf{P}$ is an identity matrix, which implies that there is no off-diagonal non-zero elements in matrix $\mathbf{D_{dd}}(t,f)$, i.e., no crossterms.

D. Source Separation Based on Joint Diagonalization and Joint Anti-Diagonalization

From the previous subsection, it is clear that care must be exercised when dealing with crossterms. The method, proposed by Belouchrani, Abed-Meraim, Amin, and Zoubir [21], carefully and properly exploits both autoterms and crossterms of the TFDs for improved source separation. This approach is based on the simultaneous diagonalization and anti-diagonalization of a combined set of autoterm and crossterm TFD matrices, respectively.

The auto-STFD and cross-STFD are defined as

$$\mathbf{D_{ss}^{a}}(t,f) = \mathbf{D_{ss}}(t,f) \quad \text{for autoterm t-f points} \tag{21}$$

and

$$\mathbf{D_{ss}^{c}}(t,f) = \mathbf{D_{ss}}(t,f) \quad \text{for crossterm t-f points.} \tag{22}$$

66

Since the off-diagonal elements of $\mathbf{D}_{\mathrm{ss}}(t,f)$ are crossterms, the auto-STFD matrix is quasi diagonal for each t-f point that corresponds to a true power concentration, i.e. signal autoterm. Similarly, since the diagonal elements of $\mathbf{D}_{\mathrm{ss}}(t,f)$ are auto-terms, the cross-STFD matrix is quasi anti-diagonal (i.e. its diagonal entries are close to zero) for each t-f point that corresponds to a crossterm.

As discussed earlier, JD can be used to incorporate multiple autoterm t-f points. Similarly, the joint anti-diagonalization (JAD) is appropriate to incorporate multiple crossterm t-f points. By selecting crossterm t-f points, the data cross-STFD will have the following structure,

$$\mathbf{D}_{\mathrm{xx}}^{c}(t,f) = \mathbf{U}\mathbf{D}_{\mathrm{ss}}^{c}(t,f)\mathbf{U}^{H} \tag{23}$$

where $\mathbf{D}_{\mathrm{ss}}^{c}(t,f)$ is anti-diagonal. The JAD searches for the unitary matrix that anti-diagonalizes a combined set $\{\mathbf{D}_{\mathrm{xx}}^{c}(t_i,f_i)|i=1,\cdots,q\}$ of q STFD matrices. The procedure for anti-diagonalization of a single $m \times m$ matrix $\mathbf{N}$ is explained in [21] and is equivalent to the maximization of the criterion

$$C(\mathbf{N},\mathbf{V}) \overset{\mathrm{def}}{=} -\sum_{i=1}^{m}\left|\mathbf{v}_i^{H}\mathbf{N}\mathbf{v}_i\right|^2 \tag{24}$$

over the set of unitary matrices $\mathbf{V} = [\mathbf{v}_1,\cdots,\mathbf{v}_m]$.

The combined JD and JAD of two sets $\{\mathbf{M}_k|k=1..p\}$ and $\{\mathbf{N}_k|k=1..q\}$ of $m \times m$ matrices is defined as the maximization of the JD/JAD criterion:

$$C(\mathbf{V}) \overset{\mathrm{def}}{=} \sum_{i=1}^{m}\left(\sum_{k=1}^{p}\left|\mathbf{v}_i^{H}\mathbf{M}_k\mathbf{v}_i\right|^2 - \sum_{k=1}^{q}\left|\mathbf{v}_i^{H}\mathbf{N}_k\mathbf{v}_i\right|^2\right) \tag{25}$$

over the set of unitary matrices $\mathbf{V} = [\mathbf{v}_1,\cdots,\mathbf{v}_m]$.

D.1 Selection of Autoterm and Crossterm Points

The success of the JD or JAD of STFD matrices in determining the unitary matrix $\mathbf{U}$ depends strongly on the correct selection of the autoterm and crossterm points. Therefore, it is crucial to have a selection procedure that is able to distinguish between autoterm and crossterm points based only on the STFD matrices of the observation. A selection approach was proposed in [21] to exploit the anti-diagonal structure of the crossterm STFD matrices. More precisely,

$$\mathrm{Trace}(\mathbf{D}_{\mathrm{xx}}^{c}(t,f)) = \mathrm{Trace}(\mathbf{U}\mathbf{D}_{\mathrm{ss}}^{c}(t,f)\mathbf{U}^{H}) = \mathrm{Trace}(\mathbf{D}_{\mathrm{ss}}^{c}(t,f)) \approx 0.$$

Based on this observation, the following testing procedure can be defined:

$$\text{if } \frac{\text{Trace}(\mathbf{D_{xx}}(t,f))}{\text{norm}(\mathbf{D_{xx}}(t,f))} < \epsilon \longrightarrow \text{ decide that } (t,f) \text{ is a crossterm}$$

$$\text{if } \frac{\text{Trace}(\mathbf{D_{xx}}(t,f))}{\text{norm}(\mathbf{D_{xx}}(t,f))} > \epsilon \longrightarrow \text{ decide that } (t,f) \text{ is an autoterm}$$

where ϵ is a 'small' positive real scalar.

D.2 Example

We consider a uniform linear array of $m = 3$ sensors having half wavelength spacing and receiving signals from $n = 2$ sources in the presence of white Gaussian noise. The sources arrive from different directions $\theta_1 = 10$ and $\theta_2 = 20$ degrees. The emitted signals are two chirps. The WVD is computed over 1024 samples and eight STFD matrices are considered.

We compare in Fig. 4 the performance of the JD-based algorithm, introduced in IV-A, and the JD/JAD algorithm, for SNRs in the range [5 – 20 dB]. The mean rejection levels are evaluated over 100 Monte Carlo runs. In this case, the new algorithm performs slightly better than the JD-based algorithm.
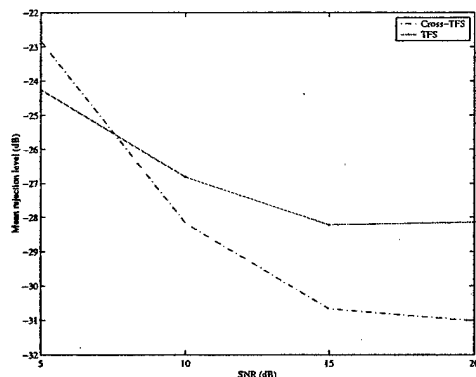

Fig. 4. Mean rejection level versus input SNR for JD and JD/AJD based source separation methods.

V. Direction Finding

A. Time-Frequency MUSIC

The t-f MUSIC was proposed by Belouchrani and Amin [9], and its performance is analyzed by Zhang, Mu, and Amin [14]. Without loss of generality, we consider one-

dimensional direction finding where the DOAs are described by θ. First, recall that the DOAs are estimated in the MUSIC technique by determining the n values of θ for which the following spatial spectrum is maximized [22],

$$f_{MU}(\theta) = \left[\mathbf{a}^H(\theta)\hat{\mathbf{G}}\hat{\mathbf{G}}^H\mathbf{a}(\theta)\right]^{-1} = \left[\mathbf{a}^H(\theta)\left(\mathbf{I} - \hat{\mathbf{S}}\hat{\mathbf{S}}^H\right)\mathbf{a}(\theta)\right]^{-1}, \tag{1}$$

where $\mathbf{a}(\theta)$ is the steering vector corresponds to θ. The variance of those estimates in the MUSIC technique, assuming white noise processes, is given by [15]

$$E\left(\hat{\omega}_i - \omega_i\right)^2 = \frac{1}{2N}\frac{\mathbf{a}^H(\theta_i)\mathbf{U}\mathbf{a}(\theta_i)}{h(\theta_i)} \tag{2}$$

where $\omega_i = (2\pi d/\lambda)\sin\theta_i$ is the spatial frequency associated with DOA θ_i, and $\hat{\omega}_i$ is its estimate obtained from the MUSIC. Moreover, $\mathbf{U}$ is defined in (11), and

$$h(\theta_i) = \mathbf{d}^H(\theta_i)\mathbf{G}\mathbf{G}^H\mathbf{d}(\theta_i), \quad \text{with} \quad \mathbf{d}(\theta_i) = d\mathbf{a}(\theta_i)/d\omega. \tag{3}$$

Similarly, for t-f MUSIC with n_o signals selected, the DOAs are determined by locating the n_o peaks of the spatial spectrum defined from the n_o signals' t-f regions,

$$f_{MU}^{tf}(\theta) = \left[\mathbf{a}^H(\theta)\hat{\mathbf{G}}^{tf}\left(\hat{\mathbf{G}}^{tf}\right)^H\mathbf{a}(\theta)\right]^{-1} = \left[\mathbf{a}^H(\theta)\left(\mathbf{I} - \hat{\mathbf{S}}^{tf}\left(\hat{\mathbf{S}}^{tf}\right)^H\right)\mathbf{a}(\theta)\right]^{-1}. \tag{4}$$

$\hat{\mathbf{G}}^{tf}$ and $\hat{\mathbf{S}}^{tf}$ can be obtained by using either JBD or t-f averaging (section II-C). When the t-f averaging is used, using the results of Lemmas 2 and 3, the variance of the DOA estimates based on t-f MUSIC is obtained as [14],

$$E\left(\hat{\omega}_i^{tf} - \omega_i\right)^2 = \frac{1}{2N'}\frac{\mathbf{a}^H(\theta_i)\mathbf{U}^{tf}\mathbf{a}(\theta_i)}{h^{tf}(\theta_i)} \tag{5}$$

where $\hat{\omega}_i^{tf}$ is the estimate of ω_i, $\mathbf{U}^{tf}$ is defined in (22), and

$$h^{tf}(\theta_i) = \mathbf{d}^H(\theta_i)\mathbf{G}^{tf}\left(\mathbf{G}^{tf}\right)^H\mathbf{d}(\theta_i). \tag{6}$$

Note that $h^{tf}(\theta) = h(\theta_i)$ if $n_o = n$.

A.1 Examples

Consider a uniform linear array of 8 sensors spaced by half a wavelength, and an observation period of 1024 samples. Two chirp signals emitted from two sources positioned at

angle θ_1 and θ_2. The start and end frequencies of the signal source at θ_1 are $\omega_{s1} = 0$ and $\omega_{e1} = \pi$, while the corresponding two frequencies for the other source at θ_2 are $\omega_{s2} = \pi$ and $\omega_{e2} = 0$, respectively.

Fig. 5 displays the variance of the estimated DOA $\hat{\theta}_1$ versus SNR for the case $(\theta_1, \theta_2) = (-10°, 10°)$. The curves in this figure show the theoretical and experimental results of the conventional MUSIC and t-f MUSIC (for L=33 and 129). The Cramer-Rao bound (CRB) is also shown in Fig. 5 for comparison. Both signals were selected when performing t-f MUSIC ($n_o = n = 2$). Simulation results were averaged over 100 independent Monte-Carlo runs. The advantages of t-f MUSIC in low SNR cases are evident from this figure. The experiment results deviate from the theoretical results for low SNR, since we only considered the lowest order of the coefficients of the perturbation expansion in deriving the theoretical results [14]. Fig. 6 shows estimated spatial spectra at SNR=−20 dB based on t-f MUSIC ($L = 129$) and the conventional MUSIC. The t-f MUSIC spectral peaks are clearly resolved.

Fig. 7 shows examples of the estimated spatial spectrum based on t-f MUSIC ($L = 129$) and the conventional MUSIC where the angle separation is small ($\theta_1 = -2.5°$, $\theta_2 = 2.5°$). The input SNR is −5 dB. Two t-f MUSIC algorithms are performed using two sets of t-f points, each set belongs to the t-f signature of one source ($n_o = 1$). It is evident that the two signals cannot be resolved when the conventional MUSIC is applied, whereas by utilizing the signals' distinct t-f signatures and applying t-f MUSIC separately for each signal, the two signals become clearly separated and reasonable DOA estimation is achieved. It is noted that there is a small bias in the estimates of t-f MUSIC due to the imperfect separation of the two signals in the t-f domain.

B. Time-Frequency Maximum Likelihood Method

In this section, we introduce the time-frequency maximum likelihood (t-f ML) methods. This method was proposed by Zhang, Mu, and Amin [10] to deal with coherent nonstationary sources. For conventional ML methods, the joint density function of the sampled
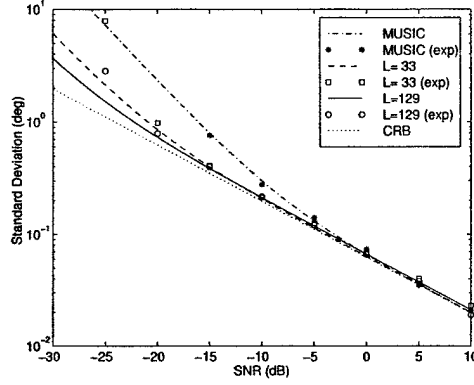
Fig. 5. Variance of DOA estimation versus input SNR.
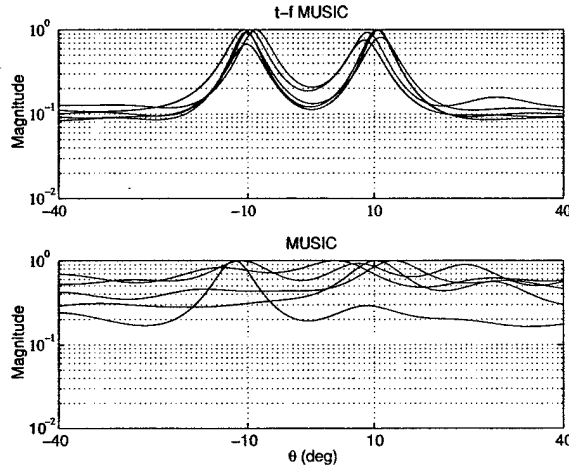
Fig. 6. Estimated spatial spectra of MUSIC and t-f MUSIC.

data vectors $\mathbf{x}(1), \mathbf{x}(2), ..., \mathbf{x}(N)$, is given by [23]

$$
\begin{aligned}
f(\mathbf{x}(1), &\ldots, \mathbf{x}(N)) \\
&= \prod_{i=1}^{N} \frac{1}{\pi^m \det[\sigma \mathbf{I}]} \exp\left(-\frac{1}{\sigma}[\mathbf{x}(i) - \mathbf{A}\mathbf{d}(i)]^H [\mathbf{x}(i) - \mathbf{A}\mathbf{d}(i)]\right),
\end{aligned}
\tag{7}
$$

where $\det[\cdot]$ denotes the matrix determinant. It follows from (7) that the log-likelihood function of the observations $\mathbf{x}(1), \mathbf{x}(2), \ldots, \mathbf{x}(N)$, is given by

$$
L = -mN\ln\sigma - \frac{1}{\sigma} \sum_{i=1}^{N} [\mathbf{x}(i) - \mathbf{A}\mathbf{d}(i)]^H [\mathbf{x}(i) - \mathbf{A}\mathbf{d}(i)].
\tag{8}
$$

To carry out this minimization, we fix $\mathbf{A}$ and minimize (8) with respect to $\mathbf{d}$. This yields the well-known solution

$$
\hat{\mathbf{d}}(i) = \left[\mathbf{A}^H \mathbf{A}\right]^{-1} \mathbf{A}^H \mathbf{x}(i).
\tag{9}
$$

71

Fig. 7. Estimated spatial spectra of MUSIC and t-f MUSIC for closely spaced signals.

We can obtain the concentrated likelihood function as [23]

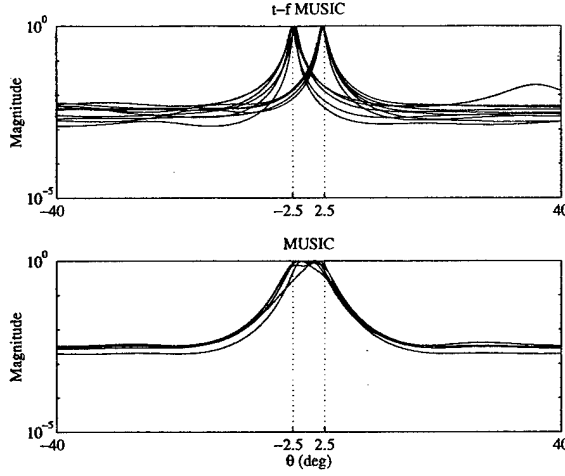$$F_{ML}(\Theta) = tr \left\{ \left[\mathbf{I} - \hat{\mathbf{A}}(\hat{\mathbf{A}}^H \hat{\mathbf{A}})^{-1} \hat{\mathbf{A}}^H \right] \hat{\mathbf{R}}_{\mathbf{xx}} \right\}, \tag{10}$$

where $tr(\mathbf{A})$ denotes the trace of $\mathbf{A}$. The ML estimate of Θ is obtained as the minimizer of (10). Let ω_i and $\hat{\omega}_i$, respectively, denote the spatial frequency and its ML estimate associated with θ_i, then the estimation error $(\hat{\omega}_i - \omega_i)$ are asymptotically (for large N) jointly Gaussian distributed with zero means and the covariance matrix [24]

$$
\begin{aligned}
E\left[(\hat{\omega}_i - \omega_i)^2\right] = \frac{1}{2N} \left[\mathrm{Re}(\mathbf{H} \odot \mathbf{R}_{\mathbf{dd}}^T)\right]^{-1} \\
\times \mathrm{Re}\left[\mathbf{H} \odot (\mathbf{R}_{\mathbf{dd}} \mathbf{A}^H \mathbf{U} \mathbf{A} \mathbf{R}_{\mathbf{dd}})^T\right] \left[\mathrm{Re}(\mathbf{H} \odot \mathbf{R}_{\mathbf{dd}}^T)\right]^{-1}
\end{aligned}
\tag{11}
$$

where $\odot$ denotes Hadamard product, $\mathbf{U}$ is defined in (11). Moreover,

$$\mathbf{H} = \mathbf{C}^H \left[\mathbf{I} - \mathbf{A}(\mathbf{A}^H \mathbf{A})^{-1} \mathbf{A}^H \right] \mathbf{C}, \quad \text{with} \quad \mathbf{C} = d\mathbf{A}/d\omega. \tag{12}$$

Next we consider the t-f ML method. As we discussed in the previous section, we select $n_o \leq n$ signals in the t-f domain. The concentrated likelihood function defined from the STFD matrix is similar to (10) and is obtained by replacing $\hat{\mathbf{R}}_{\mathbf{xx}}$ by $\hat{\mathbf{D}}$,

$$F_{ML}^{tf}(\Theta) = tr \left[\mathbf{I} - \hat{\mathbf{A}}^o \left((\hat{\mathbf{A}}^o)^H \hat{\mathbf{A}}^o \right)^{-1} (\hat{\mathbf{A}}^o)^H \right] \hat{\mathbf{D}}. \tag{13}$$

Therefore, the estimation error $(\hat{\omega}_i^{tf} - \omega_i)$ associated with the t-f ML method are asymptotically (for $N \gg L$) jointly Gaussian distributed with zero means and the covariance

72

matrix [10]

$$E\left[\left(\hat{\omega}_i^{tf} - \omega_i\right)^2\right] = \frac{\sigma}{2N'} \left[\mathrm{Re}(\mathbf{H}^o \odot \mathbf{D}_{\mathbf{dd}}^T)\right]^{-1}$$

$$\times \mathrm{Re}\left[\mathbf{H}^o \odot \left(\mathbf{D}_{\mathbf{dd}}(\mathbf{A}^o)^H \mathbf{U}^{tf} \mathbf{A}^o \mathbf{D}_{\mathbf{dd}}\right)^T\right] \left[\mathrm{Re}(\mathbf{H}^o \odot \mathbf{D}_{\mathbf{dd}}^T)\right]^{-1}$$

$$= \frac{\sigma}{2N'} \left[\mathrm{Re}\left(\mathbf{H}^o \odot (\mathbf{R}_{\mathbf{dd}}^o)^T\right)\right]^{-1} \tag{14}$$

$$\times \mathrm{Re}\left[\mathbf{H}^o \odot \left(\mathbf{R}_{\mathbf{dd}}^o(\mathbf{A}^o)^H \mathbf{U}^{tf} \mathbf{A}^o \mathbf{R}_{\mathbf{dd}}^o\right)^T\right] \left[\mathrm{Re}\left((\mathbf{H}^o \odot \mathbf{R}_{\mathbf{dd}}^o)^T\right)\right]^{-1},$$

where $\mathbf{U}^{tf}$ is defined in (22), and

$$\mathbf{H}^o = (\mathbf{C}^o)^H \left[\mathbf{I} - \mathbf{A}^o\left((\mathbf{A}^o)^H \mathbf{A}^o\right)^{-1}(\mathbf{A}^o)^H\right] \mathbf{C}^o, \quad \text{with} \quad \mathbf{C}^o = d\mathbf{A}^o/d\omega. \tag{15}$$

In the case of $n_o = n$, then $\mathbf{H}^o = \mathbf{H}$, and $\mathbf{C}^o = \mathbf{C}$.

The signal localization in the t-f domain enables us to select fewer signal arrivals. This fact is not only important in improving the estimation performance, particularly when the signals are closely spaced, but also reduces the dimension of the optimization problem solved by the maximum likelihood algorithm, and subsequently reduces the computational requirement.

B.1 Examples

To demonstrate the advantages of t-f ML over both the conventional ML and the t-f MUSIC, consider a uniform linear array of 8 sensors separated by half a wavelength. Two FM signals arrive from $(\theta_1, \theta_2) = (-10°, 10°)$ with the IFs $f_1(t) = 0.2 + 0.1t/N + 0.2\sin(2\pi t/N)$ and $f_2(t) = 0.2 + 0.1t/N + 0.2\sin(2\pi t/N + \pi/2), t = 1, ..., N$. The SNR of both signals is -20 dB, and the number of snapshots used in the simulation is $N = 1024$. We used $L=129$ for t-f ML. Fig. 8 shows (θ_1, θ_2) that yield the minimum values of the likelihood function of the t-f ML and the ML methods for 20 independent trials. It is evident that the t-f ML provides much improved DOA estimation over the conventional ML.

In the next example, the t-f ML and the t-f MUSIC are compared for coherent sources. The two coherent FM signals have common IFs $f_{1,2}(t) = 0.2 + 0.1t/N + 0.2\sin(2\pi t/N), t = 1, ..., N$, with $\pi/2$ phase difference. The signals arrive at $(\theta_1, \theta_2) = (-2°, 2°)$. The SNR of both signals is 5 dB and the number of snapshots is 1024. Fig. 9 shows the contour plots of the likelihood function of the t-f ML and the estimated spectra of t-f MUSIC for three

independent trials. It is clear that the t-f ML can separate the two signals whereas the t-f MUSIC cannot.
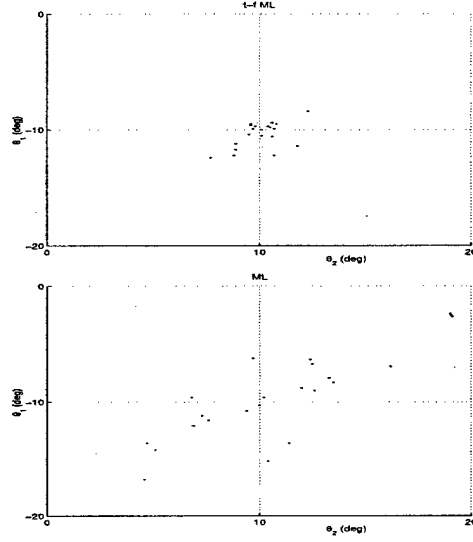
Fig. 8. (θ_1, θ_2) which minimize the t-f ML (upper) and ML (lower) likelihood functions.

C. Effect of Crossterms

Identifying the sources' t-f signatures often require searching the t-f domain for peak values. In some cases, these values correspond to crossterms. Building the STFDs around only crossterms or a mixture of autoterm and crossterms and its effect on the t-f MUSIC performance is considered by Amin and Zhang [25]. To understand the tole of crossterms in direction finding, it is important to compare the crossterms to the cross-correlation between signals in conventional array processing, whose properties are familiar. The source TFD matrix takes the following general form,

$$\mathbf{D_{dd}}(t,f) = \begin{bmatrix} D_{d_1 d_1}(t,f) & D_{d_1 d_2}(t,f) & \cdots & D_{d_1 d_n}(t,f) \\ D_{d_2 d_1}(t,f) & D_{d_2 d_2}(t,f) & \cdots & D_{d_2 d_n}(t,f) \\ \vdots & \vdots & \ddots & \vdots \\ D_{d_n d_1}(t,f) & D_{d_n d_2}(t,f) & \cdots & D_{d_n d_n}(t,f) \end{bmatrix} \tag{16}$$

On the other hand, the covariance matrix of correlated source signals is given at the

74

Fig. 9. Contour plots of t-f ML likelihood function (upper) and spatial spectra of t-f MUSIC (lower).
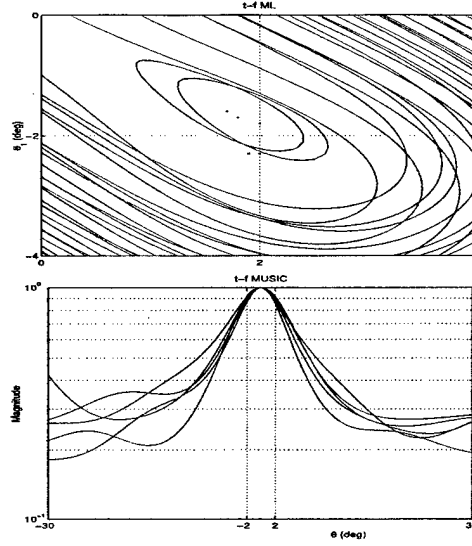
form

$$
\mathbf{R_{dd}} = \begin{bmatrix} R_{d_1 d_1} & R_{d_1 d_2} & \cdots & R_{d_1 d_n} \\ R_{d_2 d_1} & R_{d_2 d_2} & \cdots & R_{d_2 d_n} \\ \vdots & \vdots & \ddots & \vdots \\ R_{d_n d_1} & R_{d_n d_2} & \cdots & R_{d_n d_n} \end{bmatrix} \tag{17}
$$

where the off-diagonal element $R_{d_i d_j} = E[d_i(t)d_j^*(t)]$ represents the correlation between source signals d_i and d_j. Direction finding problems can usually be solved when the signals are partially correlated, however, full rank property of the source covariance matrix $\mathbf{R_{dd}}$ is a necessary condition.

Comparing equations (16) and (17), it is clear that the cross-correlation terms and the crossterms have analogous forms. However, the correlation matrix in (17) is defined for stationary signal environments, whereas the source TFD matrix in (16) is defined at a (t, f) point and its value usually varies with respect to t and f. Detailed observations are made through the following example.

C.1 Example

Consider a six-element linear array with half-wavelength inter-element spacing, and two chirp signal arrival. The start and end frequencies of the first signal $d_1(t)$ are $f_{1s} = 0.1$ and $f_{1e} = 0.5$, and those for the second signal $d_2(t)$ are $f_{2s} = 0$ and $f_{2e} = 0.4$, respectively.

75

The SNR is 10 dB for each signal, and the DOAs of the two signals are $\theta_1 = -5°$ and $\theta_2 = 5°$, respectively. The number of samples is 256. PWVD is used and the window length is $N = 129$.

We consider the autorerms and the crossterms over the following two regions: i) autoterm regions (t, f_1) with $f_1(t) = 0.1 + 0.4t/N$ and (t, f_2) with $f_2(t) = 0.4t/N$, where the autoterms are dominant; and ii) crossterm region (t, f_c) with $f_c(t) = [f_1(t) + f_2(t)]/2 = 0.05 + 0.4t/N$, where the crossterms are dominant. Both the autoterm and crossterm regions have large peak values and are most likely to be selected.

i) *Autoterm regions.* In the autoterm region of $d_1(t)$, (t, f_1), the autoterm of $d_1(t)$ is constant. The autoterm of $d_2(t)$ and the crossterm between $d_1(t)$ and $d_2(t)$ are relatively small. Since the STFD matrix in the autoterm region has dominant diagonal elements with constant values, incorporating only autoterm points, either by JBD or by t-f averaging, usually provides good direction finding performance.

ii) *Crossterm regions.* In this region the crossterms $D_{d_1d_2}(t, f) = D^*_{d_2d_1}(t, f)$ are dominant. Therefore, the source TFD matrix on the crossterm region is nearly anti-diagonal. Note that this source TFD matrix is still full rank (although not necessarily positive definite). Accordingly, the noise subspace can be properly estimated, even when only the crossterm points are selected. However, since the crossterms change with time t, taking both positive and negative values, summing them at different (t, f) points yields small smoothed values. Therefore, the t-f averaging is expected to yield degraded performance in some cases. Performing JBD instead of t-f averaging avoids such risk.

Table I shows the DOA variance of signal $d_1(t)$ obtained from 100 independent Monte-Carlo runs of t-f MUSIC. Both JBD and t-f averaging are considered for four cases, namely, (a) autoterm regions $f(t) = f_1(t)$ and $f(t) = f_2(t)$, (b) crossterm region $f(t) = [f_1(t) + f_2(t)]/2$, (c) autoterm and crossterm regions $f(t) = f_1(t)$, $f(t) = f_2(t)$, and $f(t) = [f_1(t) + f_2(t)]/2$, and (d) autoterm region of the first signal, $f(t) = f_1(t)$. Although both the JBD and t-f averaging resolve the signals in all the four cases, it is evident that the JBD outperforms the t-f averaging, particularly when the crossterm region is involved. Case (d) in which only one of the two signals is selected has the best performance for both methods of JBD and t-f averaging. An interesting observation is that, in case (b), where

76

only the crossterm region is used, the JBD yields second best performance, whereas the t-f averaging shows its worst performance.

TABLE I

VARIANCES OF DOA ESTIMATES

	case (a)	case (b)	case (c)	case (d)
JBD	0.156°	0.154°	0.180°	0.121°
T-f averaging	0.179°	0.339°	0.199°	0.161°

VI. Spatial Ambiguity Functions

The spatial ambiguity function is proposed by Amin, Belouchrani, and Zhang [26]. The discrete form spatial ambiguity function (SAF) matrix of a signal vector $\mathbf{x}(t)$ is defined as

$$\mathbf{D_{xx}}(\theta, \tau) = \sum_{u=-\infty}^{\infty} \mathbf{x}(u + \tau/2)\mathbf{x}^H(u - \tau/2)e^{j\theta u} \qquad (1)$$

where θ and τ are the frequency-lag and the time-lag, respectively. In noise-free environment, $\mathbf{x}(t) = \mathbf{A}\mathbf{d}(t)$. In this case,

$$\mathbf{D_{xx}}(\theta, \tau) = \mathbf{A}\mathbf{D_{dd}}(\theta, \tau)\mathbf{A}^H. \qquad (2)$$

Equation (2) is similar to the formula that has been commonly used in blind source separation and DOA estimation problems, relating the data correlation matrix to the signal correlation matrix. Here, these matrices are replaced by the data SAF and signal ambiguity function matrices, respectively. The two subspaces spanned by the principle eigenvectors of $\mathbf{D_{xx}}(\theta, \tau)$ and the columns of $\mathbf{A}$ are identical. This implies that array signal processing problems can be approached and solved based on the SAF.

By replacing the STFD matrix $\mathbf{D_{xx}}(t, f)$ by the SAF matrix $\mathbf{D_{xx}}(\theta, \tau)$, we can easily derive the ambiguity-domain source separation methods and the ambiguity-domain MUSIC (AD MUSIC) [26], following the same procedures described in IV and V.

The SAFs have the following two important offerings that distinguish them from other array spatial functions.

1) The crossterms in between source signals reside on the off-diagonal entries of matrix $\mathbf{D_{dd}}(\theta, \tau)$, violating its diagonal structure, which is necessary to perform blind source

separation. In the ambiguity domain, the signal autoterms are positioned near and at the origin, making it easier to leave out crossterms from matrix construction.

2) The autoterms of all narrowband signals, regardless of their frequencies and phases, fall on the time-lag axis ($\theta = 0$), while those of the wideband signals fall on a different (θ, τ) region or spread over the entire ambiguity domain. Therefore, the SAF is a natural choice for recovering and spatially localizing narrowband sources in broadband signal platforms.

VII. Sensor-Angle Distributions

In this section we use quadratic distributions to address the problem of characterizing the power attributed to near-field scattering local to an array of sensors. The proposed method is based on the quadratic sensor-angle distribution (SAD), previously called the spatial Wigner distribution [27]. This distribution is a characterization of the power at every angle for each sensor in the array. It is altogether different than the STFDs discussed in the previous sections. These two types of distributions have different structures and objectives.

In the SAD, near-field sources have different angles for the various array sensors. The SAD is a joint-variable distribution and a dual in sensor number and angle to Cohen's class of TFDs [1]. We use a known test source to illuminate the local scatterer distribution we wish to characterize. Orthogonal subspace projection techniques are then applied to the array data to suppress the direct propagation path from the test source so as to reveal the less powerful local scatter. An example from the area of high-frequency surface wave radar is provided for illustration.

A typical surface-wave radar receiving array may consist of between 8 and 64 sensors and can be hundreds of meters or indeed more than 1km in total length. It is typically sited on a coastal beach which may or may not provide a uniform transition from land to sea. The coast may in fact be a bay in which case the land sea boundaries beyond either end of the array may cause near-field scattering and distort the wave-front arriving at the array. There may be other locally sited structures, such as buildings and fences, which can be the source of local scatter (consider that the wavelength of the radar signal is between 30–100m). This makes achieving very low sidelobe spatial beams with a classical beamformer a difficult problem and can render the receiver system vulnerable to interference through

beam sidelobes (possibly via skywave propagation).

The near-field scatter produced by these mechanisms are correlated with the desired direct far-field radar return from targets (and clutter). This scatter is typically approximately 20–40dB weaker than the direct signal. Without compensating for the effects of local scatter, it is possible to achieve classical beam sidelobes of 30–35dB, however in general the remaining components of the receiving system can sustain substantially higher performance [28].

The effect of local scatter on beamforming must be mitigated in order for the radar system to realize the inherent sidelobe capability as set by the radar equipment (as distinct from the sensors) [28]. A first step to achieving this is to characterize the local scatter distribution. A means of performing this characterization using techniques derived from time-frequency analysis is the focus of the remaining sections of this chapter.

A generalization of the spatial Wigner distribution introduced in [27] is provided and combined with orthogonal projection techniques for detection, classification, and characterization of near-field and far-field sources lying in the field of view of the multi-antenna receiver.

A. Signal Model

A.1 Geometry

Consider a linear equi-spaced array of M sensors placed on a flat plane in a two dimensional surface. Assume that sensor position errors are negligible and the gain and phase of all sensors and corresponding data acquisition equipment are accurately matched. It is also assumed that the array is narrowband, i.e., the reciprocal of the bandwidth of any signals received is large compared with the propagation delay across the array. The wavelength of all sources received is λ. Let the origin of a coordinate system be at the mid-point of the array, with the sensors individually spaced by d regularly along the x-axis and indexed $i = 1, \ldots, M$ from left to right. We assume that $d < \frac{\lambda}{2}$. Boresight is along the y-axis.

A source is placed in the near-field (i.e. a circular wavefront impinges on the array) at location r_s meters from the origin and θ_s degrees from boresight. For convenience

(although somewhat unconventionally) we have defined that angles are to be measured clockwise from array boresight (the y-axis). For M odd there is a sensor at the origin, whereas for M even the origin is midpoint between two sensors. The array geometry and the notations are shown in Fig. 10 for the case of M even.
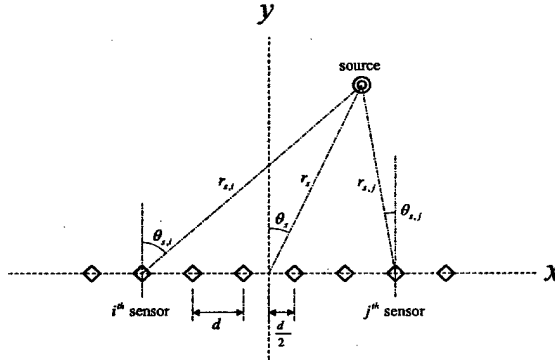

Fig. 10. Sensor array geometry and notations for linear array and a near-field source

The distance from the ith sensor to the source is given by

$$r_{s,i}^2 = r_s^2 + \left[(i-1) \cdot d - \frac{M-1}{2} \cdot d \right]^2 - 2r_s \cdot d \cdot \left[(i-1) - \frac{M-1}{2} \right] \cdot \sin(\theta_s) \qquad (1)$$

and the corresponding complex response at the ith sensor is

$$a_i(r_s, \theta_s) = \frac{1}{r_{s,i}} \cdot \exp\left(-j\frac{2\pi}{\lambda} \cdot r_{s,i} \right) \qquad (2)$$

assuming a normalized and equal gain for each sensor. The vector $\mathbf{a}(\mathbf{r_s}, \theta_s) = [\mathbf{a_1}, \ldots, \mathbf{a_M}]^{\mathbf{T}}$ is the response of the complete array to the source at (r_s, θ_s).

Likewise, the angle from the ith sensor to the source is

$$\theta_{s,i} = \cos^{-1} \left[\frac{[(i-1) - \frac{M-1}{2}]^2 d^2 + r_{s,i}^2 - r_s^2}{2d[(i-1) - \frac{M-1}{2}]r_{s,i}} \right] - \frac{\pi}{2}. \qquad (3)$$

It is a characteristic of near-field sources that they are viewed at different angles by the different sensors in the array.

Given sensor-angle measurements from any two or more sensors, it is possible to determine the range and bearing (r_s, θ_s) (with respect to the origin) of a source in the near-field. This is, however, subject to identifiability requirements that each sensor has a different

angle to the source. Given $\theta_{s,i}$ and $\theta_{s,j}$ with $i \neq j$, one determines sensor to source ranges $r_{s,i}$ and $r_{s,j}$ respectively using

$$r_{s,i} = [|i - j|] \cdot d \cdot \frac{\cos[\theta_{s,j}]}{\sin[\theta_{s,i} - \theta_{s,j}]} \qquad (4)$$

and

$$r_{s,j} = [|i - j|] \cdot d \cdot \frac{\cos[\theta_{s,i}]}{\sin[\theta_{s,i} - \theta_{s,j}]}. \qquad (5)$$

This requires that $\theta_{s,i} - \theta_{s,j} \neq 0$. The range and bearing with respect to the origin can be determined relative to any of the individual sensors using the individual sensor range and bearing. For example, for the jth sensor, we use $r_{s,j}$ and $\theta_{s,j}$ according to

$$r_s^2 = r_{s,j}^2 + \left[[\frac{M-1}{2} - [j-1]] \cdot d \right]^2 - 2 \cdot r_{s,j} \cdot \left[[\frac{M-1}{2} - [j-1]] \cdot d \right] \sin[\theta_{s,j}] \qquad (6)$$

and

$$\theta_s = \frac{r_{s,j}}{r_s} \cos^{-1}[\theta_{s,j}]. \qquad (7)$$

A.2 Model

Our proposed source characterization technique requires one cooperative source with complex envelope s_k^S in the far-field of the array at known angle θ^S. Steering vectors for the far-field $\mathbf{a}(\theta)$ and near-field $\mathbf{a}(\theta, \mathbf{r})$ take on the standard form with θ being the angle, r denotes range [29].

Assume that the conditions on the test source and sensor array are such that the following signal model is appropriate

$$\mathbf{z_k} = \mathbf{A}\mathbf{s_k} + \mathbf{q_k} + \mathbf{n_k}. \qquad (8)$$

In this model, $\mathbf{z_k}$ is the kth snapshot of sensor data outputs (dimension M). The $\mathbf{q_k}$ represents additive spatial and temporal colored noise produced in the environment and $\mathbf{n_k}$ represents additive white noise modeling the internal noise of the array of sensors receiving system.

The matrix $\mathbf{A}$ can take on one of two forms, depending on whether the local scatterer is best modeled as a collection of P discrete scatterers, or as a single spatially distributed scatterer. For the case of P discrete scatterers

$$\mathbf{A} = \left[\mathbf{a}(\theta^S), \mathbf{a}(\theta_1, \mathbf{r_1}), \ldots, \mathbf{a}(\theta_P, \mathbf{r_P}) \right]. \qquad (9)$$

81

In the above equation, the near-field scatterer $i = 1, \ldots, P$ is characterized by the angle θ_i and range r_i. For a distributed scatterer with scatter amplitude $f[\mathbf{a}(\theta, \mathbf{r})]$ contained in the near-field azimuth and range set Ω,

$$\mathbf{A} = \left[\mathbf{a}(\theta^S), \int_{\theta, \mathbf{r} \in \Omega} \mathbf{f}[\mathbf{a}(\theta, \mathbf{r})] \mathrm{d}\theta \mathrm{d}\mathbf{r} \right]. \tag{10}$$

Likewise, the signal vector $\mathbf{s_k}$ can be constructed in two ways, depending on whether the near-field scatterers are best modeled as discrete or continuous. For the discrete case,

$$\mathbf{s_k} = \left[s_k^S, s_k^1, \ldots, s_k^P \right]^{\mathbf{T}} \tag{11}$$

where the test source complex amplitude is given by s_k^S and the complex amplitude of the ith of P discrete scatterers is denoted as s_k^i. In the continuous scatterer case,

$$\mathbf{s_k} = \left[s_k^S, \mathbf{s_k} \right]^{\mathbf{T}}. \tag{12}$$

The s_k^S and s_k^i and s_k may be uncorrelated, correlated, or coherent for each case respectively.

The spatial covariance matrix $\mathbf{E}[\mathbf{zz^H}]$ is

$$\mathbf{R} = \mathbf{ASA^H} + \mathbf{Q} + \sigma^2 \mathbf{I}. \tag{13}$$

Let the elements of $\mathbf{S}$ be ρ_{ij}. We ensure that the cooperative test source has sufficient signal to noise ratio (generally greater than 50dB) to perform our measurement by requiring that

$$\rho_{\mathrm{snr}} = \frac{\rho_{11}}{(\sigma^2 + \mathrm{tr}[\mathbf{Q}])} \gg 1. \tag{14}$$

It is also expected that the direct far-field source power will be substantially greater than the total near-field power (by 20–40dB)

$$\rho_{\mathrm{snf}} = \frac{\rho_{11}}{\sum_{k=2}^{P} \rho_k} \gg 1. \tag{15}$$

A.3 Background

Breed and Posch [27] introduced the spatial Wigner distribution as a tool for determining the range and angle of a near-field source. They exploited the property that the phase front of a wave emanating from a source in the near-field of an array has an approximately quadratic phase law, or equivalently an approximately linear spatial frequency

law. They then determined source location by determining the parameters governing the linear frequency law as represented by the Wigner distribution applied to the spatial signal. The true propagating wave phase front is in fact spherical and is only approximately quadratic for near-field sources some distance from the array. The method proposed in [27] breaks down for sources close to the array. Swindlehurst and Kailath [30] examined the applicability of the quadratic-spherical approximation and apply a parametric high resolution technique to determine the linear frequency law parameters (and hence the near-field source position). However, it can be seen from equations (4) through (7) that it is possible to determine the source position without invoking the quadratic phase approximation to the spherical phase front.

There is a substantial body of literature concerned with processing spatial signals received by an array of sensors from sources in the near-field of the array. It is mostly concerned with techniques for estimating the angle and range of the source. For example, both subspace and maximum likelihood algorithms are derived in [31]. Subsequently we will present an example showing near-field characterization using both the sensor-angle distribution (discussed next) and the near-field MUSIC, as developed in [31].

Several authors have proposed methods for determining the angle of distributed sources located in the far-field of an array [32]. These techniques address the effect of scatter local to a transmitter in the far-field and not for scatter that is sufficiently local to the receiving system to be in the near-field of the array.

B. Sensor-Angle Distributions

Our method extends the spatial Wigner distribution introduced by Breed and Posch. To avoid confusion it has been necessary to change the name to reflect the generalization to all members of Cohen's class of quadratic distributions [1]. While the title "spatial Wigner distribution" is informative, retaining the name "spatial time-frequency distribution" for the remaining members of Cohen's class applied to spatial signals does not correctly describe the distribution we are interested in, and will be confused with STFD discussed in earlier sections of this chapter. Therefore, in this work we have renamed the class of quadratic distributions applied to spatial signals to be *sensor-angle distributions* (SAD). The corresponding spectra are called sensor-angle spectra (SAS).

83

The Cohen's class SAD for the kth snapshot is a distribution of the angle of sources impinging on the array *at each sensor*.

$$\mathbf{T_k}(\mathbf{i}, \theta; \mathbf{z_k}) = \sum_{\mathbf{v}=-\infty}^{\infty} \sum_{\mathbf{l}=-\infty}^{\infty} \phi(\mathbf{v}, \mathbf{l}) \mathbf{z_k}(\mathbf{i}+\mathbf{v}+\mathbf{l}) \mathbf{z_k^*}(\mathbf{i}+\mathbf{v}-\mathbf{l}) e^{-\mathbf{j}4\pi\theta\mathbf{l}} \tag{16}$$

where i and θ are the sensor index and angle respectively. The kernel $\phi(v, l)$ characterizes the distribution and is a function of sensor position and sensor lag. All the standard kernel designs applied in the time-frequency literature may be used with the SAD.

The sensor-angle spectrum (SAS) is the *power* (not energy or energy density) distribution of the sources impinging on the array. The SAS is given by

$$\mathbf{T^S}(\mathbf{i}, \theta; \mathbf{z}) = \mathbf{E}[\mathbf{T_k}(\mathbf{i}, \theta; \mathbf{z_k})] \tag{17}$$

where an estimate for temporally stationary sources is given by

$$\mathbf{\hat{T}^S}(\mathbf{i}, \theta; \mathbf{z}) = \frac{1}{\mathbf{N}} \sum_{\mathbf{k}=0}^{\mathbf{N-1}} \mathbf{T_k}(\mathbf{i}, \theta; \mathbf{z_k}) \tag{18}$$

for N snapshots.

C. Characterizing Local Scatter

The objective is to use data received by the array from a test source in the far-field that illuminates the local near-field scatterer distribution and to visualize and characterize this scatterer distribution using the SAS. We expect the test signal to be substantially more powerful than the local scatter we wish to characterize (see (15)). Subspace projection is applied to the array snapshots to remove the dominant far-field component and allow a clear depiction of the near-field source in the sensor-angle (s-a) domain.

In (16) and (17), the data snaphot $\mathbf{z_k}$ is replaced by $\mathbf{P}^{\theta^S}\mathbf{z_k}$ where $\mathbf{P}^{\theta^S}$ is the orthogonal projection operator formed from the far-field test source steering vector $\mathbf{a}(\theta^S)$ as

$$\mathbf{P}^{\theta^S} = \mathbf{I} - \mathbf{a}(\theta^S)[\mathbf{a^H}(\theta^S)\mathbf{a}(\theta^S)]^{-1}\mathbf{a^H}(\theta^S). \tag{19}$$

Therefore, we compute the modified SAS

$$\mathbf{\hat{T}^S}(\mathbf{i}, \theta; \mathbf{P}^{\theta^S}, \mathbf{z}). \tag{20}$$

In some applications, a single test angle will provide sufficient characterization using (20) while in other applications, two or several test angles will be required, in which case θ^S is scanned over the required domain of angles for the test source.

D. Simulations and Examples

The following example is used to demonstrate the proposed approach for near scattering characterizations. Consider a 32 sensor linear equi-spaced array operating at a carrier frequency of 6.41MHz and with 15m sensor spacing. The local scatterer distribution comprises a point scatterer in the near-field at a range of 400m and bearing of 30 degrees in front of the array (the array has total length 465m). Assume the test source is temporally stationary and located at 20 degrees angle with respect to boresight. The test source is coherent with and 20dB stronger than the scattered source. In this example we have used the alias-free Wigner distribution [33]. Of course others members of Cohen's class may also be used.

Figure 11 shows the SAD for the received data. The SAD is dominated by the substantially more powerful far-field test source and there is no clear indication of any additional scattering. The far-field source has the same angle for every sensor, and therefore, depicts a horizontal signature in the s-a domain. In Fig. 12 we have applied the orthogonal projection operator and computed the SAD for $\mathbf{P}^{\theta^S}\mathbf{z_k}$. The SAD now clearly shows the presence of near-field local scatter. The location of the near-field source may be determined using equations (4)–(7).
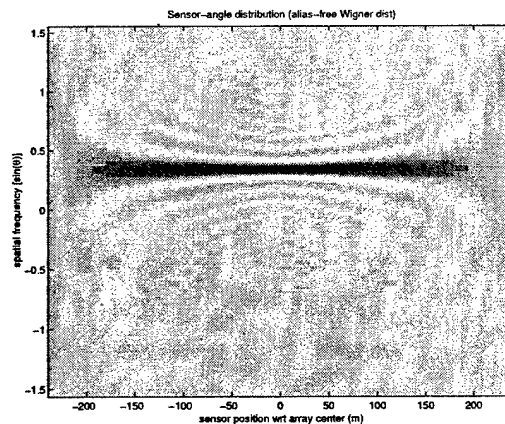

Fig. 11. SAD for the received data $\mathbf{z_k}$. The far-field test source dominates the SAD characterization.

The beampatterns for the cases of $\mathbf{z_k}$ and $\mathbf{P}^{\theta^S}\mathbf{z_k}$ are shown in Fig. 13. The presence of near-field scatterers cannot be confirmed as compared with alternative explanations for the distorted beampatterns, such as poor array calibration.
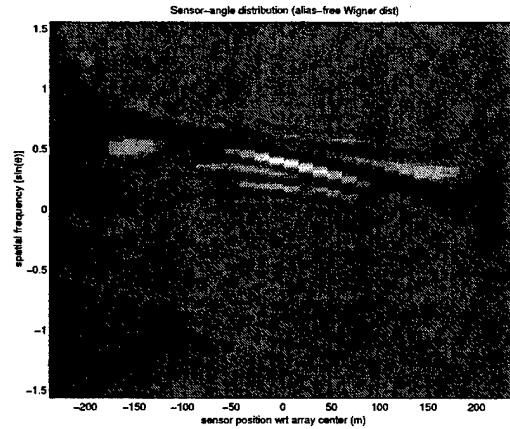
Fig. 12. SAD for the received data $\mathbf{P}^{\theta^S}\mathbf{z_k}$. With the direct propagation path from the far-field test signal removed by the orthogonal projection operator the local scatterer spectrum is revealed.
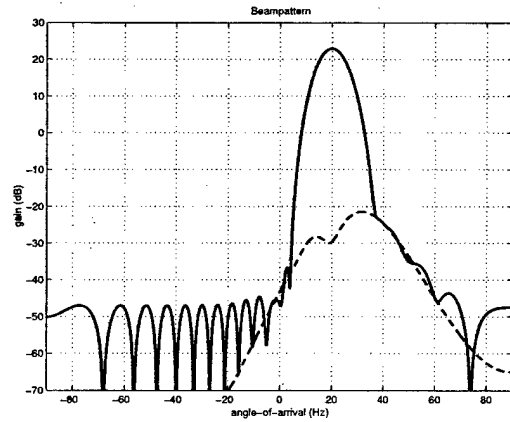

Fig. 13. Beampattern for $\mathbf{z_k}$ (—) and $\mathbf{P}^{\theta^S}\mathbf{z_k}$ (--). Without the sensor-angle characterization it is not possible to identify perturbations from the ideal test source beampattern as being due to near-field scatter.

The projection approach has also been applied to real data collected from a 16 sensor HF receiving array. An array calibration source was transmitted from the far-field of the array at boresight. The sensor angle distribution is shown in Fig. 14 and is dominated by the calibration source. Following calibration of the array using the calibration source, the received and calibrated boresight source is removed using orthogonal projection. The sensor angle distribution of the residual is shown in Fig. 15. No discrete near-field scatterers are apparent, however there is a concentration in the SAD in the upper left region of the distribution. This indicates that there is some asymmetric local scattering near the array.

A second example is used to contrast the SAD with existing techniques for near-field
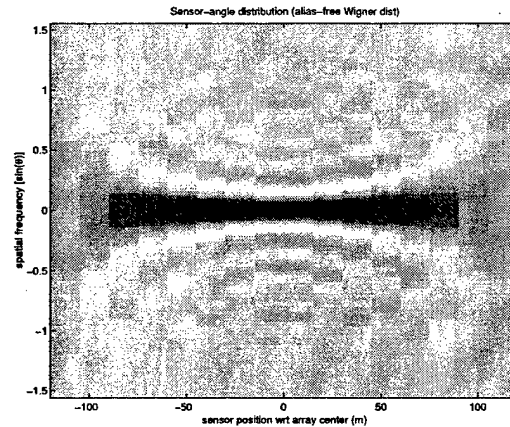
Fig. 14. SAD for the real received data. The far-field calibration source at boresight dominates the SAD characterization.
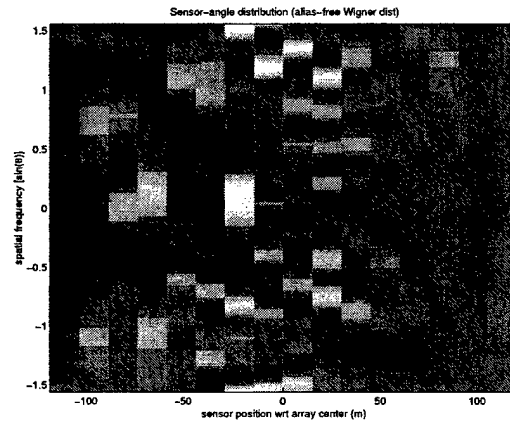
Fig. 15. SAD for the real received data with the direct propagation path from the far-field calibration source removed by orthogonal projection operator. The local scatterer sensor-angle distribution is revealed.

sources characterization. In this case, we have chosen to compare with an implementation of near-field MUSIC as described by [31]. We consider an ideal computer generated case and an equivalent case where the data has been collected using a real HF radar array.

Consider an ideal case with a single source placed at range 80m and bearing 10.5 degrees. Assume a 16 sensor array, that source signal to noise power ratio is high and 102 array data snapshots are available (generated using computer). Figs. 16 and 17 respectively, show the near-field MUSIC diagram and the SAS, both computed using all 102 data snapshots. The source is well localized using MUSIC, and there is a characteristic structure in the SAS showing sensor-angle for each sensor in the array.

87
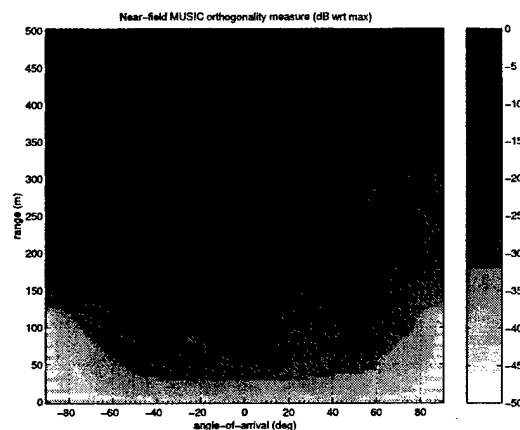
Fig. 16. Near-field MUSIC diagram for an ideal source at range 80m and bearing 10.5 degrees.
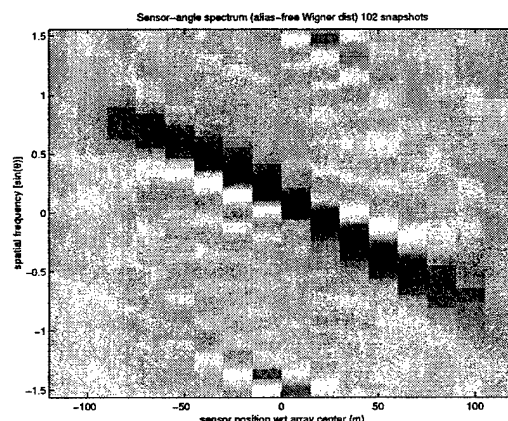
Fig. 17. sensor-angle spectrum for an ideal source at range 80m and bearing 10.5 degrees.

We have repeated the analysis, but this time used 102 data snapshots collected from the HF radar receiving array. The near-field source was approximately 80m from the array mid-point at an angle of approximately 10 degrees. In this case the source was behind the array. The exact location is not known precisely. Figs. 18 and 19 show the near-field MUSIC diagram and the SAS respectively. Imprecise array calibration has smeared the localization in the MUSIC diagram while the structure in the SAS is preserved.

VIII. Conclusion

We have presented two different new perspectives of time-frequency distributions. One perspective is driven by direction finding and blind source separation problems, whereas the other stems from the need to characterize near-field sources or reflectors. The fun-
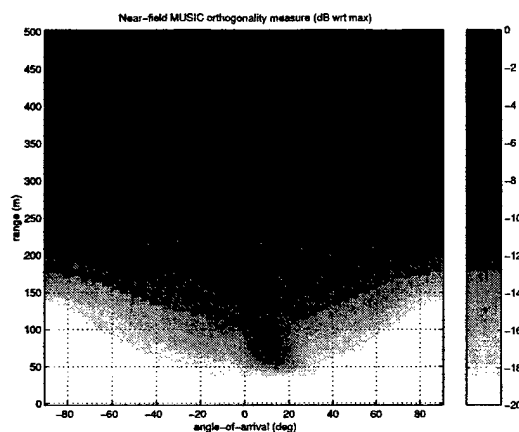
Fig. 18. Near-field MUSIC diagram for a real source placed at approximately range 80m and bearing 10.5 degrees.
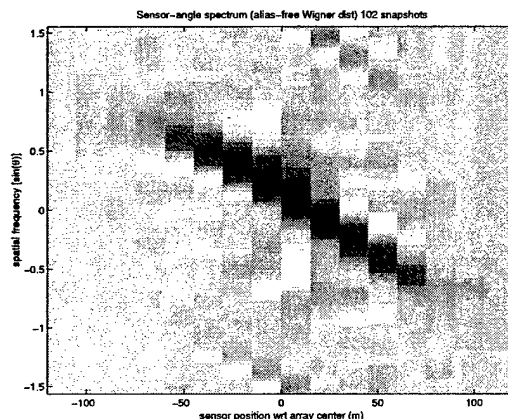
Fig. 19. sensor-angle spectrum for a real source placed at approximately range 80m and bearing 10.5 degrees.

damental offering of quadratic distributions in both cases is the ability to discriminate between the sources based on the joint-variable signatures of their respective waveforms. This allows the enhancement of signal-to-noise ratio (SNR) as well as the consideration of only the sources of interest, and subsequently improve the estimation of the source positions and waveforms.

The first six sections presented the general framework of spatial time-frequency distributions (STFDs). The advantages of a STFD matrix over the covariance matrix-based approach to array processing are the SNR enhancement and the robustness of the eigenstructure to noise. A variety of methods have been introduced for both blind source

separation and direction finding applications using STFDs. The first class of source separation methods are based on pre-whitening and the recovery of a unitary matrix. Unlike similar methods based on second-order statistics, which cannot separate signals with the same spectra, the STFD-based method can separate nonstationary signals with identical spectra when they have different time-frequency signatures. The SNR enhancement and signal localization properties in the time-frequency domain can substantially improve the source separation performance. The second class of source separation methods are based on array averaging of the time-frequency distribution, signal synthesis, and waveform recovery using the minimum mean square error criterion. For direction finding, both the MUSIC and the maximum likelihood methods have been extended and modified to incorporate the STFDs. The performance improvement, evident by both the analytical and simulation results, is most significant when the input SNR of source arrivals is low, and/or when the sources are closely spaced.

In the second part of the chapter, we have used the time-frequency distribution of the spatial signal received by an array to characterize sources based on their angle at each sensor. This sensor-angle distribution is a tool for characterizing near-field scatter local to the receiving array. The method uses a test source in the far-field to illuminate the local scatterer distribution. An orthogonal projection operator derived from the steering vector for the far-field test source is used to exclude the direct propagation path from the test source in the characterization. As part of the characterization we exploit the spatial Wigner distribution although we have renamed it the sensor-angle distribution to avoid confusion with a similarly named but differently defined STFD discussed in the first part of the chapter. We have shown the application of the method using simulation and for real data collected using an HF radar receiving array. Additional simulations and real data results contrast the SAD characterization with that of a conventional near-field localization technique (in this case near-field MUSIC).

References

[1] L. Cohen, *Time-Frequency Analysis*. Englewood Cliffs, NJ: Prentice Hall, 1995.

[2] S. Qian and D. Chen, *Joint Time-Frequency Analysis*, Englewood Cliffs, NJ: Prentice Hall, 1996.

[3] F. Hlawatsch and G. Boudreau-Bartles, "Linear and quadratic time-frequency signal representations," *IEEE Signal Processing Mag.*, vol. 9, no. 2, pp. 21–68, April 1992.

[4] M. G. Amin, "Time-frequency distributions in statistical signal and array processing," section in T. Chen (ed.), "Highlights of statistical signal and array processing," *IEEE Signal Processing Mag.*, vol. 15, no. 5, Sept. 1998.

[5] M. G. Amin and A. N. Akansu, "Time-frequency for interference excision in spread spectrum communications," section in G. Giannakis (ed.), "Highlights of signal processing for communications," *IEEE Signal Processing Mag.*, vol. 16, no. 2, March 1999.

[6] M. G. Amin and A. R. Lindsey, "Time-frequency interference mitigation in spread spectrum communication systems," in B. Boashash (ed.), *Time-Frequency Signal Analysis and Processing*, Englewood Cliffs, NJ: Prentice Hall, 2002.

[7] M. G. Amin and Y. Zhang, "Spatial time-frequency distributions and their applications," in B. Boashash (ed.), *Time-Frequency Signal Analysis and Processing*, Englewood Cliffs, NJ: Prentice Hall, 2002.

[8] A. Belouchrani and M. G. Amin, "Blind source separation based on time-frequency signal representation," *IEEE Trans. Signal Processing*, vol. 46, no. 11, pp. 2888–2898, Nov. 1998.

[9] A. Belouchrani and M. Amin, "Time-frequency MUSIC," *IEEE Signal Processing Letters*, vol. 6, no. 5, pp. 109–110, May 1999.

[10] Y. Zhang, W. Mu, and M. G. Amin, "Time-frequency maximum likelihood methods for direction finding," *J. Franklin Inst.*, vol. 337, no. 4, pp. 483–497, July 2000.

[11] Y. Zhang and M. G. Amin, "Blind separation of sources based on their time-frequency signatures," in *Proc. IEEE Int. Conf. Acoust., Speech, Signal Process.*, Istanbul, Turkey, pp. 3132–3135, June 2000.

[12] K. Sekihara, S. Nagarajan, D. Poeppel, and Y. Miyashita, "Time-frequency MEG-

MUSIC algorithm," *IEEE Trans. Medical Imaging*, vol. 18, no. 1, pp. 92–97, Jan. 1999.

[13] G. H. Golub and C. F. Van Loan, *Matrix Computations*, 3rd edition. Baltimore, MD: Johns Hopkins University Press, 1996.

[14] Y. Zhang, W. Mu, and M. G. Amin, "Subspace analysis of spatial time-frequency distribution matrices," *IEEE Trans. Signal Processing*, vol. 49, no. 4, pp. 747–759, Apr. 2000.

[15] P. Stoica and A. Nehorai, "MUSIC, maximum likelihood, and Cramer-Rao bound," *IEEE Trans. Acoust. Speech, Signal Process.*, vol. 37, no. 5, pp. 720–741, May 1989.

[16] H. I. Choi and W. J. Williams, "Improved time-frequency representation of multi-component signals using exponential kernels," *IEEE Trans. Acoust., Speech, Signal Process.*, vol. 37, pp. 862–871, June 1989.

[17] W. Mu, Y. Zhang, and M. G. Amin, "Bilinear signal synthesis in array processing," in *Proc. Int. Conf. Acoust., Speech, Signal Process.*, Salt Lake City, UT, pp. 3577-3580, May 2001.

[18] G. Boudreaux–Bartels and T. Parks, "Time–varying filtering and signal estimation using Wigner distribution synthesis techniques," *IEEE Trans. Acoust., Speech, Signal Process.*, vol. ASSP–34, no. 3, pp. 442–451, June 1986.

[19] J. Jeong and W. Williams, "Time–varying filtering and signal synthesis," in B. Boashash ed., *Time–Frequency Signal Analysis — Methods and Applications*, Longman Cheshire, 1995.

[20] Y. Zhang and M. G. Amin, "Spatial averaging of time-frequency distributions for signal recovery in uniform linear arrays," *IEEE Trans. Signal Processing*, vol. 48, no. 10, pp. 2892–2902, Oct. 2000.

[21] A. Belouchrani, K. Abed-Meraim, M. G. Amin, and A. M. Zoubir, "Joint anti-diagonalization for blind source separation," in *Proc. Int. Conf. Acoust., Speech, Signal Process.*, Salt Lake City, UT, May 2001.

[22] R. O. Schmidt, "Multiple emitter location and signal parameter estimation," *IEEE Trans. Antennas Propagat.*, vol. 34, no. 3, pp. 276–280, March 1986.

[23] I. Ziskind and M. Wax, "Maximum likelihood localization of multiple sources by

alternating projection," *IEEE Trans. Acoust. Speech Signal Process.*, vol. ASSP-36, no. 10, pp. 1553–1560, 1988.

[24] P. Stoica and A. Nehorai, "MUSIC, maximum likelihood, and Cramer-Rao bound: further results and comparisons," *IEEE Trans. Acoust. Speech, Signal Process.*, vol. 38, no. 12, pp. 2140–2150, 1990.

[25] M. G. Amin and Y. Zhang, "Direction finding based on spatial time-frequency distribution matrices," *Digital Signal Processing*, vol. 10, no. 4, pp. 325–339, Oct. 2000.

[26] M. G. Amin, A. Belouchrani, and Y. Zhang, "The spatial ambiguity function and its applications," *IEEE Signal Processing Letters*, vol. 7, no. 6, pp. 138–140, June 2000.

[27] B. R. Breed and T. E. Posch, "A range and azimuth estimator based on forming the spatial Wigner distribution," in *Proc. Int. Conf. Acoust., Speech, Signal Process.*, pp. 41B.9.1–41B.9.2, 1984.

[28] G. J. Frazer and Y. I. Abramovich, "Quantifying multi-channel receiver calibration," Tech. Rep. DSTO-TR-1152, Defence Science and Technology Organisation, Edinburgh, SA, Australia, June 2001.

[29] D. H. Johnson and D. E. Dudgeon, *Array Signal Processing: Concepts and Techniques*, Prentice-Hall Signal Processing Series. Prentice-Hall, 1993.

[30] A. L. Swindlehurst and T. Kailath, "Near-field source parameter estimation using a spatial Wigner distribution approach," in *Advanced Algorithms and Architectures for Signal Processing III*. SPIE, vol. 975, pp. 86–92, 1988.

[31] Y. D. Huang and M. Barkat, "Near-field multiple source localization by passive sensor array," *IEEE Trans. Antennas Propagat.*, vol. 39, no. 7, pp. 968–975, July 1991.

[32] S. Valaee, B. Champagne, and P. Kabal, "Parametric localization of distributed sources," *IEEE Trans. Signal Processing*, vol. 43, no. 9, pp. 2144–2153, Sept. 1995.

[33] J. Jeong and W. J. Williams, "Alias-free generalized discrete-time time-frequency distributions," *IEEE Trans. Signal Processing*, vol. 40, no. 11, pp. 2757–2765, Nov. 1992.

Interference Suppression in Spread Spectrum Communication Systems

Moeness G. Amin and Yimin Zhang

Villanova University, PA

Abstract

This chapter discusses interference excision techniques in spread spectrum communications systems. Both stationary and nonstationary interferers are considered. Sinusoidal, auto-regressive, digital communication, and polynomial phase interference signals are effectively suppressed by different excision methods; each is suitable for one or more types of interferers. Time-, frequency-, and time-frequency domain methods for analysis and estimation of the interference parameters are summarized. Domains other than time and frequency, such as the Gabor-domain, the Wavelet-domain, and quadratic time-frequency signal representations, are appropriate for non-traditional smart jamming in which the interference parameters are highly dependent on time. Excision methods can be linear, bilinear, or nonlinear with performance dependent on the interference power relative to the desired signal and noise. In some cases, the slight performance enhancement offered by bilinear and nonlinear methods may not properly justify the increase in the algorithm complexity. The BER and receiver SINR expressions and curves are presented in this chapter for some of the key interference excision techniques.

I. Introduction

Suppression of correlated interference is an important aspect of modern broadband communication platforms. For wireless communications, in addition to the presence of benign interferers, relatively narrowband cellular systems, employing time division multiple access (TDMA) or advanced mobile phone system (AMPS) may coexist within the same frequency band of the broadband code division multiple access (CDMA) systems. Hostile jamming is certainly a significant issue in military communication systems. Global positioning system (GPS) receivers potentially experience a mixture of both narrowband and wideband interference, both intentionally and unintentionally [1].

One of the fundamental applications of spread spectrum (SS) communication systems is its inherent capability of interference suppression. SS systems are implicitly able to provide a certain degree of protection against intentional or unintentional interferers. However, in some cases, the interference might be much stronger than the SS signal, and the limitations on the spectrum bandwidth render the processing gain insufficient to decode the useful signal reliably. For this reason, signal processing techniques are frequently used in conjunction with the SS receiver to augment the processing gain, permitting greater interference protection without an increase in the bandwidth. Although much of the work in this area has been motivated by the applications of SS as an anti-jamming method in military communications, it is equally applicable in commercial communication systems where SS systems and narrowband communication systems may share the same frequency bands.

This article covers both the direct-sequence spread spectrum (DS/SS) and frequency hopping (FH) communication systems, but the main focus is on the DS/SS communication systems. For DS/SS communication systems, two types of interference signals are considered, namely, narrowband interference (NBI) and nonstationary interference, such as instantanously narrowband interference (INBI).

The early work on narrowband interference rejection techniques in spread spectrum communications has been reviewed comprehensively by Milstein in [2]. Milstein discusses in depth two classes of rejection schemes: 1) those based on least-mean square (LMS) estimation techniques, and 2) those based on transform domain processing structures. The

improvement achieved by these techniques is subject to the constraint that the interference be relatively narrowband with respect to the DS/SS signal waveform. Poor and Rusch [3] have given an overview of NBI suppression in SS with the focus on CDMA communications. They categorize CDMA interference suppression by linear techniques, nonlinear estimation techniques, and multiuser detection techniques (multiuser detection is outside the scope of this article). Laster and Reed [4] have provided a comprehensive review of interference rejection techniques in digital wireless communications, with the focus on advances not covered by the previous review articles.

Interference suppression techniques for nonstationary signals, such as INBI, have been summarized by Amin and Akansu [5]. The ideas behind NBI suppression techniques can be extended to account for the nonstationary nature of the interference. For time-domain processing, time-varying notch filters and subspace projection techniques can be used to mitigate interferers characterized by their instantaneous frequencies and instantaneous bandwidths. Interference suppression is achieved using linear and bilinear transforms, where the time-frequency domain and wavelet/Gabor domain are typically considered. Several methods are available to synthesize the nonstationary interference waveform from the time-frequency domain and subtract it from the received signal.

Interference rejection for FH is not as well developed as interference rejection for DS or for CDMA. In FH systems, the fast FH (FFH) is of most interest, and the modulation most commonly used in FH is frequency-shift keying (FSK). Two types of interference waveforms can be categorized, namely, partial-band interference (PBI) and multitone interference (MTI). Typically, interference suppression techniques for FH communication systems often employ a whitening or clipping stage to reject interference, and then combined by diversity techniques.

II. Signal Model

The received waveform consists of a binary phase-shift-keying (BPSK) DS/SS signal $s(t)$, an interfering signal $u(t)$, and thermal noise $b(t)$. Without loss of generality, we consider the single-interferer case, and additive Gaussian white noise (AGWN) that is uncorrelated with both the DS/SS and the interference signals. The input to the receiver,

$x(t)$, is given by

$$x(t) = s(t) + u(t) + b(t). \tag{1}$$

The DS/SS signal can be expressed as

$$s(t) = \sum_{l=-\infty}^{\infty} d(l)p(t - lT_c), \tag{2}$$

where T_c is the chip duration, $p(t)$ is the shaping waveform,

$$d(l) = s(n)c(n, l) \tag{3}$$

is the chip sequence, $s(n) \in [-1, +1]$ is the nth symbol, and $c(n, l) \in [-1, +1]$ is a pseudo-noise (PN) sequence used as the spreading code for the nth symbol. The PN sequence can be either periodic and aperiodic. Different types of interference signals are considered.

For discrete-time filter implementations, signals are sampled at the rate $1/T$. Typically, the sampling interval T is equal to the chip duration T_c. The input to the receiver, after sampling, becomes

$$x[n] = x(nT). \tag{4}$$

The samples of the DS/SS signal, interference, and noise, can be defined accordingly as $s[n]$, $u[n]$, and $b[n]$, respectively.

III. Narrowband Interference Suppression

Interference suppression techniques for DS/SS systems are numerous. In particular, much literature exists on the adaptive notch filtering as it relates to suppress NBI on a wideband DS/SS signal. Synthesis/subtraction is another well-established technique for sinusoidal interference suppression. Other techniques include nonlinear adaptive filtering and multiuser detection techniques.

A. Adaptive Notch Filtering

The basic idea in employing an adaptive notch filter is to flatten the filter input spectrum. An SS signal tends to have a uniform wide spectrum and is affected little by the filtering process, whereas the NBI is characterized by spectral spikes and frequency regions of high concentrated power. The adaptive notch filter places notches at the frequency location of the NBI to bring the interference level to the level of the SS signal. At least two

main approaches exist for constructing an adaptive notch filter: (1) estimation/subtraction type filters and (2) transform-domain processing structures.

Estimation/Subtraction Type Filters

If the interference is relatively narrowband compared with the bandwidth of the spread spectrum waveform, then the technique of interference cancellation by the use of notch filters often results in a large improvement in system performance. This technique, described in many references including [6], [7], [8], [9], uses a tapped delay line to implement the prediction-error filter (Wiener filter [10]). Since both the DS signal and the thermal noise are wideband processes, their future values cannot be readily predicted from their past values. On the other hand, the interference, being a narrow-band process, can indeed have its current and future values predicted from past values. Hence, the current value, once predicted, can be subtracted from the incoming signal, leaving an interference-free waveform comprised primarily of the DS signal and the thermal noise. A general diagram of this technique is depicted in Fig. 1. Both one-sided and two-sided transversal filters can be used for this purpose. When two-sided filters are used, the estimation of current interference value is based on both past and future values of the interference. Consider a single-sided filter as shown in Fig. 2. Define an N-dimensional vector $\mathbf{x}[n]$, denoted as

$$\mathbf{x}[n] = (x[n-1], \cdots, x[n-N])^T, \tag{5}$$

where the superscript T denotes transpose of a vector or a matrix. The DS/SS signal, interference, and noise vectors can be defined similarly as $\mathbf{s}[n]$, $\mathbf{u}[n]$, $\mathbf{b}[n]$, respectively. We also define the corresponding weight vector $\mathbf{w}$ as

$$\mathbf{w} = [w_1, \cdots, w_N]^T. \tag{6}$$

Hence, the output sample of the filter is

$$y[n] = x[n] - \mathbf{w}^T \mathbf{x}[n]. \tag{7}$$

The mean square value $E[y^2[n]]$, representing the output average power, is given by

$$
\begin{aligned}
E\left(y^2[n]\right) &= E\left(x^2[n]\right) - 2\mathbf{w}^T E\left(x[n]\mathbf{x}[n]\right) + \mathbf{w}^T E\left(\mathbf{x}[n]\mathbf{x}^T[n]\right)\mathbf{w} \\
&\triangleq E\left(x^2[n]\right) - 2\mathbf{w}^T \mathbf{p} + \mathbf{w}^T \mathbf{R}\mathbf{w},
\end{aligned} \tag{8}
$$

98

where $\mathbf{p} = E\left(x[n]\mathbf{x}[n]\right)$ is the correlation vector between $x[n]$ and $\mathbf{x}[n]$, and

$$\mathbf{R} = E\left(\mathbf{x}[n]\mathbf{x}^T[n]\right) \tag{9}$$

is the covariance matrix of $\mathbf{x}[n]$. It is noted that, when the PN sequence is sufficiently long, the PN signal samples at different taps are approximately uncorrelated. On the other hand, samples of the narrowband interference at different taps has high correlations. Since the DS/SS signal, interference, and thermal noise are mutually uncorrelated, then,

$$
\begin{aligned}
\mathbf{p} \quad &= E\left(x[n]\mathbf{x}[n]\right) \\
&= E\left\{\left(s[n] + u[n] + b[n]\right)\left(\mathbf{s}[n] + \mathbf{u}[n] + \mathbf{b}[n]\right)\right\} \\
&= E\left(u[n]\mathbf{u}[n]\right).
\end{aligned} \tag{10}
$$

Minimizing the output power $E[y^2[n]]$ yields the following well-known Wiener-Hopf solution for the optimum weight vector $\mathbf{w}_{\text{opt}}$,

$$\mathbf{w}_{\text{opt}} = \mathbf{R}^{-1}\mathbf{p}. \tag{11}$$

The cost of notch filtering is the introduction of some distortion into the SS signal. Such distortion results in power loss of the desired DS/SS signal as well as the introduction of self-noise. Both effects become negligible when the processing gain is sufficiently large.

Note that when precise statistical knowledge of the interference cannot be assumed, adaptive filtering can be used to update the tap weights. There are a variety of adaptive algorithms and receiver structures [7], [11], [12], [10]. The optimum Wiener-Hopf filter can be implemented by using direct matrix inversion (DMI) or recursive adaptation methods. For the DMI method, the covariance matrix $\mathbf{R}$ and $\mathbf{p}$ are estimated at time n by using most recent N_t data samples, i.e.,

$$\hat{\mathbf{R}}[n] = \frac{1}{N_t}\sum_{l=0}^{N_t-1}\mathbf{x}[n-l]\mathbf{x}^T[n-l] \tag{12}$$

and

$$\hat{\mathbf{p}}[n] = \frac{1}{N_t}\sum_{l=0}^{N_t-1}x[n-l]\mathbf{x}^T[n-l] \tag{13}$$

The least mean square (LMS) algorithm is a simple and stable method to implement an iterative solution to the Wiener-Hopf equation without making use of any *a priori*

statistical information about the received signal. Using the instantaneous estimates of the covariance matrix and cross-correlation vector of Eqns. (9) and (10), the LMS algorithm can be expressed as

$$\mathbf{w}[n+1] = \mathbf{w}[n] + \mu y[n]\mathbf{x}[n], \qquad (14)$$

where $\mathbf{w}[n]$ is the filter weight vector of elements $w_l[n], l = 1, 2, \cdots, N$, $\mathbf{x}[n]$ is the vector that includes the data within the filter, and $y[n]$ is the output, all at the nth adaptation, and μ is a parameter that determines the rate of convergence of the algorithm. It is noted that in most applications of the LMS algorithm, an external reference waveform is needed in order to correctly adjust the tap weights. However, in this particular application, the signal on the reference tap $x[n]$ serves as the external reference.

The drawback of LMS algorithm is its slow convergence. To improve the convergence performance, techniques including self-orthogonalizing LMS, recursive least squares (RLS), and lattice structure can be used [13], [10].

SINR and BER Analysis

The output signal-to-interference-plus-noise ratio (SINR) and bit error rate (BER) are two important measures for communication quality and the performance enhancement using the signal processing techniques.

To derive the output SINR, we rewrite the filter output as [1]

$$y[n] = \sum_{l=0}^{N} w_l x[n-l] = \sum_{l=0}^{N} w_l(c[n-l] + u[n-l] + b[n-l]). \qquad (15)$$

where $w_0 = 1$. The signal $\{y[n]\}$ is then fed to the PN correlator. Denote L as the number of chips per information bit. Then the output of the PN correlator, which is the decision variable for recovering the binary information, is expressed as

$$
\begin{aligned}
r &= \sum_{n=1}^{L} y[n]c[n] = \sum_{n=1}^{L} c[n] \sum_{l=0}^{N} w_l(c[n-l] + u[n-l] + b[n-l]) \\
&= \sum_{n=1}^{L} c^2[n] + \sum_{n=1}^{L} c[n] \sum_{l=1}^{N} w_l c[n-l] + \sum_{n=1}^{L} c[n] \sum_{l=0}^{N} w_l(u[n-l] + b[n-l]) \\
&= L + \sum_{n=1}^{L} c[n] \sum_{l=1}^{N} w_l c[n-l] + \sum_{n=1}^{L} \sum_{l=0}^{N} c[n]w_l u[n-l] + \sum_{n=1}^{L} \sum_{l=0}^{N} c[n]w_l b[n-l].
\end{aligned}
$$

[1]To keep the notation simple, we have used in (15) the same symbol w_l as in (6). The two sets of weights, however, differ in sign.

100

$$\text{(16)}$$

The first term on the right-hand side of (16) represents the desired signal component, the second term amounts to the self-noise caused by the dispersive characteristic of the filter, and the third term is the residual narrowband interference escaping the excision process and appearing at the output of the PN correlator. The last term in (16) is the additive noise component.

The mean value of r is

$$E(r) = L \qquad \text{(17)}$$

and the variance is [7]

$$\text{var}(r) \underline{\triangle} \sigma^2 = L \sum_{l=1}^{N} w_l^2 + L \sum_{n=1}^{N} \sum_{l=0}^{N} w_n w_l \rho[n-l] + L\sigma_n^2 \sum_{l=0}^{N} w_l^2, \qquad \text{(18)}$$

where $\sigma_n^2 = E(b^2[n])$ is the AGWN variance and

$$\rho[n-l] = E\left(u[k]u[k+n-l]\right).$$

The three terms of the right-hand side of (18) represent the mean square values caused by the self-noise, residual narrowband interference, and noise, respectively.

The output SINR is defined as the ratio of the square of the mean to the variance. Thus,

$$\text{SINR}_0 = \frac{E^2(r)}{\text{var}(r)} = \frac{L}{\sum_{l=1}^{N} w_l^2 + \sum_{n=1}^{N} \sum_{l=0}^{N} w_n w_l \rho[n-l] + \sigma_n^2 \sum_{l=0}^{N} w_l^2}. \qquad \text{(19)}$$

Note that, if there is no interference suppression filter, $w_l = 1$ for $l = 0$ and zero otherwise. Therefore, the corresponding output SINR is

$$\text{SINR}_{no} = \frac{L}{\rho[0] + \sigma_n^2}. \qquad \text{(20)}$$

If we assume that the self-noise, residual interference, and noise components at the output of correlator is Gaussian, then the BER can be evaluated in the same manner as the conventional BPSK corrupted only by AWGN. Under such assumption, the BER is given by

$$P_b = P(r < 0) = \int_{-\infty}^{0} \frac{1}{\sqrt{2\pi}\sigma} e^{-(r-L)^2/2\sigma^2} dr = Q\left(\sqrt{\text{SINR}_0}\right), \qquad \text{(21)}$$

where

$$Q(x) = \frac{1}{\sqrt{2\pi}} \int_x^\infty e^{-v^2/2} dv \qquad (22)$$

is the Q-function [13].

Transform-Domain Processing Structures

An alternative to time-domain excision as described in the preceding section, is to transform the received signal to the frequency domain and perform the excision in that domain. Clipping and gating methods can then be applied on those transform bins contaminated by the interference.

Surface acoustic wave (SAW) device technology can be used to produce the continuous-time Fourier transform of the received waveform [14], [15]. The discrete Fourier transform (DFT), with FFT implementations, is commonly applied for time-sampled signals [16]. Adaptive subband transforms generalize transform-domain processing [17], [18], and can yield uncorrelated transform coefficients.

The interference-suppressed signal based on a block transform can be written as

$$\mathbf{x}_s[n] = \mathbf{BEAx}[n], \qquad (23)$$

where $\mathbf{x}[n]$ is the received input vector, $\mathbf{A}$ and $\mathbf{B}$ are the forward transform matrix and inverse transform matrix, respectively, and $\mathbf{E}$ is a diagonal matrix with each diagonal element acting as a weight multiplied to the input signal at each transform bin. The weights can be controlled by different schemes. Two commonly used methods are either to set the weights binary (i.e., a weight is either one or zero) or to adjust the weights adaptively. In applying the first method, powerful NBI is detected by observing the envelope of the spectral waveform. Substantial interference suppression can be achieved by multiplying the input signal with a weight that is set to zero when the output of the envelope detector at a transform bin exceeds a predetermined level. Fig. 3 illustrates the concept of transform-domain notch filtering. Adaptive algorithms, such as LMS and RLS, can be used to determine the excision weights adaptively. The application of these algorithms, however, requires a reference signal that is correlated with the DS/SS signal.

When the binary weights are used, the transform-domain processing technique may suffer from the interference sidelobes. With block transforms, the energy in the narrowband

interference, which initially occupies a small region of the frequency spectrum, is dispersed in a relatively large spectral region. In this case, excision of a large frequency band may become necessary to effectively remove the interference power from most transform bins. The frequency dispersion of the interference can be nearly eliminated by weighting the received signal in the time domain with a nonrectangular weighting function prior to evaluating the transform. In doing so, the levels of the side lobes of the interference frequency spectrum are attenuated at the expense of broadening the main lobe [19], [15]. In this case, the conventional matched filter is no longer optimal. Using adapted demodulation accordingly can improve the receiver performance [20].

It is important to point out that for transform-domain processing, symbol detection can be performed in either the time or the transform domain. In the later case, filtering and correlation operations can be combined in one step.

The BER expression for transform-domain interference excision can be easily formulated using the Gaussian tail probability or the Q-function. The residual filtered and despreaded interference is treated as an equivalent AWGN source. Typically, a uniform interference phase distribution is assumed. When transform-domain filtering is considered, the BER depends on both the excision coefficients and the error misadjustment.

B. Synthesis/Subtraction for Sinusoidal Interference

In this section, we view the interference signal as the one that is corrupted by the additive noise and the DS/SS signal.

Eigenanalysis Approaches

In a typical situation, the power level of the DS/SS signal is negligible relative to the power level of the interference and, in the most case, relative to the additive noise. For high interference-to-noise ratio (INR), the correlation matrix of the received signal vector consists of a limited number of large eigenvalues contributed mainly by the narrowband interference, and a large number of small and almost equal eigenvalues contributed by the DS/SS signal and noise. The eigenanalysis interference canceller is designed with a weight vector orthogonal to the eigenvectors corresponding to the large eigenvalues [21].

The eigendecomposition of the correlation matrix, defined in (9), results in

$$R = U\Sigma U^H = [U_r U_n] \begin{bmatrix} \Sigma_r & 0 \\ 0 & \Sigma_n \end{bmatrix} \begin{bmatrix} U_r^H \\ U_n^H \end{bmatrix}, \qquad (24)$$

where the columns of U_r span the interference subspace, whereas the columns of U_n span the signal with noise subspace, and Σ_r and Σ_n are diagonal matrices whose elements are the eigenvalues of R. For real sinusoidal interference, the number of dimensions of the interference subspace is twice the number of interfering tones.

The projection of the signal vector on the noise subspace results in interference suppressed data sequence,

$$\hat{x}[n] = U_n U_n^H x[n] = \left(I - U_r U_r^H\right) x[n], \qquad (25)$$

where I is the identity matrix.

The subspace projection approach can also be performed using the singular value decomposition (SVD) for the sample data matrix [22].

C. Nonlinear Estimation Techniques

The commonly applied predictor/subtracter technique for narrowband interference suppression previously discussed is optimum in the minimum mean square error (MMSE) sense when trying to predict a Gaussian autoregressive process in the presence of AWGN. If the prediction is done in a non-Gaussian environment, as in the case of SS signals, linear prediction methods will no longer be optimum. In [3], depending on whether the statistics of the AR process is known or unknown, time-recursive and data-adaptive nonlinear filters with soft decision feedback are used to estimate the SS signal. For known interference statistics, the interference suppression problem is cast in state space for use with Kalman-Bucy and approximate conditional mean (ACM) filters. A fixed length LMS transversal filter, on the other hand, is used when there is no *a priori* statistical information is provided. With the same AR model, both schemes are shown to achieve similar performance, which is an improvement over the Gaussian assumed environment.

D. Multiuser Detection Techniques

A narrowband interference could be a digital communication signal with a data rate much lower than the spread spectrum chip rate. This is typically the case when spread

spectrum signals are used in services overlaying on existing frequency band occupants. In this case, the narrowband interference is a strong communication signal that interferes with commercial DS/SS communication systems. This type of interferers is poorly modeled as either a sinusoid or an autoregressive process. Because of the similarity of the spread spectrum signal and the digital interference, techniques from multi-user detection theory are applied to decode the SS user signal and simultaneously suppressing the interferer [23].

In order to apply methods from multiuser detection, the single narrowband interferer is treated as a collection of m spread spectrum users, where m is a function of the relative data rates of the true SS signal and the interference. That is, m bits of the narrowband user occur for each bit of the SS user. As shown in Fig. 4, and using square waves for illustrations, each narrowband user's bit can be thought as a signal arising from a virtual user having a signature sequence with only one non-zero entry. The virtual users are orthogonal, but correlated with the SS user.

The optimum receiver implementing the maximum likelihood (ML) detector has a complexity that is exponential in the number of virtual users, m. To overcome such complexity, the optimal linear detector and decorrelating detector are applied. While the first requires knowledge of relative energies of both the narrowband interferer and the SS user and maximizes the receiver asymptotic efficiency, the latter is independent of the receiver energies and achieves the near-far resistance of the ML detector. The asymptotic efficiency is the limit of the receiver efficiency as the AWGN goes to zero. It characterizes the detector performance when the dominant source of corruption is the narrowband interferer rather than the AWGN. The receiver efficiency, on the other hand, quantifies the SS user energy that would achieve the same probability of error in a system with the same AWGN and no other users. The input of both detectors is the output of the filter bank and consists of filters matched to the spreading codes of each active user, as depicted in Fig. 5.

The following expressions are derived in reference [23] for the probability of errors of four different detectors. In all cases, it is assumed that the narrowband signal is synchronized with the SS signal.

Conventional Detector (CD), where the received signal is sent directly to a single filter matched to the spreading code. The output of the filter is then compared to a threshold

to yield the spread spectrum bit estimate. This detector is only optimum in the case of a single spread spectrum user in AWGN. The BER is given by

$$P_{cd} = \frac{1}{2^m} \sum_{i=0}^{2^m-1} Q \left(\frac{\sqrt{w_2} \left(1 - \alpha \mathbf{p}^T \mathbf{q}^i \right)}{\sigma_n} \right) \tag{26}$$

where $\alpha = \sqrt{w_1/w_2}$, w_1 is the received energy of the narrowband interference, w_2 is the received energy of the SS user (including the process gain), $\mathbf{p}$ is the vector formed by the cross correlation between the narrowband interference waveform and the DS/SS signal waveform, $\mathbf{q}$ is the narrowband interference data bits, and $\{\mathbf{q}^i\}$ is an ordering of the 2^m possible values of the vector of narrowband bits.

Decorrelating Detector (DD), where the last row of the inverse of the cross-correlation matrix of the $m+1$ users is used to multiply the output of the $m+1$ matched filters, followed by a threshold comparison for bit estimate. The BER is given by

$$P_{dd} = Q \left(\frac{\sqrt{w_2 \left(1 - \mathbf{p}^T \mathbf{p} \right)}}{\sigma_n} \right). \tag{27}$$

Optimum Linear Detector (OLD), where the user energies are used to maximize the asymptotic efficiency. The BER is given by

$$P_{old} = \frac{1}{2^m} \sum_{i=0}^{2^m-1} Q \left(\frac{\sqrt{w_2} \left(1 + \alpha \mathbf{v}^T \mathbf{p} - \alpha(\alpha \mathbf{v}^T + \mathbf{p}^T) \mathbf{q}^i \right)}{\sigma_n \sqrt{1 + 2\alpha \mathbf{v}^T \mathbf{p} + \alpha^2 \mathbf{v}^T \mathbf{v}}} \right) \tag{28}$$

where the ith element of vector $\mathbf{v}$ is given by

$$v_i = \begin{cases} 1 & -\rho_i > \alpha \\ -1 & \rho_i > \alpha \\ -\rho_i/\alpha & \text{otherwise.} \end{cases} \tag{29}$$

Ideal Predictor/Subtracter (IPS), which is similar to the transversal filter excision techniques described in Section III-A. Perfect knowledge of the narrowband signal is assumed. Further, it is assume that perfect prediction to the sample interior to the narrowband bit is achieved and the only error occurs when predicting at bit transitions. The expressions were derived in [23], where one detector assumes zero bit estimate of the narrowband bit at the transition and the other detector takes this estimate to be random. For the former

detector,

$$P_{\text{ips}} = \frac{1}{2^m} \sum_{i=0}^{2^m-1} Q\left(\frac{\sqrt{w_2}\left(1 - \alpha \tilde{\mathbf{p}}^T \mathbf{q}^i\right)}{\sigma_n}\right),$$ (30)

and for the other detector

$$P_{\text{ips}} = \frac{1}{2^m} \sum_{i=0}^{2^m-1} \frac{1}{2^m} \sum_{j=0}^{2^m-1} Q\left(\frac{\sqrt{w_2}\left(1 - \alpha \tilde{\mathbf{p}}^T(\mathbf{q}^i - \hat{\mathbf{q}}^j)\right)}{\sigma_n}\right).$$ (31)

where $\hat{\mathbf{q}}^j$ is the estimate of $\mathbf{q}^j$, and $\tilde{\mathbf{p}}$, defined only over the chip interval emcompassing a narrowband bit transition, is the vector formed by the cross correlation between the narrowband interference and the DS/SS signal.

The performance of the optimum linear and decorrelator detectors, representing the multi-user detection techniques, is shown in reference [23] to be similar for different interference power and bandwidth. Both techniques significantly outperform the conventional detector and the predictor/subtracter, when using a 7 tap LMS prediction filter. The improvement in BER is more pronounced for stronger and less narrowband interferers. The advantage of the decorrelator detector over the other conventional and adaptive prediction filters remains unchanged when considering asynchronous interference.

Fig. 6 depicts the BER comparison between the conventional detector, decorrelating detector, optimum linear detector, and ideal predictor/subtracter with $m=2$ and $L = 63$. This figure is in agreement with the performance figures, shown in [23], and conforms with the same observations stated above. It is clear from Fig. 6 that the matched filter performs well for weak interferers. The optimum linear detector offers slight improvement over the decorrelating detector. The ideal predictor/subtracter outperforms the decorrelating detector for moderate values of interference power. It is important to note, however, that the actual predictor/subtracter performance will have much greater error probability [23].

E. Minimum Mean-Square Error Algorithm

The minimum mean-square error (MMSE) algorithm, originally proposed for suppressing multiple-access interference in DS/CDMA multi-user detection problems, has been employed for narrowband interference mitigation [24]. Using the signal-to-interference ratio and its upper bounds as a performance measure, the MMSE has been compared with

linear and nonlinear techniques in suppressing three types of interference, namely single-tone and multi-tone signals, autoregressive process, and digital communications signal with a data rate much lower than the spread spectrum chip rate. The linear estimators include the conventional matched filter detector, the predictor/subtracter, and the interpolator/subtracter techniques. The latter is based on using a fixed number of past and future samples [24]. The nonlinear techniques include those based on prediction and interpolation. It is shown that the MMSE detector completely suppresses the digital interference, irrespective of its power, and provides similar performance to the nonlinear interpolator/subtracter method, when dealing with AR type of interference.

IV. Nonstationary Interference Suppression

The interference excision techniques discussed in the previous sections deal with stationary or quasi-stationary environment. The interference frequency signature, or characteristics, is assumed fixed or slowly time-varying. None of these techniques is capable of effectively incorporating the suddenly changing or evolutionary rapidly time-varying nature of the frequency characteristics of the interference. These techniques all suffer from their lack of intelligence about interference behavior in the joint time-frequency (t-f) domain and therefore are limited in their results and their applicability. For the time-varying interference depicted in Fig. 7, frequency-domain methods remove the frequency band Δf and ignore the fact that only few frequency bins are contaminated by the interference at a given time. Dually, time domain excision techniques, through gating or clipping the interference over Δt, do not account for the cases where only few time samples are contaminated by the interference for a given frequency. Applying either method will indeed eliminate the interference but at the cost of unnecessarily reducing the desired signal energy. Adaptive excision methods might be able to track and remove the nonstationary interference, but would fail if the interference is highly nonlinear FM or linear FM, as in Fig. 7, with high sweep rates. Further, the adaptive filtering length or block transform length trades off the temporal and the spectral resolutions of the interference. Increasing the step size parameter increases the filter output errors at convergence, and causes an unstable estimate of the interference waveform.

The above example clearly demonstrates that nonstationary interferers, which have

model parameters that rapidly change with time, are particularly troublesome due to the inability of single-domain mitigation algorithms to adequately ameliorate their effects. In this challenging situation, and others like it, joint t-f techniques can provide significant performance gains, since the instantaneous frequency (IF), the instantaneous bandwidth, and the energy measurement, in addition to myriad other parameters, are available. The objective is then to estimate the t-f signature of the received data using t-f analysis, attenuating the received signal in those t-f regions that contain strong interference. This is depicted by the region in between the dashed lines in Fig. 7.

An FM interference in the form $u(n) = e^{j\phi(n)}$ is solely characterized by its IF, which can be estimated using a variety of IF estimators, including the time-frequency distributions (TFDs) [25], [26].

The TFD of the data, $x(n)$, at time t and radian frequency ω, is given by

$$C_f(t,\omega,\phi) = \sum_{l=-\infty}^{\infty} \sum_{m=-\infty}^{\infty} \phi(m,l)x(n+m+l)x^*(x+m-l)e^{-j2\omega l} \qquad (32)$$

where $\phi(m,l)$ is the time-frequency kernel which is a function of the lag l and time-lag m. Several requirements have been imposed on $\phi(m,l)$ to satisfy desirable distribution properties, including power localization at the IF. As shown in eqn. (32), the TFD is the Fourier transform of a time-average estimate of the autocorrelation function.

A time-frequency notch filter can be designed, in which the position of the filter notch is synchronous with the interference IF estimate. Based on the IF, two constraints should exist to construct an interference excision filter with desirable characteristics. First, an FIR filter with short impulse response must be used. Long extent filters are likely to span segments of changing frequency contents and, as such, allow some of the interference components to escape to the filter output. Second, at any given time, the filter frequency response must be close to an ideal notch filter to be able to null the interference with minimum possible distortion of the signal. This property, however, requires filters with infinite or relatively long impulse responses.

Amin [27] has shown that a linear-phase five-coefficient filter is effective in FM interference excision. Assuming exact IF values, the corresponding receiver SINR is given

by

$$\text{SINR} = \frac{L}{11/8 + 9\sigma_n^2/4}. \tag{33}$$

The above expression shows that full interference excision comes at the expense of a change in the noise variance in addition of a self-noise form, as compared with the non-interference case. The main objective of any excision process is to reduce both effects. The SINR in (33) assumes a random IF with uniform distribution over $[0, 2\pi]$. For an interference with fixed frequency ω_0, the receiver SINR becomes dependent on ω_0. The receiver performance sensitivity to the interference frequency is discussed in detail in [27].

Wang and Amin [28] considered the performance analysis of the IF-based excision system using a general class of multiple-zero FIR excision filters showing the dependence of the BER on the filter order and its group delay. The effect of inaccuracies in the interference IF on receiver performance was also considered as a function of the filter notch bandwidth. Closed form approximations for SINR at the receiver are given for the various cases.

One of the drawbacks to the notch filter approach in [27] is the infinite notch depth due to the placement of the filter zeros. The effect is a "self-noise" inflicted on the received signal by the action of the filter on the PN sequence underlying the spread information signal. This problem led to the design of an open-loop filter with adjustable notch depth based on the interference energy. The notch depth is determined by a variable embedded in the filter coefficients chosen as the solution to an optimization problem which maximizes receiver SINR. The TFD is necessary for this work, even for single component signals, because simple IF estimators do not provide energy information. Amin, Wang, and Lindsey accomplished this work in [29], incorporating a "depth factor" into the analysis and re-developing all the SINR calculations. The result was a significant improvement in SINR, especially at mid-range interference-to-signal ratios (ISR's), typically around 0 to 20 dB.

Instead of using time-varying excision filters, Barbarossa and Scaglione [30] proposed a two-step procedure based on dechirping techniques commonly applied in radar algorithms. In the first step the time varying interference is converted to a fixed frequency sinusoid eliminated by time invariant filters. The process is reversed. In the second step and the interference-free signal is multiplied by the interference t-f signature to restore the DS/SS signal and noise characteristics which have been strongly impacted in the first phase.

Similar to predictor/subtracter method discussed in Section III, Lach, Amin, and Lindsey proposed synthesis/subtracter technique for FM interference using TFD [31]. A replica of the interference can be synthesized from the t-f domain and subtracted from the incoming signal to produce an essentially interference-free channel.

Another synthesis/subtracter method is introduced in [32] where the discrete evolutionary and the Hough transforms are used to estimate the IF. The interference amplitude is found by conventional methods such as linear filtering or singular value decomposition. This excision technique applies equally well to one or multi-component chirp-interferers with constant or time-varying amplitudes and with instantaneous frequencies not necessarily parametrically modeled.

To overcome the drawbacks of the potential amplitude and phase errors produced by the synthesis methods, Amin, Ramineni and Lindsey [33] proposed a projection filter approach in which the FM interference subspace is constructed from its t-f signature. Since the signal space at the receiver is not specifically mandated, it can be rotated such that a single interferer becomes one of the basis functions. In this way, the interference subspace is one dimensional and its orthogonal subspace is interference-free. A projection of the received signal onto the orthogonal subspace accomplishes interference excision with a minimal message degradation. The projection filtering methods compare favorably over the previous notch filtering systems.

In [34], Zhang, Amin, and Lindsey proposed a method to suppress more general INBI signals. The interference subspace is constructed using t-f synthesis methods. In different to the work in [31], the interferer is removed by projection rather than subtraction. To estimate the interference waveform, a mask is constructed and applied such that the masked t-f region captures the interference energy, but leaves out most of the DS/SS signals.

Seong and Loughlin have also extended the projection method developed by Amin *et. al.* [33] for excising constant amplitude FM interferers from DS/SS signals to the case of AM-FM interferers [35]. Theoretical performance results (correlator SNR and BER) for the AM-FM projector filter show that FM estimation errors generally cause greater performance degradation than the same level of error in estimating the AM. The lower-

bound for the correlator SINR for the AM-FM projection filter for the case of both AM and FM errors is given by

$$\text{SINR} = \frac{L-1}{\frac{1}{L} + \sigma_n^2 + A^2 \left[\frac{1}{1 + \sigma_{\Delta a}^2} \left(1 - e^{-\sigma_{\Delta \phi}^2} \right) + \sigma_{\Delta a}^2 \right]}, \tag{34}$$

where L is the PN sequence length, A^2 is the interference power, σ_n^2 is the variance of AWGN, and $\sigma_{\Delta a}^2$ and $\sigma_{\Delta \phi}^2$ are the variances of the estimation errors in the AM and FM, respectively.

Linear t-f signal analysis has also been shown effective to characterize a large class of nonstationary interferers. Roberts and Amin [36] proposed the use of the discrete Gabor transform (DGT) as a linear joint time-frequency representation. The DGT can attenuate a large class of nonstationary wideband interferers whose spectra are localized in the t-f domain. Compared to bilinear TFDs, the DGT does not suffer from the crossterm interference problems, and enjoys a low computational complexity. In [37], Wei, Harding, and Bovik devised a DGT-based, iterative time-varying excision filtering, in which a hypothesis testing approach was used to design a binary mask in the DGT domain. The time-frequency geometric shape of the mask is adapted to the time-varying spectrum of the interference. They show that such a statistical framework for the transform-domain mask design can be extended to any linear transform. Both the maximum likelihood test and the local optimal test are presented to demonstrate performance versus complexity.

The application of the short-time Fourier transform (STFT) to nonstationary interference excision in DS/SS communications is considered in [38], [39]. In both papers, due to the inherent property of STFT to trade off temporal and spectral resolutions, several STFTs corresponding to different analysis windows were generated. In [38], Ouyang and Amin used a multiple-pole data window to obtain a large class of recursive STFTs. Subsequently, they employed concentration measures to select the STFT that localizes the interference in the t-f domain. This procedure is followed by applying a binary excision mask to remove the high-power t-f region. The remainder is synthesized to yield a DS/SS signal with improved signal-to-interference ratio (SIR).

In [39], Krongold *et. al* proposed multiple overdetermined tiling techniques and utilized a collection of STFTs for the purpose of interference excision. Unlike the procedure in [38],

the authors in [39] removed the high-value coefficients in all generated STFTs, and used the combined results, via efficient least-square synthesis, to reconstruct an interference-reduced signal. Bultan and Akansu [40] proposed a chirplet-transform-based exciser to handle chirp-like interference types in SS communications.

The block diagram in Fig. 8 depicts the various interference rejection techniques using the time-frequency methods cited above.

A. Example

At this point, in order to further illustrate these excision methods, the work in [33] will be detailed since it includes comparisons between the two most prominent techniques based on TFDs currently being studied — notch filtering and projection filtering. The signal model is, as expected, given by (1), and the major theme of the work is to annihilate interference via projection of the received signal onto an "interference-free" subspace generated from the estimated interference characteristics. This paper includes a figure, reprinted here as Fig. 9, which clearly illustrates the trade-offs between projection and notch filtering based on the ISR. In the legend, the variable a represents the adaptation parameter for the notch filtering scheme and N represents the block size, in samples, for a 128 sample bit duration in the projection method. Thus, $N = 128$ means no block processing and $N = 2$ corresponds to 64 blocks per bit being processed for projection. Since the projection and non-adaptive notch filter techniques are assumed to completely annihilate the interference, their performance is decoupled from the interference power, and therefore correctly indicate constant SINR across the graph. The dashed line representing the notch filter with $a = 0$ is really indicating no filtering at all, since the adaptation parameter controls the depth of the notch.

It is evident from Fig. 9 that without adaptation a crossover point occurs around 2 dB where filtering with an infinitely deep notch is advantageous. Thus when the interference power exceeds this point, presumably a user would flip a switch to turn on the excision subsystem. However, with adaptation, this process happens automatically, while giving superior performance in the midrange. For the projection technique, the block size determines receiver performance conspicuously (ceteris paribus). Most important to note, however, is the superior performance of projection over all methods when the block size

is equal to the bit duration, i.e. no block processing. It is feasible that computational complexity may warrant a trade-off between SINR and block size, in which case a hybrid implementation may be of benefit — one that automatically switches between adaptive notch filtering and projection depending on the desired SINR. In any case, this example illustrates the parameters involved in the design of modern excision filters for nonstationary interferers.

V. Interference Suppression for Frequency Hopping Communications

Interference rejection for FH is not as well developed as interference rejection for DS or for CDMA. In FH systems, the fast FH (FFH) is of most interest, and the modulation most commonly used in FH is frequency-shift keying (FSK). Two types of interference waveforms can be categorized, namely, partial-band interference (PBI) and multitone interference (MTI).

The effects of PBI and AWGN on several diversity-combining receivers in FFH/FSK SS communication systems have been investigated in [41], [42], [43], [45]. In [46], an alternative method using a fast Fourier transform (FFT) is proposed. In [41] the authors present an automatic gain-control (AGC) receiver using a diversity technique. In this method, each soft-decision square-law detected MARK and SPACE filter output is weighted by the inverse of the noise power in the slot prior to linear combining. This method is near-optimal (in terms of SNR) if the exact information of noise and interference power can be obtained. A similar clipped-linear combining receiver was also reported in [43]. Due to the difficulty of such information, self-normalizing receivers [42] and the ratio-statistic combining technique [44] use the output values of the square-law detector in each hop to derive a weight or normalizing factor. The performance of these two methods is shown to be comparable to that of the square-law clipper receiver.

In [45] the authors describe an FFH receiver that employs a prewhitening filter to reject NBI. For binary FSK modulations, it is shown that the FFH signal is statistically uncorrelated at lag values of $T_h/(4N_h)$ where T_h is the hop duration and $2N_h$ is the total number of frequency slots (i.e., there are N_h MARK and N_h SPACE's). Thus, as in the DS case, NBI can be predicted and suppressed independently of the desired FFH signal. Using the complex LMS algorithm to update the prewhitening filter coefficients, this technique is

114

shown to compare favorably with the maximal-ratio combiner diversity technique. When the interferer is wide-sense stationary, the prewhitening filter based receiver provides performance approaching that of the AGC receiver and at least 2 – 3 dB superior to that of the self-normalizing receiver. However, when hostile interference is present, the adaptive prewhitening filter technique may not be able to track the interference rapidly enough. In this case, nonparametric techniques such as the self-normalizing receiver must be used to reject the jammed hops.

Reed and Agee [47] have extended and improved on the idea of whitening by using a time-dependent filter structure to estimate and remove interference, based on the interference spectral correlation properties. In this method, the detection of FH/SS in the presence of spectrally correlated interference is nearly independent of the SIR. The process can be viewed as a time-dependent whitening process with suppression of signals that exhibit a particular spectral correlation. The technique is developed from the maximum-likelihood estimate of the spectral frequency of a frequency agile signal received in complex Gaussian interference with unknown spectral correlation. The resulting algorithm uses the correlation between spectrally separated interference components to reduce the interference content in each spectral bin prior to the whitening/detection operation.

In [46], an alternative approach to suppress PBI using the FFT is proposed. The major attraction of FFT-based implementation lies in the ability to achieve guaranteed accuracy and perfect reproducibility.

For suppression of MTI, basically the same processing methods applied for PBI can be employed. However, the performance analyses differ from those for PBI situations. The performance depends on the distribution of the MTI and, in turn, how many bands are contaminated by MTI. Performance analyses of FFH SS systems are presented in [48], [49] for linear combining diversity, in [50] clipped diversity, in [51], [52] for maximum likelihood and product-combining receivers.

References

[1] M. Amin and A. Lindsey, "Time-frequency for interference mitigation in spread spectrum communication systems," CRC, B. Boashash (ed.), Prentice-Hall, Spring 2002.

[2] L. B. Milstein, "Interference rejection techniques in spread spectrum communications," *Proc. IEEE*, vol. 76, no. 6, pp. 657–671, June 1988.

[3] H. V. Poor and L. A. Rusch, "Narrowband interference suppression in spread-spectrum CDMA," *IEEE Personal Comm. Mag.*, vol. 1, no. 8, pp. 14–27, Aug. 1994.

[4] J. D. Laster and J. H. Reed, "Interference rejection in digital wireless communications," *IEEE Signal Processing Mag.*, vol. 14, no. 3, pp. 37–62, May 1997.

[5] M. G. Amin and A. N. Akansu, "Time-frequency for interference excision in spread-spectrum communications," section in "Highlights of signal processing for communications," G. Giannakis, editor, *IEEE Signal Processing Mag.*, vol. 15, no. 5, Sep. 1998.

[6] F. M. Hsu and A. A. Giordano, "Digital whitening techniques for improving spread-spectrum communications performance in the presence of narrow-band jamming and interference," *IEEE Trans. Commun.*, vol. COM-26, pp. 209–216, Feb. 1978.

[7] J. W. Ketchum and J. G. Proakis, "Adaptive algorithms for estimating and suppressing narrow-band interference in PN spread-spectrum systems," *IEEE Trans. Commun.*, vol. COM-30, pp. 913–924, May 1982.

[8] L. Li and L. B. Milstein, "Rejection of narrow-band interference in PN spread-spectrum system using transversal filters," *IEEE Trans. Commun.*, vol. COM-30, pp. 925–928, May 1982.

[9] R. A. Iltis and L. B. Milstein, "Performance analysis of narrow-band interference rejection techniques in DS spread-spectrum systems," *IEEE Trans. Commun.*, vol. COM-32, pp. 1169–1177, Nov. 1984.

[10] S. Haykin, *Adaptive Filter Theory*, 3rd ed. Englewood Cliffs, NJ: Prentice Hall, 1996.

[11] R. A. Iltis and L. B. Milstein, "An approximate statistical analysis of the Widrow LMS algorithm with application to narrow-band interference rejection," *IEEE Trans. Commun.*, vol. COM-33, pp. 121–130, Feb. 1985.

[12] F. Takawira and L. B. Milstein, "Narrowband interference rejection in PN spread spectrum system using decision feedback filters," in *Proc. MILCOM*, pp. 20.4.1–20.4.5, Oct. 1986.

[13] J. G. Proakis, *Digital Communications*, 3rd ed. New York, NY: McGraw-Hill, 1995.

[14] L. B. Milstein and P. K. Das, "Spread spectrum receiver using surface acoustic wave technology," *IEEE Trans. Commun.*, vol. COM-25, pp. 841–847, Aug. 1977.

[15] S. Davidovici and E. G. Kanterakis, "Narrowbnd interference rejection using real-time Fourier transform," *IEEE Trans. Commun.*, vol. 37, pp. 713–722, July 1989.

[16] R. C. Dipietro, "An FFT based technique for suppressing narrow-band interference in PN spread spectrum communication systems," in *Proc. IEEE Int. Conf. Acoust., Speech, Signal Proc.*, pp. 1360–1363, 1989.

[17] M. V. Tazebay and A. N. Akansu, "Adaptive subband transforms in time-frequency excisers for DSSS communication systems," *IEEE Trans. Signal Processing*, vol. 43, pp. 1776–1782, Nov. 1995.

[18] M. Medley, G. J. Saulnier, and P. Das, "Adaptive subband filtering of narrowband interference," H. Szu, Ed., *SPIE Proc. — Wavelet Appls. III*, vol. 2762, April 1996.

[19] J. Gevargiz, M. Rosenmann, P. Das, and L. B. Milstein, "A coparison of weighted and non-weighted transform domain processing systems for narrowband interference excision," in *Proc. MILCOM*, pp. 32.3.1–32.3.4, 1984.

[20] S. D. Sandberg, "Adapted demodulation for spread-spectrum receivers which employ transform-domain interference excision," *IEEE Trans. Commun.*, vol. 43, pp. 2502–2510, Sept. 1995.

[21] A. Haimovich and A. Vadhri, "Rejection of narrowband interferences in PN spread spectrum systems using an eigenanalysis approach," in *Proc. IEEE Signal Processing Workshop on Statistical Signal and Array Processing*, Quebec, Canada, pp. 1002–1006, June 1994.

[22] B. K. Poh, T. S. Quek, C. M. S. See, and A. C. Kot, "Suppression of strong narrowband interference using eigen-structure-based algorithm," in *Proc. MILCOM*, pp. 1205–1208, July 1995.

[23] L. A. Rusch and H. V. Poor, "Multiuser detection techniques for narrow-band interference suppression in spread spectrum communications," *IEEE Trans. Commun.*, vol. 43, pp. 1725–1737, Feb./Mar./Apr. 1995.

[24] H. V. Poor and X. Wang, "Code-aided interference suppression for DS/CDMA communications. I. Interference suppression capability," *IEEE Trans. Commun.*, vol. 45, pp. 1101–1111, Sept. 1997.

[25] B. Boashash, "Estimating and interpreting the instantaneous frequency of a signal. I. Fundamentals," *Proc. IEEE*, vol. 80, pp. 520–538, Apr. 1992.

[26] B. Boashash, "Estimating and interpreting the instantaneous frequency of a signal. II. Algorithms and applications," *Proc. IEEE*, vol. 80, pp. 540–568, Apr. 1992.

[27] M. G. Amin, "Interference Mitigation in Spread-Spectrum Communication Systems Using Time-Frequency Distributions," *IEEE Trans. Signal Processing*, vol. 45, no. 1, pp. 90-102, Jan. 1997.

[28] C. Wang and M. G. Amin, "Performance analysis of instantaneous frequency based interference excision techniques in spread spectrum communications," *IEEE Trans. Signal Processing*, vol. 46, no. 1 pp. 70-83, Jan. 1998.

[29] M. G. Amin, C. Wang, and A. R. Lindsey, "Optimum Interference Excision in Spread-Spectrum Communications Using Open-Loop Adaptive Filters," *IEEE Trans. Signal Processing*, July 1999.

[30] S. Barbarossa and A. Scaglione, "Adaptive time-varying cancellations of wideband interferences in spread-spectrum communications based on time-frequency distributions," *IEEE Trans. Signal Processing*, vol. 47, no. 4, pp. 957-965, April 1999.

[31] S. Lach, M. G. Amin, and A. R. Lindsey, "Broadband nonstationary interference excision in spread-spectrum communications using time-frequency synthesis techniques," *IEEE J. Select. Areas Commun.*, vol. 17, no. 4, pp. 704-714, April 1999.

[32] H. A. Khan and L. F. Chaparro, "Formulation and implementation of the non-stationary evolutionary

Wiener filtering," *Signal Processing*, vol. 76, pp. 253-267, 1999.

[33] M. G. Amin, R. S. Ramineni, A. R. Lindsey, "Interference excision in DSSS communication systems using projection techniques," in *Proc. IEEE Int. Conf. Acoust., Speech, Signal Process.*, Istanbul, Turkey, June 2000.

[34] Y. Zhang, M. G. Amin, and A. R. Lindsey, "Combined Synthesis and Projection Techniques for Jammer Suppression in DS/SS Communications," *IEEE Int. Conf. Acoust., Speech, Signal Process.*, Orlando, FL, May 2002.

[35] S.-C. Jang and P. J. Loughlin, "AM-FM interference excision in spread spectrum communications via projection filtering," *J. Applied Signal Processing*, 2001.

[36] S. Roberts and M. Amin, "Linear vs. bilinear time-frequency methods for interference mitigation in direct-sequence spread-spectrum communication systems," *Proc. Asilomar Conf. Signals, Systems, and Computers*, Pacific Grove, CA, Nov. 1995.

[37] D. Wei, D. S. Harding, and A. C. Bovik, "Interference rejection in direct-sequence spread-spectrum communications using the discrete Gabor transform," *Proc. IEEE Digital Signal Processing Workshop*, Bryce Canyon, UT, Aug. 1998.

[38] X. Ouyang, M. G. Amin, "Short-time Fourier transform receiver for nonstationary interference excision in direct sequence spread spectrum communications," *IEEE Trans. Signal Processing*, vol. 49, no. 4, pp. 851–863, April 2001.

[39] B. S. Krongold, M. L. Kramer, K. Ramchandran, and D. L. Jones, "Spread-spectrum interference suppression using adaptive time-frequency tilings," *Proc. IEEE Int. Conf. Acoust. Speech, Signal Process.*, Munich, Germany, April 1997.

[40] A. Bultan and A. N. Akansu, "A novel time-frequency exciser in spread-spectrum communications for chirp-like interference," *Proc. IEEE Int. Conf. Acoust. Speech, Signal Process.*, Seattle, WA, May 1998.

[41] J. S. Lee, L. E. Miller, and Y. K. Kim, "Probability of error analysis of a BFSK frequency-hopping system with diversity – Part II," *IEEE Trans. Commun.*, vol. COM-32, pp. 1243–1250, Dec. 1984.

[42] L. E. Miller, J. S. Lee, and A. P. Kadrichu, "Probability of error analyses of a BPSK frequency-hopping system with diversity under partial-band jamming interference – Part III: Performance of a square-law self-normalizing soft decision receiver," *IEEE Trans. Commun.*, vol. COM-34, pp. 669-675, July 1986.

[43] C. M. Keller and M. B. Pursley, "Clipper diversity combining for channels with partial-band interference – Part I: Clipper linear combining," *IEEE Trans. Commun.*, vol. COM-35, pp. 1320–1328, Dec. 1987.

[44] C. M. Keller and M. B. Pursley, "Clipper diversity combining for channels with partial-band interference – Part II: Ratio-statistic combining," *IEEE Trans. Commun.*, vol. COM-37, pp. 145-151, Feb. 1989.

[45] R. A. Iltis, J. A. Ritcey, and L. B. Milstein, "Interference rejection in FFH systems using least squares

estimation techniques," *IEEE Trans. Commun.*, vol. 38, pp. 2174–2183, Dec. 1990.

[46] K. C. Teh, A. C. Kot, K. H. Li, "Partial-band jammer suppression in FFH spread-spectrum system using FFT," *IEEE Trans. Vehi. Tech.*, vol. 48, pp. 478–486, March 1999.

[47] J. H. Reed and B. Agee, "A technique for instantaneous tracking of frequency agile signals in the presence of spectrally correlated interference," *Proc. Asilomar Conf. Signals, Systems, and Computers*, Pacific Grove, CA, Nov. 1992.

[48] B, K. Livitt, "FH/MFSK performance in multitone jamming," *IEEE J. Select. Areas Commun.*, vol. SAC-3, pp. 627–643, Sept. 1985.

[49] R. E. Ezers, E. B. Felstead, T. A. Gulliver, and J. S. Wight, "An analytical method for linear combining with application to FFH NCFSK receivers," *IEEE J. Select. Areas Commun.*, vol. 11, pp. 454–464, Apr. 1993.

[50] J. J. Chang and L. S. Lee, "An exact performance analysis of the clipped diversity combining receiver for FH/MFSK systems against a band multitone jammer," *IEEE Trans. Commun.*, vol. 42, pp. 700–710, Feb./Mar./Apr. 1994.

[51] K. C. Teh, A. C. Kot, K. H. Li, "Performance study of a maximum-likelihood receiver for FFH/BFSK systems with multitone jamming," *IEEE Trans. Commun.*, vol. 47, pp. 766–772, May 1999.

[52] K. C. Teh, A. C. Kot, K. H. Li, "Performance analysis of an FFH/BFSK product-combining receiver under multitone jamming" *IEEE Trans. Vehi. Tech.*, vol. 48, pp. 1946–1953, Nov. 1999.
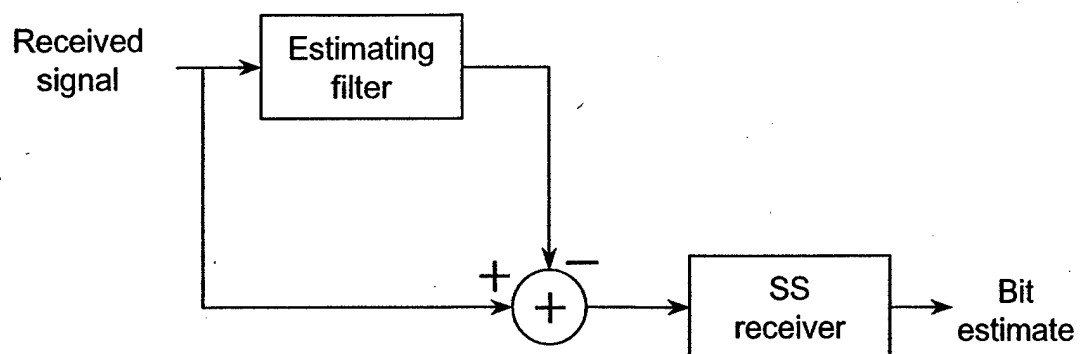
Fig. 1   Estimator/subtracter based interference suppression.
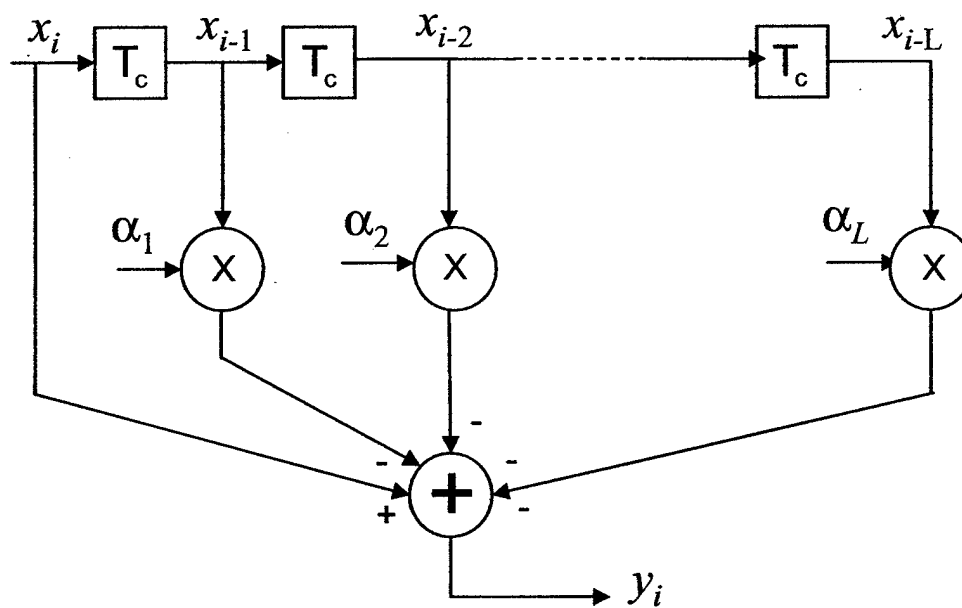
Fig. 2   Single-sided transversal filter.
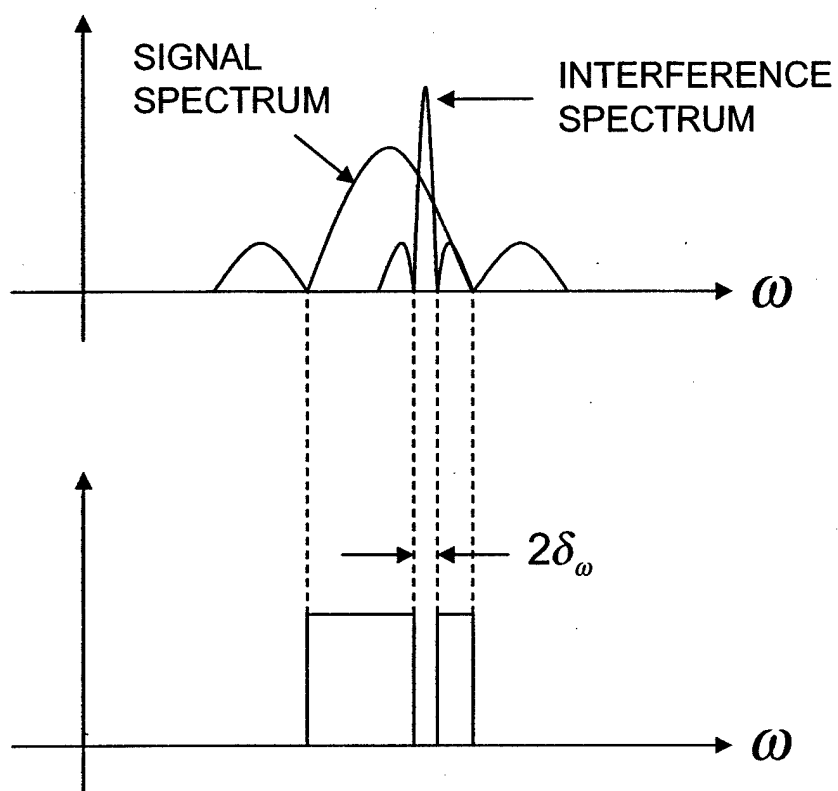
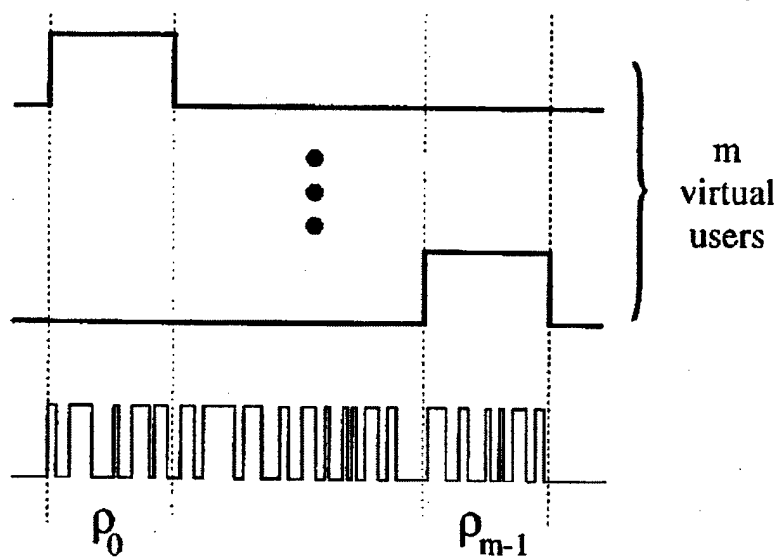Fig. 3   Transform-domain notch filtering.

Fig. 4   Virtual CDMA systems (synchronous case).
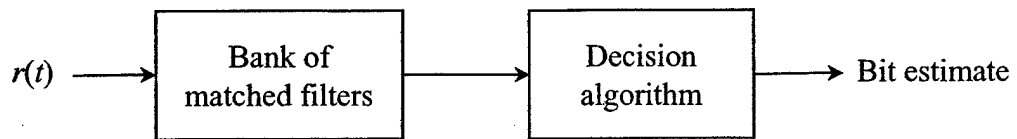
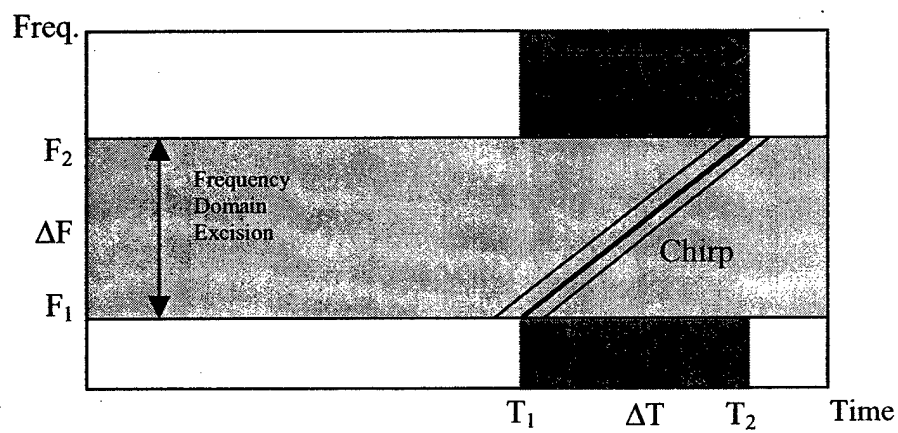Fig. 5   Multiuser detector structure.

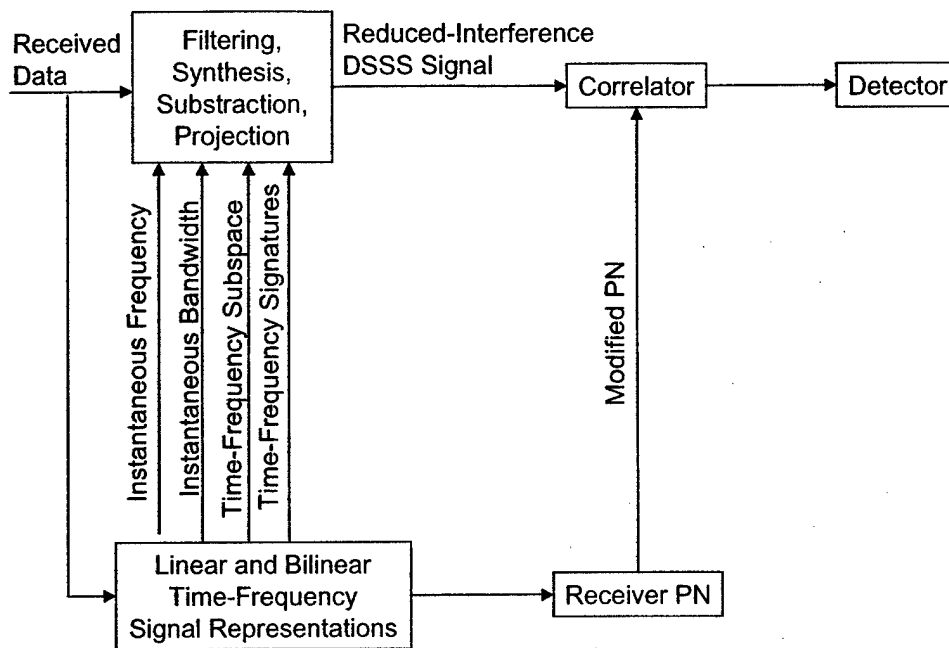Fig. 6   Excision methods for nonstationary interferers.
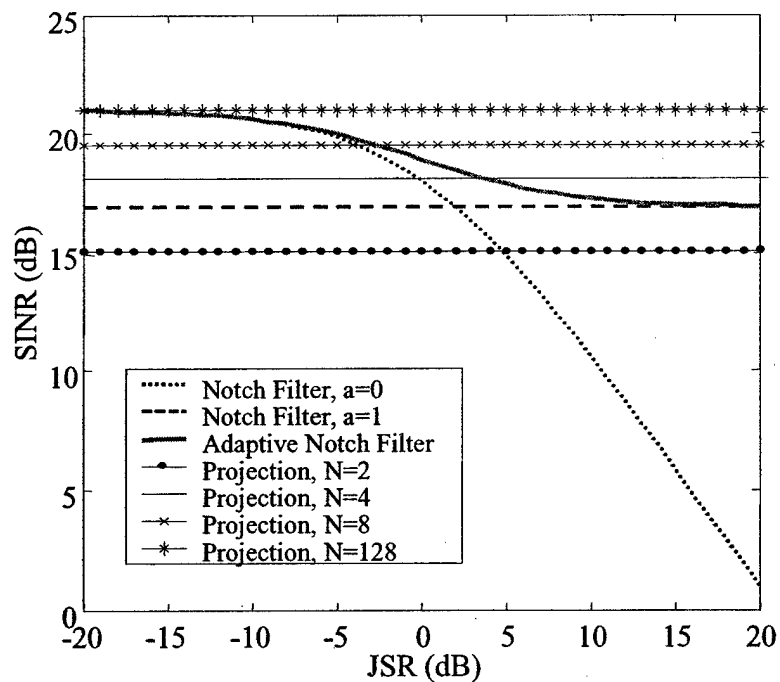
Fig.7   Interference rejection techniques

Fig. 8   Comparison between projection and notch filtering excision methods.

Spatial Time-Frequency Distributions

and Their Applications

Moeness G. Amin and Yimin Zhang

Department of Electrical and Computer Engineering, Villanova University, Villanova, PA 19085, USA

I. Spatial Time-Frequency Distributions

The evaluation of quadratic time-frequency distributions (TFDs) of nonstationary signals impinging on a multi-sensor receiver yields spatial time-frequency distributions (STFDs), which permit the application of eigenstructure subspace techniques to solving a large class of channel estimation and equalization, blind source separation (BSS), and high resolution direction-of-arrival (DOA) estimation problems [1], [2], [3]. STFD based techniques are appropriate to handle sources of nonstationary waveforms that are highly localized in the time-frequency (t-f) domain. In the area of BSS, the use of the STFDs allows the separation of sources with identical spectral shape, but with different t-f localization properties, i.e., different t-f signatures. For both source separation and DOA estimation problems, spreading the noise power while localizing the source energy in the t-f domain amounts to increasing the robustness of eigenstructure signal and noise subspace estimation methods with respect to channel and receiver noise. This in turn leads to an improvement of spatial resolution and source separation performance.

The quadratic class of STFD matrix of a signal vector $\mathbf{x}(t)$ is defined as

$$\mathbf{D_{xx}}(t, f) = \int_{-\infty}^{\infty} \int_{-\infty}^{\infty} \int_{-\infty}^{\infty} g(v, \tau) \mathbf{x}(u + \frac{\tau}{2}) \mathbf{x}^{H}(u - \frac{\tau}{2}) e^{j2\pi(vu - vt - f\tau)} d\tau \, du \, dv, \qquad (1)$$

where $g(v, \tau)$ is the kernel function.

In narrowband array processing, when n signals arrive at an m-element array (see Fig. I), the linear data model

$$\mathbf{x}(t) = \mathbf{y}(t) + \mathbf{n}(t) = \mathbf{A}\mathbf{d}(t) + \mathbf{n}(t) \qquad (2)$$

is commonly assumed, where $\mathbf{x}(t)$ is the $m \times 1$ data vector received at the array, $\mathbf{d}(t)$ is the $n \times 1$ source data vector, the $m \times n$ spatial matrix $\mathbf{A} = [\mathbf{a}_1 \cdots \mathbf{a}_n]$ represents the mixing matrix, $\mathbf{a}_i$ is the steering vector of ith signal, and $\mathbf{n}(t)$ is an additive noise vector whose elements are modeled as stationary, spatially and temporally white, zero-mean complex random processes, independent of the source signals.
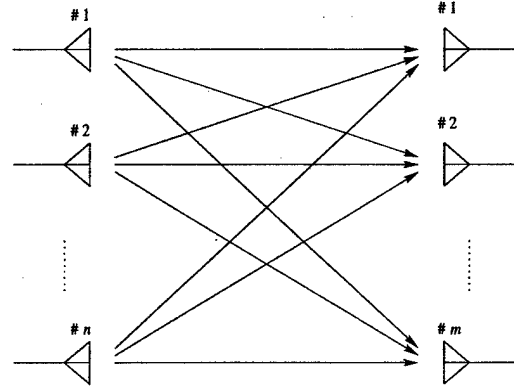
m-element array with n signal arrivals.

Under the uncorrelated signal and noise assumption and the zero-mean noise property, the expectation of the crossterm TFD matrices between the signal and noise vectors is zero, i.e., $E\left[\mathbf{D_{yn}}(t, f)\right] = E\left[\mathbf{D_{ny}}(t, f)\right] = \mathbf{0}$, and it follows

$$E\left[\mathbf{D_{xx}}(t, f)\right] = \mathbf{D_{yy}}(t, f) + E\left[\mathbf{D_{nn}}(t, f)\right] = \mathbf{A}\mathbf{D_{dd}}(t, f)\mathbf{A}^H + \sigma^2 \mathbf{I}, \qquad (3)$$

where σ^2 is the noise power, and $\mathbf{I}$ is the identity matrix. Equation (3) is similar to that which has been commonly used in array processing based on second-order statistics, relating the signal correlation matrix to the data spatial correlation matrix [1]. This implies that key problems in various applications of array processing, specifically those dealing with nonstationary signal environments, can be approached using quadratic transformations. If $\mathbf{D_{dd}}(t, f)$ is a full-rank matrix, the two subspaces spanned by the principal eigenvectors of $\mathbf{D_{xx}}(t, f)$ and the columns of $\mathbf{A}$ become identical. In this case, direction finding techniques based on eigenstructures can be applied. If $\mathbf{D_{dd}}(t, f)$ is diagonal, i.e., the signal cross-TFDs at the t-f point (t, f) are zeros, then both the mixing matrix and the signal waveforms can be recovered using BSS methods.

II. Fundamental Properties

There are five key advantages of array signal processing using STFD. In order to properly explain these advantages, we use the diagram in Fig. II. We consider two sources A and B incident on a multi-sensor array. Source A occupies the t-f region R_a, whereas source B occupies the t-f region R_b. The t-f signatures of the two sources overlap, but each source still has a t-f region that is not intruded over by the other source.
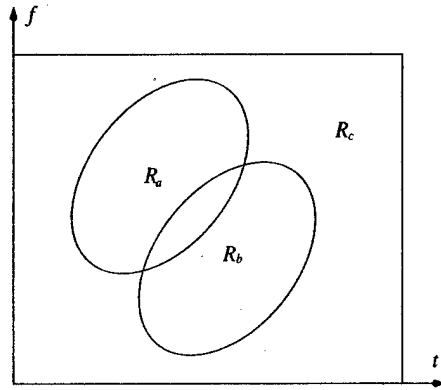
Signals with different time-frequency signature.

1) Equation (3) can be easily derived for any arbitrary joint-variables. Time and frequency are indeed the two most commonly used and physically understood parameters. However, by replacing the STFDs by spatial arbitrary joint-variable distributions, one can relate the sensor joint-variable distributions to the sources joint-variable distributions through the same mixing matrix **A**. As shown in the Examples Section, there are situations where it is preferable to consider other domains such as the ambiguity lag-Doppler domain, where the locations of the signals and their cross-terms are guided by properties and mechanisms different than those associated with the t-f domain.

2) Equation (3) is valid for all t-f points. It is well known that direction finding techniques require $\mathbf{D_{dd}}(t, f)$ to be full rank, preferably diagonal. On the other hand, BSS techniques demand the diagonal structure of the same matrix without degenerate eigenvalues. These properties along with high signal-to-noise ratio (SNR) requirements may be difficult to achieve using a single t-f point. Two different methods can be used for integrating several t-f points into equation (3). One method is based on a simple averaging performed over the signatures of the sources of interest, whereas the second method is

based on incorporating several desired t-f points into joint diagonalization or joint block-diagonalization schemes.

3) The TFD of the white noise is distributed all over the t-f domain, whereas the TFDs of the source waveforms are likely to be confined to much smaller regions. Referring to Fig. II, the noise is spread over both R_a and R_b as well as the complement region R_c. If the t-f points (t, f) used in either the averaging or joint diagonalization approaches belong to the noise only region R_c, then no information of the incident waveforms is used and, as such, no reasonable source localization and signal separation outcomes can be obtained. On the other hand, if all points (t, f) in Fig. II are used, and the employed TFD satisfies the marginal constraints, then it can be easily shown that only the signal average power is considered. As a result, the problem simplifies to the second-order covariance based matrix approach, traditionally used in high resolution DOA estimation. This is an important feature, as it casts the conventional techniques as special cases of the array signal processing framework based on t-f analysis. Finally, if we confine the (t, f) points to R_a and R_b, then only the noise part in these regions is included. The result of leaving out the points (t, f) that are not part of the t-f signatures of the signal arrivals is enhancing the input SNR, which is utilized by the source localization and signal separation techniques.

4) By only selecting t-f points that belong to the t-f signature of one source, then this source will be the only one considered by equation (3). This selection, in essence, is equivalent to implicitly performing spatial filtering and removing other sources from consideration. It is important to note, however, that such removal does not come at the expense of reduction of the number of degrees-of-freedom (DOFs), as it is the case in beamspace processing, but the problem remains a sensor space processing with the original number of DOFs kept intact. This property represents a key contribution of TFDs to the direction finding and DOA estimation areas. An antenna array can be used to localize a number of sources equal or even greater than its number of sensors. The fundamental condition is that there must be t-f regions over which the respective t-f signatures of the sources do not overlap. Referring to Fig. II and considering the case of two sensors, if all t-f points incorporated in direction finding belong to region R_a and not R_b, then the signal subspace defined by equation (3) is one-dimensional. Thus, by excluding source

B, a one-dimensional noise subspace is established. This allows us to proceed with high resolution techniques for localization of source A. In a general scenario, one can localize one source at a time or a set of selected sources, depending on the array size, overlapping and distinct t-f regions, and the dimension of the noise subspace necessary to achieve the required resolution performance. The same concepts and advantages of t-f point selection discussed above for direction finding can be applied to BSS problems.

5) The *a priori* knowledge of some temporal characteristics or the nature of time-varying frequency contents of the sources of interest may permit us to directly select the t-f regions used in equation (3). For instance, it is known that, in the ambiguity domain, all fixed frequency sinusoidal signals map to the time-lag axis. By only incorporating the points on this axis, we have, in fact, opted to separate and localize all narrowband signals in broadband communications platforms.

III. Examples

In this Section, we present simulation examples to demonstrate the fundamental offerings discussed in the previous Section. Time-frequency MUSIC (t-f MUSIC), ambiguity-domain MUSIC (AD-MUSIC), and the BSS based on STFDs are three different techniques chosen for the demonstration. The algorithms involved in the implementation of the techniques are given in Tables I, II, and III [2], [4], [1].

Example I [4]. Consider the scenario of a four-element equi-spaced linear array spaced by half a wavelength, where one chirp signal and two sinusoidal signals are received. The data record has 128 samples. All three signals have the same SNR of 20 dB. The DOAs of the chirp signal and the two sinusoidal signals are 15°, 10°, and 0°, respectively. While the ambiguity function of the chirp signal sweeps the ambiguity domain with contribution at the origin, the exact autoterm ambiguity function of the narrowband arrivals $s_1(t)$ and $s_2(t)$ is zero for non-zero frequency-lags and may have non-zero values only along the vertical axis $v = 0$.

In this simulation example, we selected 24 points on the time-lag axis, excluding the origin, and as such emphasizing the narrowband components. Fig. III shows the ambiguity function where the two vertical lines away from the origin represent the crossterms between the sinusoidal components. Fig. III shows the two estimated spatial spectra for three

STEP I   Form K matrices $\mathbf{D_{xx}}(t_i, f_i)$ for the selected (t_i, f_i) points, $i = 1, \cdots, K$.

STEP II   The eigenvectors of $E\left[\mathbf{D_{xx}}(t, f)\right]$ corresponding to the $m - n$ smallest eigenvalues,$\mathbf{e}_1, \cdots, \mathbf{e}_{m-n}$, are obtained by joint block-diagonalization, or the eigen-decomposition of averaged matrix $\frac{1}{K}\sum_{i=1}^{K}\mathbf{D_{xx}}(t_i, f_i)$.

STEP III   Estimate the number of signals from the eigenvalues, and estimate the DOAs from the peaks of the t-f MUSIC spectra $f(\theta) = \left|\hat{\mathbf{E}}_n^H \mathbf{a}(\theta)\right|^{-2}$, where $\hat{\mathbf{E}}_n = [\mathbf{e}_1, \cdots, \mathbf{e}_{m-n}]$, and $\mathbf{a}(\theta)$ is the steering vector corresponding to DOA θ.

Ambiguity-Domain MUSIC

Ambiguity-Domain MUSIC follows the same procedure as time-frequency MUSIC by using $\mathbf{D_{xx}}(v_i, \tau_i)$ instead of $\mathbf{D_{xx}}(t_i, f_i)$, $i = 1, \cdots, K$.

independent trials, one corresponds to the conventional method and the other corresponds to the AD-MUSIC. There are two dominant eigenvalues for the case of the AD-MUSIC, since we have not deliberately considered the chirp signal through our careful selection of the ambiguity-domain points. It is clear that the AD-MUSIC resolves the two sinusoidal signals, while the conventional MUSIC could not separate the three signals.

Example II [5]. Consider a uniform linear array of eight sensors separated by half a wavelength. Two chirp signals emitted from two sources positioned at $(\theta_1, \theta_2) = (-10°, 10°)$,

STEP I   Estimate the auto-correlation matrix $\hat{\mathbf{R}}_{\mathbf{xx}}$ from T data samples. Denote by $\lambda_1, \cdots, \lambda_n$ the n largest eigenvalues and $\mathbf{h}_1, \cdots, \mathbf{h}_n$ the corresponding eigenvectors of $\hat{\mathbf{R}}_{\mathbf{xx}}$.

STEP II   An estimate $\hat{\sigma}^2$ of the noise variance is the average of the $m - n$ smallest eigenvalues of $\hat{\mathbf{R}}_{\mathbf{xx}}$. The whitening matrix is formed as $\hat{\mathbf{W}} = \left[(\lambda_1 - \hat{\sigma}^2)^{-\frac{1}{2}} \mathbf{h}_1, \cdots, (\lambda_n - \hat{\sigma}^2)^{-\frac{1}{2}} \mathbf{h}_n \right]^H$.

STEP III   Form K matrices by computing the STFD of whitened vector $\mathbf{z}(t) = \hat{\mathbf{W}} \mathbf{x}(t)$ for a fixed set of (t_i, f_i) points, $i = 1, \cdots, K$, corresponding to signal autoterms.

STEP IV   A unitary matrix $\hat{\mathbf{U}}$ is then obtained as joint diagonalizer of the set $\mathbf{D}_{\mathbf{zz}}(t_i, f_i), i = 1, \cdots, K$.

STEP V   The source signals are estimated as $\hat{\mathbf{s}}(t) = \hat{\mathbf{U}}^H \hat{\mathbf{W}} \mathbf{x}(t)$, and the mixing matrix $\mathbf{A}$ is estimated as $\hat{\mathbf{A}} = \hat{\mathbf{W}}^{\#} \hat{\mathbf{U}}$.

respectively. The data record has 1024 samples. The start and end frequencies of the chirp signal of the source at θ_1 are $f_{s1} = 0$ and $f_{e1} = 0.5$, while the corresponding two frequencies for the signal of the other source at θ_2 are $f_{s2} = 0.5$ and $f_{e2} = 0$, respectively.

Fig. III displays the standard deviations of the DOA estimation $\hat{\theta}_1$ versus SNR. The curves in this figure show the theoretical and experimental results of the conventional MUSIC and t-f MUSIC. Pseudo Wigner-Ville distribution with window length $L = 33$ and 129 are considered. The Cramer-Rao Bound (CRB) is also shown in Fig. III. Both signals are selected when performing t-f MUSIC. Simulation results are averaged over 100 independent trials of Monte Carlo experiments. The advantages of t-f MUSIC in low SNR
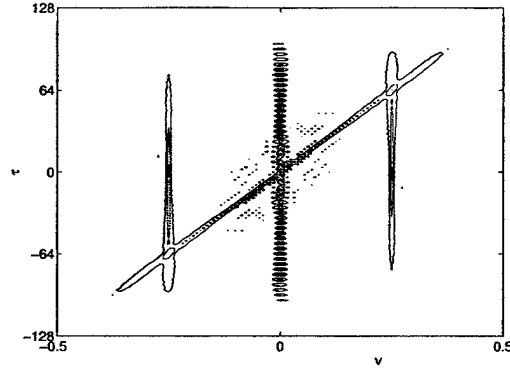
The ambiguity functions of the chirp signal and two sinusoidal signals.
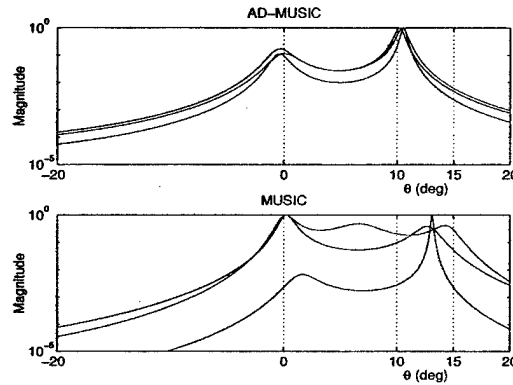
The estimated spatial spectra of AD-MUSIC and conventional MUSIC.

cases are evident from this figure. Fig. III shows estimated spatial spectra at SNR$=-20$ dB based on t-f MUSIC ($L = 129$) and the conventional MUSIC. The t-f MUSIC spectral peaks are clearly resolved.

Example III [1]. In Fig. III, we show an example of the application of STFDs to the BSS problem. A three-element equi-spaced linear array is considered where the interelement spacing is half a wavelength. Two chirp signals arrive at $-10°$ and $10°$, respectively. The number of data samples used to compute the STFD is 128. The number of t-f points employed in the joint diagonalization is p$=128$, with equal number of points on each signature. Fig. III(b) shows the Choi-Williams distributions of two linear mixtures of the original chirp signals depicted in Fig. III(a), corresponding to the data at the first and the second sensors. Using the STFDs, we are able to recover the original signals from their observed mixture, as shown in Fig. III(c).

IV. Crossterm Issues in STFD

There are two sources of crossterms. The first type are the crossterms that are the results of the interactions between the components of the same source signal. The other type of crossterms are those generated from the interactions between two signal components belonging to two different sources. These crossterms are associated with cross-TFDs of the source signals and, at any given t-f point, they constitute the off-diagonal entries of the source TFD matrices $\mathbf{D_{dd}}(t, f)$ defined in (3). Although the off-diagonal elements do not necessarily destroy the full-rank matrix property necessary for direction finding application [6], they violate the basic assumption in the problem of source separation regarding the diagonal structure of the source TFD matrix. We must therefore select the t-f points that belong to autoterm regions where crossterm contributions are at minimum, e.g., by using *a priori* information of the source signals.

The method of spatial averaging of the STFD introduced in [7] does not reduce the crossterms as in the case with reduced interference distribution kernels, but rather move them from their locations on the off-diagonal matrix entries to be part of the matrix diagonal elements. The other parts of the matrix diagonal elements represent the contribution of the autoterms at the same point. Therefore, not only we are able to set the off-diagonal elements of the source TFD matrix to zeros, but also we can improve performance by selecting the t-f points of peak values, irrespective of whether these points belong to autoterm or crossterm regions.
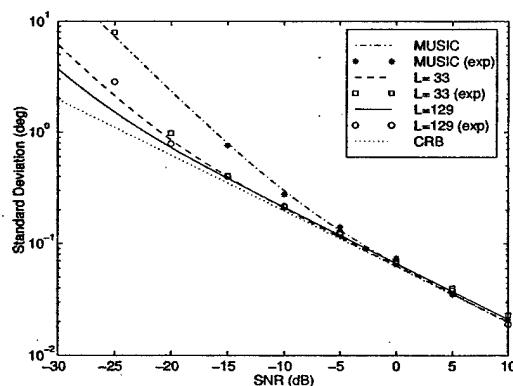
The standard deviations of DOA estimation $\hat{\theta}_1$ vs. SNR.

A. Summary and Conclusions

The spatial time-frequency distribution (STFD) is an important tool for temporal and spatial separations of sources emitting nonstationary signals. It is a discriminatory tool that allows a consideration of only a subset of source signals impinging on a multi-sensor receiver. This property enhances signal parameter estimation and permits direction finding and signal separation to be applied to a number of sources that is equal or even exceeds the number of sensors.

All material presented in this article is based on the model (2). One important change in the direction of the research in the time-frequency array signal processing area was given in [8], where the strict model of (2) was relaxed and a direction finding technique employing a STFD-based wideband root-MUSIC was proposed. Another research direction is the utilization and integration of crossterms into STFDs. It has recently been shown [9] that source separation can be performed based on both autoterms and crossterms through joint diagonalization and joint anti-diagonalization schemes of STFD matrices.

References

[1] A. Belouchrani and M. G. Amin, "Blind source separation based on time-frequency signal representation," *IEEE Trans. Signal Processing*, vol. 46, no. 11, pp. 2888–2898, Nov. 1998.
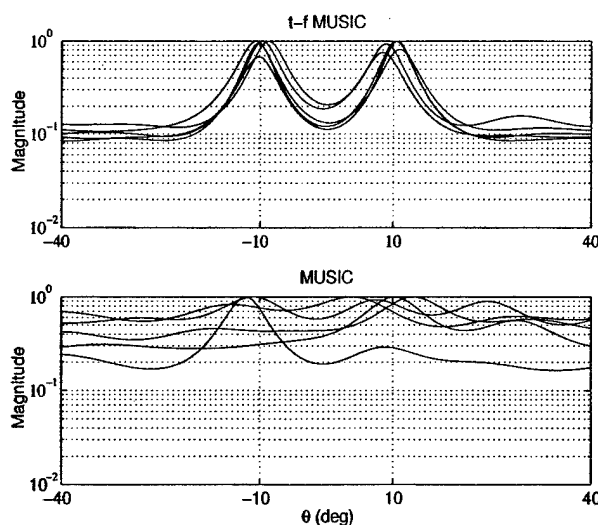
The estimated spatial spectra of t-f MUSIC and conventional MUSIC.

[2] A. Belouchrani and M. G. Amin, "Time-frequency MUSIC," *IEEE Signal Processing Letters*, vol. 6, no. 5, pp. 109–110, May 1999.

[3] Y. Zhang, W. Mu, and M. G. Amin, "Time-frequency maximum likelihood methods for direction finding," *J. Franklin Inst.*, vol. 337, no. 4, pp. 483–497, July 2000.

[4] M. G. Amin, A. Belouchrani, and Y. Zhang, "The spatial ambiguity function and its applications," *IEEE Signal Processing Letters*, vol. 7, no. 6, pp. 138–140, June 2000.

[5] Y. Zhang, W. Mu, and M. G. Amin, "Subspace analysis of spatial time-frequency distribution matrices," *IEEE Trans. Signal Processing*, vol. 49, no. 4, pp. 747–759, April 2001.

[6] M. G. Amin and Y. Zhang, "Direction finding based on spatial time-frequency distribution matrices," *Digital Signal Processing*, vol. 10, no. 4, pp. 325–339, Oct. 2000.

[7] Y. Zhang and M. G. Amin, "Spatial averaging of time-frequency distributions for signal recovery in uniform linear arrays," *IEEE Trans. Signal Processing*, vol. 48, no. 10, pp. 2892–2902, Oct. 2000.

[8] A. B. Gershman and M. G. Amin, "Wideband direction-of-arrival estimation of multiple chirp signals using spatial time-frequency distributions," *IEEE Signal Processing Letters*, vol. 7, no. 6, pp. 152–155, June 2000.

[9] A. Belouchrani, K. Abdel-Meraim, M. G. Amin, and A. Zoubir, "Joint anti-diagonalization for blind source separation," in *Proc. IEEE Int. Conf. Acoust., Speech, Signal Process.*, Salt Lake City, UT, May 2001.
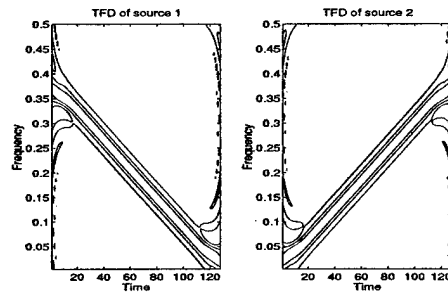
(a) TFDs of the source signals
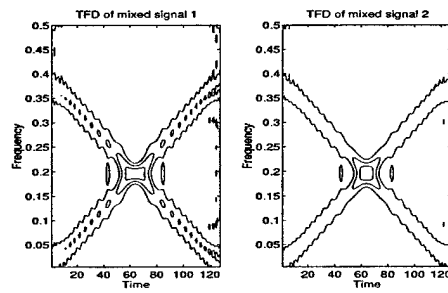
(b) TFDs of the mixed signals
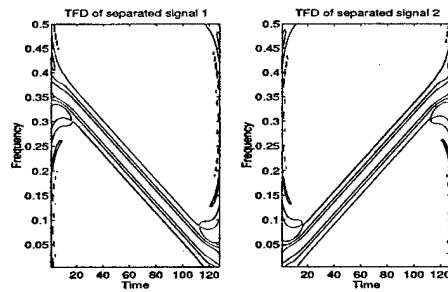
(c) TFDs of the separated signals

Blind source separation based on STFDs.

135

Polarimetric Array Processing for Nonstationary Signals [1]

Yimin Zhang, Moeness G. Amin, and Baha A. Obeidat

Center for Advanced Communications

Villanova University, Villanova, PA 19085, USA

Abstract

Time-frequency distributions (TFDs) have evolved to be a powerful technique for nonstationary signal analysis and synthesis. With the use of a multi-sensor array, spatial time-frequency distributions (STFDs) have been developed and successfully applied to high-resolution direction-of-arrival (DOA) estimations and blind recovery of the source waveforms. In this paper, we introduce the spatial polarimetric time-frequency distribution (SPTFD) as a platform to process nonstationary array signals with two orthogonal polarization components, such as horizontal and vertical. The use of dual polarization empowers the STFDs with additional degrees-of-freedom (DOFs) and improves the robustness of the signal and noise subspaces. This improvement serves to enhance DOA estimation and signal recovery. To demonstrate the effectiveness of the SPTFD platform, the polarimetric time-frequency ESPRIT (PTF-ESPRIT) method is proposed and is shown to outperform time-frequency, polarimetric, and conventional ESPRIT methods.

1 Introduction

Over the past two decades, time-frequency distributions (TFDs) have evolved to be a powerful technique for nonstationary signal analysis and synthesis in the areas of speech, biomedicine, automotive industry, and machine monitoring [1-5]. In radar signal processing, the time-frequency signal representation, in its linear and bilinear forms, has been used in target detection, classification, and clutter suppression [6-10]. Most recently, the spatial dimension has been incorporated, along with the time and frequency variables, into quadratic and higher-order time-frequency distributions, and led to the introduction of spatial time-frequency distributions (STFDs) for sensor signal processing. The STFD has been successfully applied to high-resolution direction-of-arrival (DOA) estimations and blind recovery of the source waveforms impinging on a multi-sensor receiver, specifically those of nonstationary temporal characteristics [11-19].

Polarization and polarization diversity, on the other hand, have been proven to be very effective in wireless communications and various types of radar systems [20,21]. Antenna and target polarization properties are widely employed in remote sensing and synthesis aperture radar (SAR) applications [22-24]. Presently, airborne and spaceborne platforms as well as meteorological radars include polarization information [25,26]. Additionally, polarization plays an effective role for target identification in the presence of clutter [27,28]. Polarization has also been incorporated in array antennas for improved signal parameter estimation, such as DOA and time-of-arrival (TOA) [29-31].

Despite the extensive research work performed in time-frequency signal representations and polarimetric signal processing methods, these two important areas have not been coupled or considered within the same platform. In numerous communications and radar applications, moving sources/targets often generate time-varying Doppler frequency, with well defined Doppler-frequency signatures. Also, mechanical vibration or rotation of structure in a source/target typically includes frequency modulation on returned signals. Time-frequency methods have been proposed to characterize the Doppler-frequency signature as well as to analyze micro-Doppler phenomenon. However, little attention, if any, has been paid to the fact that the return signal from a moving or

vibrating target may have a time-varying polarization. The polarimetric Doppler frequency signature contains valuable information that the single-polarization Doppler frequency signature fails to provide.

In this paper, we develop the spatial polarimetric time-frequency technique for multi-antenna receivers. This technique utilizes not only the time-varying Doppler frequency signatures, but also the polarization signatures, whether they are stationary or time-varying. The signal polarization information empowers the spatial time-frequency distributions (STFDs), as it retains the integrity of eigenstructure methods and improves the robustness of the respective signal and noise subspaces under low signal-to-noise ratio (SNR) and coherent signal environment.

The importance of this technique stems from the fact that targets, emitters, and scatters, when changing their positions, are likely to produce Doppler and polarization profiles that are time-dependent. If the field of view covers multiple sources, then target detection, source location, and signal recovery benefit from distinctions in polarization, spatial, and time-frequency signatures. With polarization no longer decoupled from the signal time-varying spectrum characteristics, high resolution imaging and DOA estimation can be achieved over the cases where the decoupling is enforced.

The focus of this paper is limited to the proposition of the SPTFD and, as its application example to demonstrate the effectiveness of this technique, polarimetric time-frequency ESPRIT (PTF-ESPRIT) for DOA estimation of noncoherent sources is considered [32]. The application to a MUSIC-like method for non-coherent and coherent signals is introduced separately in [33-35].

This paper is organized as follows. Section 2 introduces the signal model and briefly reviews the definition of STFD. In Section 3 the polarimetric time-frequency distribution (PTFD) and SPTFD are introduced and defined. The PTF-ESPRIT is proposed in Section 4. Section 5 presents simulation results and Section 6 concludes this paper.

Table 1. Notations

A	Matrix	$(.)^*$	complex conjugate
a	Vector	$(.)^{[i]}$	polarization index
$(.)^T$	Transpose	$(.)^H$	Hermitian

2 Signal Model

2.1 Time-Frequency Distributions

The Cohen's class of TFDs of a signal $x(t)$ is expressed as [4]

$$D_{xx}(t,f) = \iint \phi(t-u,\tau)x(t+\tau/2)x^*(t-\tau/2)\, e^{-j2\pi f\tau} du\, d\tau \tag{1}$$

where t and f represent the time index and frequency index, respectively. The kernel $\phi(t, \tau)$ uniquely defines the TFD and is a function of the time and lag variables. In this paper, all the integrals are from $-\infty$ to ∞.

The TFDs, given in Eq. (1), have been shown to be a powerful tool in analysis of signals with time-varying frequencies. They are used in different applications for ninstationary signal detection, classification, and discriminations [1-5]. The cross-sensor TFD of two signals $x_1(t)$ and $x_2(t)$ is defined by

$$D_{x_1 x_2}(t,f) = \iint \phi(t-u,\tau)x_1(t+\tau/2)x_2^*(t-\tau/2)\, e^{-j2\pi f\tau} du\, d\tau \,. \tag{2}$$

2.2 Spatial Time-Frequency Distributions

Consider a narrowband array processing problem, where n signals arrive at an m-element array. The following linear data model is assumed,

$$\mathbf{x}(t) = \mathbf{A}\mathbf{s}(t) + \mathbf{n}(t) \qquad (3)$$

where the $m \times n$ spatial matrix $\mathbf{A} = [\mathbf{a}_1, \mathbf{a}_2, \cdots, \mathbf{a}_n]$ is the mixing matrix which holds the spatial information. In this paper, structured mixing matrix, that is, $\mathbf{A} = \mathbf{A}(\Theta) = [\mathbf{a}(\theta_1), \mathbf{a}(\theta_2), \cdots, \mathbf{a}(\theta_n)]$ is assumed, where $\Theta = [\theta_1, \theta_2, \cdots, \theta_n]$. The elements of the $m \times 1$ vector $\mathbf{x}(t)$, which represents the measured or sensor data, are multi-component signals, while the elements of the $n \times 1$ vector $\mathbf{s}(t) = [s_1(t), s_2(t), \cdots, s_n(t)]^T$ are often mono-component signals. $\mathbf{n}(t)$ is an $m \times 1$ additive noise vector, which consists of independent zero-mean, white and Gaussian distributed processes.

The STFD of a data vector $\mathbf{x}(t)$ is expressed as [11]

$$\mathbf{D}_{\mathbf{xx}}(t, f) = \iint \phi(t - u, \tau) \mathbf{x}(t + \tau/2) \mathbf{x}^H(t - \tau/2) \, e^{-j2\pi f \tau} du d\tau \qquad (4)$$

where the (i, k)th element of $\mathbf{D}_{\mathbf{xx}}(t, f)$ is defined as $[\mathbf{D}_{\mathbf{xx}}(t, f)]_{ik} = D_{x_i x_k}(t, f)$, $i, k = 1, 2, \cdots, m$.

Due to the linear data model, the noise-free STFD is obtained by substituting (3) into (4),

$$\mathbf{D}_{\mathbf{xx}}(t, f) = \mathbf{A}(\Theta) \mathbf{D}_{\mathbf{ss}}(t, f) \mathbf{A}^H(\Theta) \qquad (5)$$

where $\mathbf{D}_{\mathbf{ss}}(t, f)$ is the TFD matrix of $\mathbf{s}(t)$ which consists of auto- and cross-source TFDs as its elements. With the presence of noise, which is uncorrelated with the signals, the expected values of the above equations yields

$$E[\mathbf{D}_{\mathbf{xx}}(t, f)] = \mathbf{A}(\Theta) E[\mathbf{D}_{\mathbf{ss}}(t, f)] \mathbf{A}^H(\Theta) + \sigma \mathbf{I}. \qquad (6)$$

In the above equation, σ is the noise power, $\mathbf{I}$ is the identity matrix, and $E[.]$ denotes the statistical expectation operator.

Equations (5) and (6) are similar to the mathematical formula which has been commonly used in narrowband array processing problems, relating the source correlation matrix to the sensor spatial correlation matrix. However, the correlation matrices are replaced by the source and sensor TFD matrices. The two subspaces spanned by the principle eigenvectors of $\mathbf{D}_{\mathbf{xx}}(t, f)$ and the columns of

$\mathbf{A}(\Theta)$ are, therefore, identical. In [13-15] it is further shown that, by only selecting the t-f points with highly localized signal energy, the eigenvalues and eigenvectors estimated from $\mathbf{D}_{xx}(t,f)$ are more robust to noise than their counterparts obtained from the corresponding data covariance matrix $\mathbf{R}_{xx} = E[\mathbf{x}(t)\mathbf{x}^H(t)]$. This implies that key problems in various array processing applications can be addressed and solved using a new formulation that is more tuned to nonstationary signal environments.

3 Spatial Polarimetric Time-Frequency Distributions

3.1 Polarimetric Time-Frequency Distributions

In passive radar, sonar, and most communication problems, the received signal with dual polarizations can be expressed as

$$\underline{x}(t) = [x^{[p]}(t) \quad x^{[q]}(t)]^T \tag{7}$$

where the superscripts $(.)^{[p]}$ and $(.)^{[q]}$, respectively, denote two orthogonal polarizations. They can be, for example, vertical and horizontal polarizations, or right-hand and left-hand circular polarizations.

In active radar and sonar applications, the received signal with dual transmit and dual receive polarizations can be expressed as

$$\underline{x}(t) = [x^{[pp]}(t) \quad x^{[pq]}(t) \quad x^{[qp]}(t) \quad x^{[qq]}(t)]^T \tag{8}$$

where the first letter of the superscript denotes the transmit polarization, and the second letter denotes the receive polarization. For notation simplicity and uniformity, we focus only on the pp and qq components, and let $x^{[p]}(t)$ and $x^{[q]}(t)$ denote $x^{[pp]}(t)$ and $x^{[pp]}(t)$, respectively. In this way, Eq. (7) can be used to represent both passive and active signal processing.

The self- and cross-polarized TFD are expressed as

$$D_{x^{[i]}x^{[i]}}(t,f) = \iint \phi(t-u,\tau)x^{[i]}(t+\tau/2)\left(x^{[i]}(t-\tau/2)\right)^* e^{-j2\pi f\tau}dud\tau \qquad (9)$$

and

$$D_{x^{[i]}x^{[k]}}(t,f) = \iint \phi(t-u,\tau)x^{[i]}(t+\tau/2)\left(x^{[k]}(t-\tau/2)\right)^* e^{-j2\pi f\tau}dud\tau \qquad (10)$$

where the superscripts i and k denote either p or q. The self- and cross-polarized TFDs together define the polarization TFD matrix,

$$\mathbf{D}_{\underline{xx}}(t,f) = \iint \phi(t-u,\tau)\underline{x}(t+\tau/2)\underline{x}^H(t-\tau/2)\,e^{-j2\pi f\tau}dud\tau \ . \qquad (11)$$

The polarization TFD matrix is of dimension 2×2, although it can be 4×4 if the full four element representation in Eq. (8) is used. The diagonal elements of $\mathbf{D}_{\underline{xx}}(t,f)$ are the self-polarized terms $D_{x^{[i]}x^{[i]}}(t,f)$, whereas the off-diagonal elements are the cross-polarized terms $D_{x^{[i]}x^{[k]}}(t,f)$, $i \ne k$. Accordingly, the polarization TFD matrix can be used to estimate the self- and cross-polarization signatures of propagation channels.

3.2 Spatial Polarimetric Time-Frequency Distributions

Equations (7)-(11) correspond to a single dual-polarization sensor case. When an array consisting of m dual-polarized sensors is considered, the data vector, for each polarization i, is expressed as,

$$\mathbf{x}^{[i]}(t) = \mathbf{A}^{[i]}(\Theta)\mathbf{s}^{[i]}(t) + \mathbf{n}^{[i]}(t) \ . \qquad (12)$$

It is noted that, for structured mixing matrices, they are polarization-independent, i.e., $\mathbf{A}^{[p]}(\Theta) = \mathbf{A}^{[q]}(\Theta) = \mathbf{A}(\Theta)$, and Eq. (12) simplifies to the following,

$$\mathbf{x}^{[i]}(t) = \mathbf{A}(\Theta)\mathbf{s}^{[i]}(t) + \mathbf{n}^{[i]}(t) \ . \qquad (13)$$

The generalization of Eq. (9) to the multi-sensor receiver is obtained using Eq. (13). The STFD matrix introduced in Eq. (4) can be defined for each polarization

$$\mathbf{D}_{\mathbf{x}^{[i]}\mathbf{x}^{[i]}}(t,f) = \iint \phi(t-u,\tau)\mathbf{x}^{[i]}(t+\tau/2)\left(\mathbf{x}^{[i]}(t-\tau/2)\right)^{H} e^{-j2\pi f\tau} du d\tau . \qquad (14)$$

In the noise-free environment

$$\mathbf{D}_{\mathbf{x}^{[i]}\mathbf{x}^{[i]}}(t,f) = \mathbf{A}(\mathbf{\Theta})\mathbf{D}_{\mathbf{s}^{[i]}\mathbf{s}^{[i]}}(t,f)\mathbf{A}^{H}(\mathbf{\Theta}) . \qquad (15)$$

In a similar manner, the cross-polarization STFD matrix between the data vectors with two different polarizations can be obtained as,

$$\mathbf{D}_{\mathbf{x}^{[i]}\mathbf{x}^{[n]}}(t,f) = \mathbf{A}(\mathbf{\Theta})\mathbf{D}_{\mathbf{s}^{[i]}\mathbf{s}^{[n]}}(t,f)\mathbf{A}^{H}(\mathbf{\Theta}) . \qquad (16)$$

We are now in a position to tie the polarization, the spatial, and the t-f properties of the signals incident on the antenna array. Based on Eq. (12), the following vector can be constructed for both polarizations,

$$\mathbf{x}(t) = \begin{bmatrix} \mathbf{x}^{[p]}(t) \\ \mathbf{x}^{[q]}(t) \end{bmatrix} = \begin{bmatrix} \mathbf{A}(\mathbf{\Theta}) & \mathbf{0} \\ \mathbf{0} & \mathbf{A}(\mathbf{\Theta}) \end{bmatrix} \begin{bmatrix} \mathbf{s}^{[p]}(t) \\ \mathbf{s}^{[q]}(t) \end{bmatrix} + \begin{bmatrix} \mathbf{n}^{[p]}(t) \\ \mathbf{n}^{[q]}(t) \end{bmatrix}$$
$$= \mathbf{B}(\mathbf{\Theta})\mathbf{s}(t) + \mathbf{n}(t) \qquad (17)$$

where $\mathbf{B}(\mathbf{\Theta}) = \begin{bmatrix} \mathbf{A}(\mathbf{\Theta}) & \mathbf{0} \\ \mathbf{0} & \mathbf{A}(\mathbf{\Theta}) \end{bmatrix}$ is block-diagonal and $\mathbf{s}^{[i]}(t)$, $i=p,q$, are the source signal vectors for polarization i. The STFD of the dual-polarization vector, $\mathbf{x}(t)$, can therefore be defined as

$$\mathbf{D}_{\mathbf{xx}}(t,f) = \iint \phi(t-u,\tau)\mathbf{x}(t+\tau/2)\mathbf{x}^{H}(t-\tau/2) e^{-j2\pi f\tau} du d\tau$$
$$= \begin{bmatrix} \mathbf{A}(\mathbf{\Theta}) & \mathbf{0} \\ \mathbf{0} & \mathbf{A}(\mathbf{\Theta}) \end{bmatrix} \begin{bmatrix} \mathbf{D}_{\mathbf{s}^{[p]}\mathbf{s}^{[p]}}(t,f) & \mathbf{D}_{\mathbf{s}^{[p]}\mathbf{s}^{[q]}}(t,f) \\ \mathbf{D}_{\mathbf{s}^{[q]}\mathbf{s}^{[p]}}(t,f) & \mathbf{D}_{\mathbf{s}^{[q]}\mathbf{s}^{[q]}}(t,f) \end{bmatrix} \begin{bmatrix} \mathbf{A}(\mathbf{\Theta}) & \mathbf{0} \\ \mathbf{0} & \mathbf{A}(\mathbf{\Theta}) \end{bmatrix}^{H} \qquad (18)$$

$\mathbf{D}_{\mathbf{xx}}(t,f)$ is referred to as the spatial polarimetric time-frequency distribution (SPTFD) matrix. This distribution serves as a general framework within which typical problems in array processing can be addressed [32-35]. In the next section, the polarimetric time-frequency ESPRIT (PTF-ESPRIT) [32] is shown as an application example of the SPTFD.

4 Polarimetric Time-Frequency ESPRIT

In order to achieve the rotational invariance in the array at hand, we consider a uniform linear array with m cross-dipoles. This array is divided into two overlapping subarrays of m-1 elements. Let the first subarray be composed of the left-most m-1 cross-polarized antennas, and the second subarray be composed of the right-most m-1 cross-dipoles. Additionally, let the array response matrices of the identically polarized sensors of the two subarrays be $\mathbf{A}_1(\Theta)$ and $\mathbf{A}_2(\Theta)$, respectively. Accordingly,

$$\begin{bmatrix} \mathbf{A}_2(\Theta) & 0 \\ 0 & \mathbf{A}_2(\Theta) \end{bmatrix} = \begin{bmatrix} \mathbf{A}_1(\Theta) & 0 \\ 0 & \mathbf{A}_1(\Theta) \end{bmatrix} \begin{bmatrix} \Phi & 0 \\ 0 & \Phi \end{bmatrix}, \tag{19}$$

where the rotation operator Φ can be modeled as

$$\Phi = \text{diag}[e^{-j2\pi\frac{d}{\lambda}\sin(\theta_1)}, e^{-j2\pi\frac{d}{\lambda}\sin(\theta_2)}, \ldots, e^{-j2\pi\frac{d}{\lambda}\sin(\theta_n)}], \tag{20}$$

d is the interelement spacing, and λ is the wavelength of the impinging signals.

By performing joint block-diagonalization [12,36] on the SPTFD matrices $\mathbf{D}_{xx}(t,f)$ over multiple (t,f) points where the energy of the signal arrivals is concentrated, we obtain the signal and noise subspaces, represented as matrices $\mathbf{U}_s$ and $\mathbf{U}_n$, respectively.

The signal eigenvectors, comprising the columns of $\mathbf{U}_s$, span approximately the signal subspace of dimension n such that there exists a transformation matrix $\mathbf{T}$ that satisfies

$$\mathbf{U}_s = \begin{bmatrix} \mathbf{A}(\Theta) & 0 \\ 0 & \mathbf{A}(\Theta) \end{bmatrix} \mathbf{T} \tag{21}$$

where $\mathbf{A}(\Theta)$ is the full (undivided) array response matrix for one polarization.

By applying the same transformation matrix $\mathbf{T}$ to the steering matrices of the two subarrays, the following matrices are defined,

$$\mathbf{U}_{s1} = \begin{bmatrix} \mathbf{A}_1(\Theta) & \mathbf{0} \\ \mathbf{0} & \mathbf{A}_1(\Theta) \end{bmatrix} \mathbf{T} \qquad (22)$$

and

$$\mathbf{U}_{s2} = \begin{bmatrix} \mathbf{A}_2(\Theta) & \mathbf{0} \\ \mathbf{0} & \mathbf{A}_2(\Theta) \end{bmatrix} \mathbf{T}. \qquad (23)$$

Using the above two equations, we have

$$\mathbf{U}_{s2} = \mathbf{U}_{s1}\mathbf{\Psi}, \qquad (24)$$

where the matrix $\mathbf{\Psi}$ satisfies

$$\mathbf{\Psi} = \mathbf{T}^{-1}\begin{bmatrix} \Phi & \mathbf{0} \\ \mathbf{0} & \Phi \end{bmatrix}\mathbf{T}. \qquad (25)$$

where the eigenvalues of the matrix $\mathbf{\Psi}$ are $e^{-j2\pi\frac{d}{\lambda}\sin(\theta_i)}$, $i = 1, 2, \ldots ,n$ [35]. In order to find the matrix $\mathbf{\Psi}$ one has to solve the underdetermined equation (24) using the least-squares or the total least-squares approach [37]. When the least-squares approach is applied, the solution to (24) is

$$\mathbf{\Psi} = (\mathbf{U}_{s1}{}^{H}\mathbf{U}_{s1})^{-1}\mathbf{U}_{s1}{}^{H}\mathbf{U}_{s2}. \qquad (26)$$

5 Simulations

We consider a uniform linear array of four dual-polarization cross-dipoles, $m=4$, with half-wavelength inter-element spacing. To fully demonstrate the advantages of the proposed SPTFD framework and the PTF-ESPRIT algorithm, we consider two far-field sources (sources 1 and 2) with high-order frequency modulated (FM) waveforms in the presence of an undesired sinusoidal signal (source 3). Table 2 shows three respective DOAs (measured from the broadside), and the two

145

polarization parameters, γ and ϕ, representing the amplitude ratio ($\tan(\gamma) = \left| s^{[p]}(t) / s^{[q]}(t) \right|$) and phase

difference between the two polarization components, respectively. The normalized frequency of the

sinusoid is 0.1. All signals have the same signal power (SNR=5 dB). The data length is 256 samples.

The pseudo Wigner-Ville distribution (PWVD) is used to compute the TFDs where a rectangular

window of length 65 is used.

Table 2. Signal parameters

	DOA (deg)	γ (deg)	ϕ (deg)
Source 1	-3	45	0
Source 2	3	45	180
Source 3	5	20	0

5.1 Array and Polarization Averaging of TFDs

The proper selection of t-f autoterms is often important in array processing based on STFDs and

SPTFDs [14,16,38]. The presence of crossterms and noise often obscure the identification and

selection of t-f autoterm regions. Averaging TFDs across different sensors and different polarizations

can suppress the effect of noise and crossterms and render it easier to identify the autoterm TFDs

[39,40]. The suppression of crossterms is highly dependent on the spatial correlations and polarization

diversity among the signals.

Figure 1 shows the PWVD of the signal received at the first vertical sensor. With the single sensor

and single polarization, the crossterms between the source signals and the noise obscure the correct

identification of the autoterm of each signal component. Figure 2 shows the PWVD averaged across

the four vertical sensors. While the noise is substantially suppressed, the array averaging does not

significantly reduce the crossterms because of the close orientation of the sources. To further suppress

the crossterms, we utilize both the spatial and polarization information. Figure 3 shows the PWVD averaged over the four sensors and both polarizations. In this example, because source 1 and source 2 have orthogonal polarizations, their associated crossterms are completely suppressed.
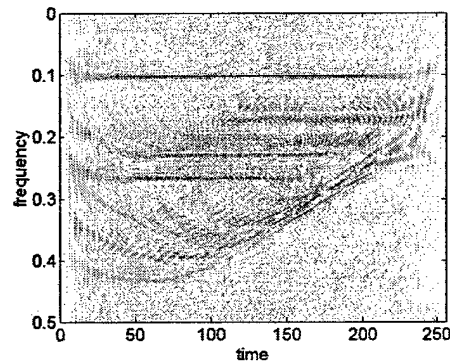

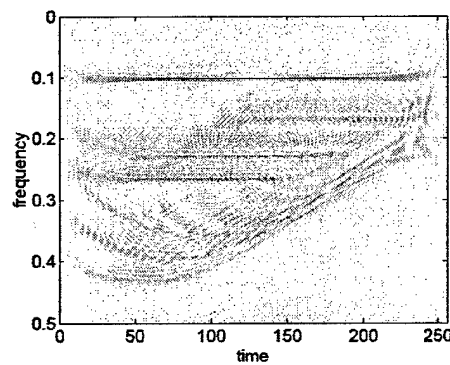Figure 1. PWVD of the vertical component received at the first antenna sensor.

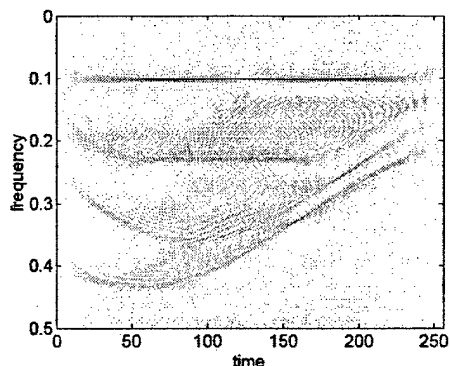Figure 2. PWVD of the vertical components averaged across four antenna sensors.

Figure 3. PWVD averaged across four antennas and both polarizations.

5.2 PTF-ESPRIT

For both time-frequency ESPRIT (t-f ESPRIT) [18] and PTF-ESPRIT, the array averaged PWVD is first used to identify the autoterm regions. The search-free PTF-ESPRIT provides a DOA estimation which is compared to that of the conventional ESPRIT, polarimetric ESPRIT, and t-f ESPRIT. In the underlying situation where the source signatures can be separated in the t-f domain, only the t-f points on the signal signature of a single source are considered for STFD and SPTFD matrix construction. The PTF-ESPRIT outperforms other ESPRIT-based methods by taking advantages of such source discriminatory capability, in addition to the SNR enhancement and polarimetric selection.

Figure 4 shows the root mean square error (RMSE) performance of the PTF-ESPRIT and other ESPRIT-based methods versus the input SNR, where the least-squares approach is used for all methods and the results are obtained from 100 independent trials. For conventional and t-f ESPRIT, only the vertical polarization components of the source signals are used. For the t-f and PTF-ESPRIT methods, only the first source signal is selected in STFD and SPTFD matrix construction, respectively. The RMSE performance is evaluated for the first source signal. It is evident that the PTF-ESPRIT outperforms all the other methods. It is clear that the polarimetric ESPRIT provides

satisfactory DOA estimation only when the input SNR is moderate, and the conventional ESPRIT fails to do so for all the input SNR values simulated. To the contrary, the PTF-ESPRIT provides 1-degree RMSE when the input SNR is at a low level of about -7 dB.
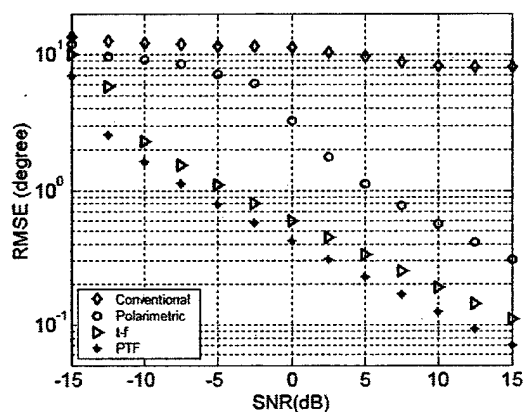

Figure 4. RMSE performance of ESPRIT algorithms versus input SNR.

In Figure 5, DOA estimates of 30 independent trials are shown for the different ESPRIT methods utilizing the least-squares approach, where the input SNR is 5 dB. It is evident that, at this low input SNR level, only the PTF-ESPRIT produces accurate and consistent estimates of the DOAs of all three signals. While the t-f ESPRIT provides comparable DOA estimation for source signal 1, the variance of the DOA estimations is much greater for the other two signals.
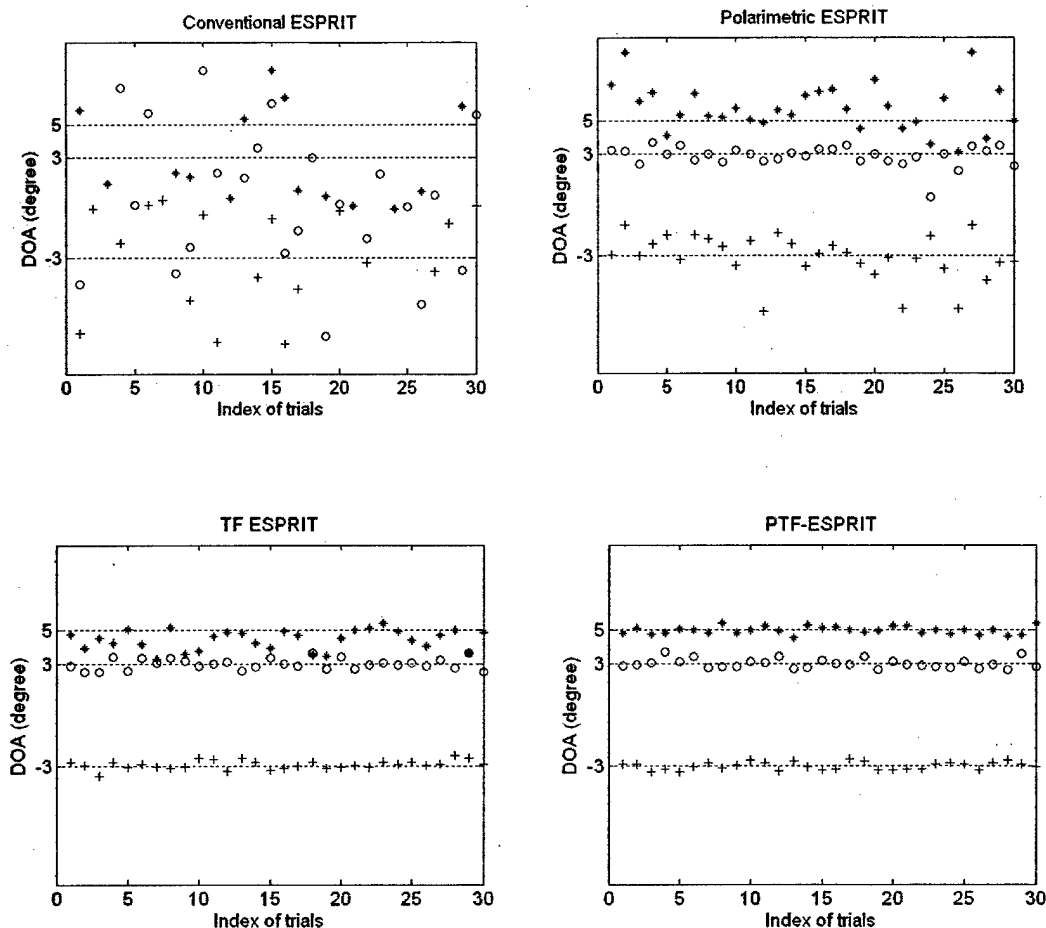
Figure 5. DOA estimation results from different ESPRIT methods.

6 Conclusion

The concept of SPTFD has been proposed and shown to be a powerful platform to utilize the polarization and temporal signatures of signal arrivals for sophisticated array processing. To demonstrate the advantage of the SPTFD platform, we have considered the DOA estimation problem and proposed the polarimetric time-frequency ESPRIT (PTF-ESPRIT) method as an example of its applications. In such scenarios where the signals are highly localized in the time-frequency domain and diversely polarized, the proposed PTF-ESPRIT significantly outperforms the other existing

ESPRIT methods, including conventional ESPRIT, time-frequency ESPRIT, and polarimetric ESPRIT.

Reference

[1] L. Cohen, "Time-frequency distributions - a review," *Proc. IEEE*, vol. 77, no. 7, pp. 941-981, July 1989.

[2] B. Boashash, "Time-frequency signal analysis," in S. Haykin (ed.), *Advances in Spectrum Analysis and Array Processing*, Englewood Cliffs, NJ: Prentice Hall, 1990.

[3] F. Hlawatsch and G. Boudreaux-Bartels, "Linear and quadratic time-frequency signal representations," *IEEE Signal Processing Mag.*, vol. 9, no. 2, pp. 21-68, April 1992.

[4] L. Cohen, *Time-Frequency Analysis*, Englewood Cliffs, NJ: Prentice Hall, 1995.

[5] S. Qian and D. Chen, *Joint Time-Frequency Analysis - Methods and Applications*, Englewood Cliffs, NJ: Prentice Hall, 1996.

[6] S. Barbarossa and A. Farina, "Detection and imaging of moving objects with synthetic aperture radar - part II: joint time-frequency by Wigner-Ville distribution," *IEE Proc. F*, vol. 139, no. 1, pp. 89-97, February 1992.

[7] O. P. Kenny and B. Boashash, "Time-frequency analysis of backscattered signals from diffuse radar targets," *IEE Proc. F*, vol. 140, no. 3, pp. 198-208, June 1993.

[8] V. C. Chen and S. Qian, "Joint time-frequency transform for radar range-Doppler imaging," *IEEE Trans. Aerospace and Electronic Systems*, vol. 34, no. 2, pp. 486-499, April 1998.

[9] V. C. Chen and H. Ling, "Joint time-frequency analysis for radar signal and image processing," *IEEE Signal Processing Mag.*, vol. 16, no. 2, pp. 81-93, March 1999.

[10] K.-T. Kim, I.-S. Choi, and H.-T. Kin, "Efficient radar target classification using adaptive joint time-frequency processing," *IEEE Trans. Antennas Propagat.*, vol. 48, no. 12, pp. 1789-1801, December 2000.

[11] A. Belouchrani and M. G. Amin, "Blind source separation based on time-frequency signal representations," *IEEE Trans. Signal Processing*, vol. 46, no. 11, pp. 2888-2897, November 1998.

[12] A. Belouchrani and M. G. Amin, "Time-frequency MUSIC," *IEEE Signal Processing Letters*, vol. 6, pp. 109-110, May 1999.

[13] Y. Zhang, W. Mu, and M. G. Amin, "Time-frequency maximum likelihood methods for direction finding," *J. Franklin Institute*, vol. 337, no. 4, pp. 483-497, July 2000.

[14] M. G. Amin and Y. Zhang, "Direction finding based on spatial time-frequency distribution matrices," *Digital Signal Processing*, vol. 10, no. 4, pp. 325-339, October 2000.

[15] Y. Zhang, W. Mu, and M. G. Amin, "Subspace analysis of spatial time-frequency distribution matrices," *IEEE Trans. Signal Processing*, vol. 49, no. 4, pp. 747-759, April 2001.

[16] M. G. Amin, Y. Zhang, G. J. Frazer, and A. R. Lindsey, "Spatial time-frequency distributions: Theory and applications," in L. Debnath (ed.), *Wavelets and Signal Processing*, Boston, MA: Birkhauser, 2003.

[17] A. R. Leyman, Z. M. Kamran, and K. Abed-Meraim, "Higher-order time frequency-based blind source separation technique," *IEEE Signal Processing Letters*, vol. 7, no. 7, pp. 193-196, July 2000.

[18] A. Hassanien, A. B. Gershman, and M. G. Amin, "Time-frequency ESPRIT for direction-of-arrival estimation of chirp signals," *Proceedings of IEEE Sensor Array and Multichannel Signal Processing Workshop*, Rosslyn, VA, August 2002.

[19] L. A. Cirillo, A. M. Zoubir, and A. B. Gershman, "Direction-of-arrival estimation for uncorrelated FM signals," *Proceedings of IEEE Sensor Array and Multichannel Signal Processing Workshop*, Rosslyn, VA, August 2002.

[20] W. C. Y. Lee and Y. S. Yeh, "Polarization diversity for mobile radio," *IEEE Trans. Communications*, vol. COM-20, pp. 912-923, May 1972.

[21] D. Giuli, "Polarization diversity in radars," *Proc. IEEE*, vol. 74, no. 2, pp. 245-269, February 1986.

[22] A. I. Kozlov, L. P. Ligthart, and A. I. Logvin, *Mathematical and Physical Modelling of Microwave Scattering and Polarimetric Remote Sensing*, London, U.K.: Kluwer Academic, 2001.

[23] D. J. McLaughlin, Y. Wu, W. G. Stevens, X. Zhang, M. J. Sowa, and B. Weijers, "Fully polarimetric bistatic radar scattering behavior of forested hills," *IEEE Trans. Antennas Propagat.*, vol. 50, no. 2, pp. 101-110, February 2002.

[24] F. Sadjadi, "Improved target classification using optimum polarimetric SAR signatures," *IEEE Trans. Aerospace and Electronic Systems*, vol. 38, no. 1, pp. 38-49, January 2002

[25] A. L. Pazmany, R. E. McIntosh, R. D. Kelly, and G. Vali, "An airborne 95 GHz dual-polarized radar for cloud studies," *IEEE Trans. Geoscience and Remote Sensing*, vol. 32, no. 4, pp. 731-739, July 1994.

[26] S. H. Yueh, W. J. Wilson, and S. Dinardo, "Polarimetric radar remote sensing of ocean surface wind," *IEEE Trans. Geoscience and Remote Sensing*, vol. 40, no. 4, pp. 793-800, April 2002.

[27] G. A. Ioannidids and D. E. Hammers, "Optimum antenna polarizations for target discrimination in clutter," *IEEE Trans. Antennas Propagat.*, vol. AP-27, pp. 357-363, 1979.

[28] D. A. Garren, A. C. Odom, M. K. Osborn, J. S. Goldstein, S. U. Pillai, and J. R. Guerci, "Full-polarization matched-illumination for target detection and identification," *IEEE Trans. Aerospace and Electronic Systems*, vol. 38, no. 3, pp. 824-837, July 2002.

[29] J. Li and R. T. Compton, "Angle estimation using a polarization sensitive array," *IEEE Trans. Antennas Propagat.*, vol. 39, no. 10, pp. 1539-1543, October 1991.

[30] E. R. Ferrara and T. M. Parks, "Direction finding with an array of antennas having diverse polarizations," *IEEE Trans. Antennas Propagat.*, vol. 31, pp. 231-236, March 1983.

[31] H. Yamada, K. Onishi, and Y. Yamaguchi, "Polarimetric superresolution technique for 2-D radar target imaging," *Proc. SPIE*, vol. 3120, pp. 317-326, 1997.

[32] B. A. Obeidat, Y. Zhang, and M. G. Amin, "Polarimetric time-frequency ESPRIT," *Annual Asilomar Conference on Signals, Systems, and Computers*, Pacific Grove, CA, Nov. 2003. (submitted)

[33] Y. Zhang, M. G. Amin, and B. A. Obeidat, "Direction finding using spatial polarimetric time-frequency distributions," *Int. Symp. Signal Processing and Its Applications*, Paris, France, July 2003.

[34] Y. Zhang, M. G. Amin, and B. A. Obeidat, "The spatial polarimetric time-frequency distributions and their application to direction-of-arrival estimation," *Proc. SPIE*, vol. 5205, Aug. 2003.

[35] Y. Zhang, B. A. Obeidat, and M. G. Amin, "Polarimetric time-frequency MUSIC in coherent signal environment," *IEEE Workshop on Statistical Signal Processing*, St. Louis, MO, Sept. 2003.

[36]   A. Belouchrani, M. G. Amin, and K. Abed-Meraim, "Direction finding in correlated noise fields based on joint block-diagonalization of spatio-temporal correlation matrices," *IEEE Signal Processing Letters*, vol. 4, no. 9, pp. 266-268, Sept. 1997.

[37] R. Roy and T. Kailath, "ESPRIT-estimation of signal parameters via rotational invariance techniques," *IEEE Trans. Acoust., Speech, Signal Processing*, vol. 37, pp. 984-995, July 1989.

[38] A. Belouchrani, K. Abed-Meraim, M. G. Amin, and A. M. Zoubir, "Joint anti-diagonalization for blind source separation," *Proc. ICASSP*, Salt Lake City, UT, pp. 2789-2792, May 2001.

[39] W. Mu, M. G. Amin, and Y. Zhang, "Bilinear signal synthesis in array processing," *IEEE Trans. Signal Processing*, vol. 51, no. 1, pp. 90-100, Jan. 2003.

[40] M. G. Amin and Y. Zhang, "Bilinear signal synthesis using polarization diversity," *IEEE Signal Processing Letters*. (in press)

ONR FY03 Collection Data

REPORTING PERIOD: 1 October 2002 to 30 September 2003

NAME OF PI: Moeness AMIN

UNIVERSITY/Contractor: Villanova University

TITLE OF PROJECT: Classification and Discrimination of Sources with Time-Varying Frequency and Spatial Spectra

GRANT/CONTRACT/WORK REQUEST NUMBER: N00014-98-1-0176

1.   Papers published in referred journals (TITLE; JOURNAL):

W. Mu, M. G. Amin, and Y. Zhang, "Bilinear signal synthesis in array processing," IEEE Transactions on Signal Processing, vol. 51, no. 1, Jan. 2003.

Y. Zhang, M. G. Amin, and G. J. Frazer, "High-resolution time-frequency distributions for maneuvering target detection in over-the-horizon radars," accepted for publication in the IEE Proceedings on Radar, Sonar and Navigation.

G. Wang, X.-G. Xia, B. T. Root, V. C. Chen, Y. Zhang, and M. G. Amin, "Maneuvering target detection in over-the-horizon radar by using adaptive clutter rejection and adaptive chirplet transform," accepted for publication in the IEE Proceedings on Radar, Sonar and Navigation.

M. G. Amin and Y. Zhang, "Bilinear signal synthesis using polarization diversity," accepted for publication in the IEEE Signal Processing Letters.

A. Belouchrani, M. G. Amin, K. Marium, and A. Zoubir, "Blind Separation of Non-Stationary Sources using joint anti-diagonalization," accepted for publication in the IEEE Signal Processing Letters.

2.   Books or Book chapters published (TITLE; AUTHORS/EDITORS; PUBLISHER):

M. G. Amin, Y. Zhang, G. J. Frazer, and A. R. Lindsey, "Spatial time-frequency distributions: Theory and applications," in L. Debnath (ed.), Wavelets and Signal Processing, Boston, MA: Birkhauser, 2003.

M. G. Amin and Y. Zhang, "Interference suppression in spread spectrum communication systems," in J. G. Proakis (ed.), The Wiley Encyclopedia of Telecommunications, New York, NY: John Wiley, 2002.

M. G. Amin and Y. Zhang, "Spatial time-frequency distributions and their applications," in B. Boashash, Time-Frequency Signal Analysis and Processing: A Comprehensive Reference, Oxford, UK: Elsevier, 2003.

Y. Zhang, M. G. Amin, and B. Obeidat, "Polarimetric array processing for nonstationary signals," in S.Chandran (ed.), Adaptive Antenna Arrays: Trends and Applications, Springer-Verlag (in press).

3.   Patents (ANNOTATE EACH WITH FILED OR GRANTED):

None

4. Presentations (INVITED):

As a Distinguished Lecturer of the IEEE, I gave three invited presentations on the work performed under ONR grant in Istanbul, Ankara, and Cairo. Over the period of January 5th-15th, 03.

5. Presentations (CONTRIBUTED):

Y. Zhang, M. G. Amin, and H. Ge, "Nonstationary interference suppression in DS/SS communications using space-time oblique projection techniques," IEEE International Symposium on Signal Processing and Information Technology, Marrakech, Morocco, December 2002.

Y. Zhang, M. G. Amin, and A. R. Lindsey, "Improved blind separations of nonstationary sources based on spatial time-frequency distributions," Fourth International Symposium on Independent Component Analysis and Blind Signal Processing, Nara, Japan, April 2003.

Y. Zhang, M. G. Amin, and G. J. Frazer, "High resolution time-frequency distributions for manuvering target detection in over-the-horizon radars," IEEE International Conference on Acoustics, Speech, and Signal Processing, Hong Kong, China, April 2003.

L. A. Cirillo and M. G. Amin, "Auto-term detection using time-frequency array processing," IEEE International Conference on Acoustics, Speech, and Signal Processing, Hong Kong, China, April 2003.

G. Wang, X.-G. Xia, B. Root, V. Chen, Y. Zhang, and M. G. Amin, "Manuvering target detection in over-the-horizon radar by using adaptive chirplet transform and subspace clutter rejection," IEEE International Conference on Acoustics, Speech, and Signal Processing, Hong Kong, China, April 2003.

Y. Zhang, M. G. Amin, and B. A. Obeidat, "Direction finding using spatial polarimetric time-frequency distributions," International Symposium on Signal Processing and Its Applications, Paris, France, July 2003.

Y. Zhang, M. G. Amin, B. M. Dogahe, and G. J. Frazer, "Time-frequency analysis for maneuvering target detection in over-the-horizon radars," International Symposium on Signal Processing and Its Applications, Paris, France, July 2003.

Y. Zhang, K. Yang, and M. G. Amin, "Space-time adaptive processing and subband array implementations," SPIE Annual Meeting, San Diego, CA, Aug. 2003.

Y. Zhang, M. G. Amin, and B. Obeidat, "Spatial polarimetric time-frequency distributions and applications to direction-of-arrival estimation," SPIE Annual Meeting, San Diego, CA, Aug. 2003.

Y. Zhang, B. A. Obeidat, and M. G. Amin, "Polarimetric time-frequency MUSIC in coherent signal environment," IEEE Workshop on Statistical Signal Processing, St. Louis, MO, Sept., 2003.

6.   Honors (Presidential YIP, elections to Fellow status in major scientific society; appointed editor of scientific journal, elected NAS/NAE/IOM, awarded medal by scientific society, Chairman of scientific meeting, etc):

2003-Distinguished Lecturere for the IEEE Signal Processing Society.

Two Session Chair: IEEE International Symposium on Signal Processing and its Applications, Paris France, July 2003.

Served on the Advisory Committee of the IEEE International Conference on Acoustics, Speech, and Signal Processing, Hong Kong, April 2003.

Served on the Franklin Institute Committee on Science and Arts.

Organizer of the Franklin Institute Workshop on Speech Coding and Recognition, honoring the Medal Recipient, Dr. B. Atal, April 2003.

7.   Number of graduate students:

One-graduate student (full-time)

8.   Number of Post-doctoral students:

One full-time Postdoctoral Fellow and one half-time Postdoctoral Fellow

9.   Number of undergraduate students supported:

None

10.   Number of under-represented members by group:

One women (Postdoc.)

REPORT DOCUMENTATION PAGE

1. REPORT DATE (DD-MM-YYYY)	2. REPORT DATE	3. DATES COVERED (From - To)
1-10-2003	Interim	October 2002-September 2003

4. TITLE AND SUBTITLE	5a. CONTRACT NUMBER
Classification and Discrimination of Sources with Time-Varying Frequency and Spatial Spectra	**5b. GRANT NUMBER** G-N00014-98-1-0176
	5c. PROGRAM ELEMENT NUMBER

6. AUTHOR(S)	5d. PROJECT NUMBER
Moeness G. Amin	**5e. TASK NUMBER**
	5f. WORK UNIT NUMBER

7. PERFORMING ORGANIZATION NAME(S) AND ADDRESS(ES)	8. PERFORMING ORGANIZATION REPORT NUMBER
Villanova University 800 Lancaster Ave Villanova, PA 19085	Acc: 527616

9. SPONSORING/MONITORING AGENCY NAME(S) AND ADDRESS(ES)	10. SPONSOR/MONITOR'S ACRONYM(S)
G. D. McNeal Office of Naval Research Ballston Center Tower One 800 North Quincy Street Arlinton. VA 22217-5660	**11. SPONSORING/MONITORING AGENCY REPORT NUMBER**

12. DISTRIBUTION AVAILABILITY STATEMENT

Approved for Public Release; Distribution is Unlimited

13. SUPPLEMENTARY NOTES

14. ABSTRACT

The research objectives in FY03 evolved around the detection of complex Doppler target signatures using time-frequency signal representations. In additions to achieving these objectives, the research has progressed on two other fronts; namely, Polarimetric Sensor Array Processing and Subband Array Implementations for Space-Time Processing. We have developed a high-resolution time-varying signature estimation of weak target signals for Over-the-Horizon Radars (OTHRs). We have also developed polarimetric time-frequency distributions for sensor arrays. We continued to analyze the performance of several subband array processing schemes. In particular, we have evaluated the effect of decimation on the mean square errors and examined the advantages of performing subband processing on the received input data as well as the desired (reference) signal.

15. SUBJECT TERMS

Time-Frequency Distribution, Over-the-Horizon Radar, Polarization, Direction Finding, Space-Time Processing, Subband Arrays, Spread Spectrum Communications

16. SECURITY CLASSIFICATION OF:			17. LIMITATION OF ABSTRACT	18. NUMBER OF PAGES	19a. NAME OF RESPONSIBLE PERSON
a. REPORT	b. ABSTRACT	c. THIS PAGE			
U	U	U	UU	160	**19b. TELEPONE NUMBER (Include area code)**